Cosmic-Ray Muons in the L3 Detector

(A pilot study in determining the secondary muon flux)

Een wetenschappelijke proeve op het gebied
van de Natuurwetenschappen, Wiskunde en Informatica

Proefschrift

ter verkrijging van de graad van doctor
aan de Katholieke Universiteit Nijmegen,
volgens besluit van het College van Decanen
in het openbaar te verdedigen
op maandag 8 januari 2001,
des namiddags om 3.30 uur precies, door

Albertus Johannes Wilhelmus van Mil

geboren op 1 september 1966 te Rips.

Promotores: **Prof. Dr. E.W. Kittel**
Prof. Dr. J.M.E. Kuijpers

Co-promotor: **Dr. C.J.W.P. Timmermans**

Manuscriptcommissie: **Prof. Dr. M. Pohl**
Prof. Dr. A. Achterberg   (Utrecht University)
Dr. G.J. Bobbink   (NIKHEF Amsterdam)
Dr. P. LeCoultre   (ETH Zürich)

Acknowledgements

During the time I was working as a PhD student at the Department of High Energy Physics in Nijmegen I enjoyed the help and company of many people. I would like to express my gratitude to some of them, since I cannot possibly mention everyone.

First I thank Prof. Wolfram Kittel and Prof. Jan Kuijpers for letting me work the first year at the department as an army TEGGER. It's a loss of culture now this is not possible anymore.

I spend two years at CERN in Geneva. The group of "Cosmic guys" was barely enough at that time to call it a group. I thank Pierre LeCoultre for the support and help he gave me. It was a tough time, but seeing the slow progress of "L3+Cosmics" helped sustaining the effort. I also thank Ulrich Uwer for explaining me everything I wanted to know about the scintillators and Ingrid Clare for all the work she did in helping me to handle the tapes and process them. See here, Mr. Cosmic is finally finished ! I also thank Prof. Remy van de Walle for the illuminating monologs, dialogs and discussions.

It was a pleasure to find company in the other Dutch people from surrounding offices and other students at CERN, of whom I want to mention Frank Filthaut, Gerhard Raven, Tasja van Rhee, Sandra Muijs, Daniel van Dierendonck and Andreas Korn. I much liked the (almost) weekly trips to the cinema accompanied by a good Swiss style meal.

One of the best experiences I had were the (too) few visits to Macumba. Thank you Herve, for introducing me to the wild side of life in Switzerland (or was it France ?)

In Nijmegen it was a pleasure to work, even in the "koelcel". I was very happy to experience the company of Bert Petersen and Henric Wilkens, so that finally I could argue with someone about cosmic and less cosmic matters. The touch of the lightness of being was added by Charles Timmermans on a daily basis and helped to keep seeing things in perspective. I obtained a lot of help from you three: thanks for that !

The people of our department made the "happy hour" on Friday afternoon always a good start of the weekend, with and also without cake. Of the students at our department I would like to mention Mirna "double star" van Hoek, Michiel "Janssen" Sanders, Wim++ Lavrijsen, Ljubisa Drndarski, Erik Visser, Jorn van Dalen, Roy Smits and Martin van den Akker, without whom the days at the department would have been much more tough.

For the regular (non-)computing issues it was always possible to find an ear in our system managers Peter Klok and Frans Rohde. For the more delicate issues, Erna Dickmans, Marjo van Wees, Martine Schout, Hanneke Vos and Annelies Oosterhof gave a helping hand.

Finally, but not least, thanks to my friends and family for the necessary diversion during the past six years and their continuous support and interest into the subject.

Contents

Chapter 1

Introduction

In this chapter a general introduction to cosmic rays is given. The discovery of cosmic rays and their physics interest is briefly described. The potential importance of the L3 detector at CERN as a cosmic-ray muon spectrograph is explained.

1.1 Introduction

This work addresses measurements of the cosmic-ray muon energy spectrum and its physics implications, performed with the L3 detector at CERN, Geneva, Switzerland. In high energy physics, cosmic rays have in general been replaced by man-made beams of particles, accelerated to accurately determined energies and colliding at pre-determined points inside a detector. The big advantage of this approach is, of course, that physics analysis becomes a lot simpler because the input parameters can be set by "turning the right knob". Cosmic rays, particles originating from the cosmos, don't have such a knob. This makes life for cosmic-ray physicists much harder than for accelerator physicists, but it does not mean that their life is less interesting. On the contrary, cosmic rays contain a wealth of information on the flavour and energy (up to 10^{21} eV) of particles, stunning particle-physicists and astro-physicists alike.

   Cosmic rays play an important role in the dynamics of our galaxy [1; 2]. The energy densities of cosmic rays, the galactic magnetic field and the thermal gas in the interstellar medium are comparable in magnitude, about 1 eV/cm^3. The total energy put into cosmic rays in our galaxy is estimated to be about 10^{60} eV per year. In composition, cosmic rays show an abundance which is different from that of main-sequence stars. Although the cosmic ray composition is largely related to nucleosynthesis in stars and to the evolution of stellar composition and the interstellar medium, cosmic rays also undergo spallation in the interstellar gas. As a result, a pool of rare nuclei is being built up continuously. If one knows the spallation cross sections and the measured abundances, the initial composition

at the source can be calculated. As has been shown by several authors, this composition strikingly corresponds to the general abundances of the elements in our galaxy [3].

Most cosmic rays with energy up to 10^{18} eV come from within our galaxy [1], and a very low fraction of them (below a few GeV for protons) originates in the lower solar atmosphere (flares), with temporal behaviour dictated by the eleven-year solar-activity cycle and random outbursts. At very high energies, the origin is probably extra-galactic. The majority of the cosmic rays have a homogeneous distribution in space and time.

Numerous calculations have shown that the acceleration to the highest energies cannot be accounted for by one single mechanism. The large range of energies observed implies a series of different cascading mechanisms, much like the necessary pre-acceleration stages in man-made particle accelerators. Actually, the presence of a "knee" and an "ankle" in the momentum spectrum (Fig. 2.1), probably imply different acceleration mechanisms for the energies beyond these regions. It is generally understood that the shock waves of supernova remnants (SNR) are the main sites of particle acceleration. Diffusive shock acceleration produces a spectrum that is close to the one observed and it can refurbish the spectrum during a long time period [4; 5; 6].

For the highest energy cosmic rays, no convincing mechanism nor power source has, up to now, been demonstrated. Some observations seem to point at supernova explosions where the energy of the explosion is dumped into a relatively small area of space around the imploded star. Other possibilities include the merging of a binary neutron-star system or a combination of stochastic and electromagnetic acceleration near neutron stars or active galactic nuclei (AGN) (see [7] for a short overview). Much research is currently undertaken to investigate these curious events. It is even not clear at all whether the primary particles have rest mass or if they are photons. What the primary composition in the high energy regime is, photons, protons or other nuclei, is one of the main questions hopefully to be answered in the next decennium.

There is one other aspect of cosmic-ray research we want to mention here. Already since the discovery of elementary particles themselves, cosmic rays have served as a source of new physics. Although the standard model as it is known today did surprisingly well in explaining sub-atomic physics, some cosmic-ray experiments have found indications for new physics outside the standard model (see [8] and references therein). The reason for the scepticism on these events is that they are hard to reproduce because of their sparse nature. Also the experimental setups are normally not capable of a precise measurement of the event. Therefore, at face value, these events hardly contain any solid evidence. On the other hand, some theories (and extensions to the standard model) like super-symmetry predict the existence of new particles. Since accelerator experiments in the recent past did not provide anything unexpected, the energy required to produce exotic particles might well be beyond our reach but *within* reach of the cosmos. That's why cosmic rays still offer us a "Box of Pandora" which might reveal interesting physics to us, one day, just like it did in the past.

1.2 History of the study of cosmic rays

The history of the study of cosmic rays starts with the experimental evidence for the existence of charged particles, as well as X- and gamma-rays. Early experiments by W. Crookes in 1895 [9] showed that in a so-called "Crookes tube" cathode rays were generated. These rays could be deflected by a magnetic field, as was found later. In 1897, J.J. Thomson performed a charge/mass measurement on these cathode rays, showing that this ratio was far larger than the one for hydrogen. After measuring the charge of the

cathode rays he found the mass of this first *elementary particle* to be about 1/1000 that of a hydrogen atom. The particles produced by the photoelectric effect were identified to be the same as the cathode rays, both being named *electrons*. In 1896, Becquerel discovered the *natural radioactivity* through the blackening of photographic plates far from any light source. In the next few years, Rutherford discovered α and β rays as two separate radiative components of a radioactive substance. In 1895 W.C. Röntgen discovered the X rays. The γ rays were discovered in 1900 by Villard. Up to then, natural radio activity was the only known source of energetic particles and gamma rays.

The onset to the experimental evidence of cosmic rays came from the fact that electroscopes, when kept in the dark and away from any radioactive source still showed a slow discharge. Experiments on this discharge of electroscopes were performed by C.T.R. Wilson, Geitel and Elster [10; 11; 12; 13; 14], who found that the discharge was due to radiation from outside the electroscope.

In 1910, Wulf ascended the Eiffel Tower carrying an electroscope with him, which showed a decrease of ionisation with increasing altitude, at least up to 330 meters. The rate of decrease with increasing altitude was, however, not enough to be explained by gamma rays originating from the surface of the earth. In 1911-12, V. Hess and his assistants made balloon flights up to 5 km of altitude, carrying with them an ionisation chamber [15]. Balloon ascents were also made by Kolhörster, up to 9 km [16; 17]. They found that above about 1.5 km altitude, the ionisation rate increased with respect to the rate at sea level. The source of the ionisation, therefore, had to be extraterrestrial, but still producing noticeable effects at ground level. In 1925, this radiation was named *cosmic radiation* by R. Millikan. Up to then, this cosmic radiation was believed to consist of γ-radiation. Experimental facts put forward by Clay, Compton and Johnson [18; 19; 20; 21] around 1930-33, showed that part of the cosmic radiation could be deflected by the earth magnetic field, and thus had to consist of charged particles.

The discovery, among others, of the positron in cosmic radiation by C. Anderson in 1933 [22] led to the concept of electromagnetic cascades. This theory of cascades led to the discovery in 1938 of the *extensive air showers* by Schmeiser and Bothe, Auger et al. and Kolhörster et al.[23; 24; 25].

From that time on, numerous experiments were performed using Geiger-Müller counters and cloud chambers. The cosmic radiation provided the source of highly energetic particles with which experiments were performed up to the 50's. A lot of new particles were discovered by photographing the cloud chamber events. By 1953, the first accelerator experiments were performed using a stable beam of accelerated particles. From that time on, cosmic rays were studied less extensively. The development of astro-particle physics, however, during the 80's and 90's has lead to a renewed interest in cosmic-ray experiments. Part of the cosmic rays, of energies up to nearly 10^{21} eV [26], far surpass accelerator experiments in energy.

1.3 The L3 detector as a cosmic-ray muon spectrograph

The L3 detector at LEP (CERN, Geneva) [27], as described in this thesis, is used as a cosmic-muon spectrograph. Here, a first evaluation of its capabilities is given, using cosmic-muon data taken for calibration purposes in 1991. The strength of the L3 detector lies in the detection of leptons (electrons and muons) as well as photons. The muon detector takes up the largest volume of the apparatus (Fig. 1.1). It is enclosed by a magnet coil and yoke, see Ch. 4. The advantages of the L3 detector in its use as a spectrometer are:

Z-Measuring
Strip Chamber

Plastic Scintillating
Fibres (PSF)

Time Expansion
Chamber (TEC)

Electromagnetic
Calorimeter (BGO)

Scintillator
Counters

Hadron Calorimeter
(Uranium-MWPC)

Muon Filter
(Brass-MWPC)

Muon Chambers
(MO, MM, MI)

-6   -3   0   3   6 metres
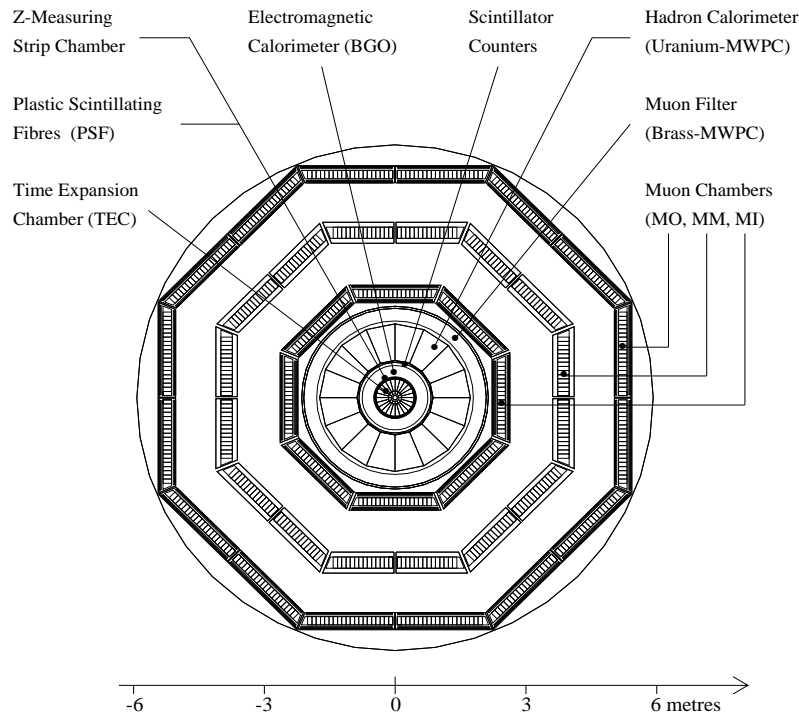
Fig. 1.1. Front view of the L3 detector showing the muon chambers and subdetectors.

– The cosmic-ray flux is shielded by about 30 meters of molasse. This is enough to absorb the low energy debris, electrons and hadrons, and at the same time leaving through cosmic-ray muons from about 20 GeV/c on. Any leakage cosmic-ray flux other than muons is stopped with high probability by the magnet yoke and coil, each of about 1 meter in thickness.
– The molasse on top of the L3 detector has been examined thoroughly by a geological survey. The chance on any undetected holes in the molasse is minimal and the molasse composition has been determined accurately. The molasse is also easy to simulate since the top layer is flat within a radius of about 100 meters from the L3 detector position.
– The accuracy $\Delta p/p$ with which the cosmic-ray muon momentum can be measured is designed to be about 3.5% $\times p/(45 \text{ GeV}/c)$, which is considerably better than other cosmic-ray experiments employing magnetic spectrometers. The charge of the muon can thus be measured up to about 3 TeV/c of muon momentum, before the charge confusion reaches its maximum value.

These advantages make it worthwhile to exploit the L3 detector in a pioneering experiment as a cosmic-ray muon spectrometer.

Chapter 2

Theory

This chapter gives a summary of the basic theory of cosmic-ray air showers and the secondary muon flux. The primary composition and the role of the atmosphere in the development of an air shower are briefly discussed. As an introduction to the theory of transport equations some generally used terminology is reviewed. The transport equations are set up and a simple derivation of the muon energy spectrum and the muon charge ratio is performed.

2.1 Primary composition and spectrum

The cosmic-ray energy spectrum extends over more than 11 decades (Fig. 2.1). Up to nearly 10^{15} eV, the spectrum can be well described by a single power-law relation. Between 10^{15} eV and $10^{18.5}$ eV, the spectrum is steeper, but another change in slope is observed beyond $10^{18.5}$ eV. The sudden changes in the spectral index near 10^{15} and $10^{18.5}$ eV, commonly known as the "knee" and the "ankle", are believed to reflect a change in the propagation of the particles in the interstellar medium and/or in the sources and acceleration mechanisms. At least below 10^{18} eV, cosmic rays originate from within our galaxy out of which they diffuse with a typical time scale of 10^7 years. Cosmic rays above $10^{18.5}$ eV are thought to be of extra-galactic origin, since the composition seems to change from predominantly heavy to light nuclei above this energy and the galaxy is transparent for particles of these energies.

The distance over which these *Ultra High Energy* (UHE) particles can survive is limited by photo-pion production on the Cosmic Microwave Background Radiation (CMBR). In case of protons the reactions are e.g. $p + \gamma \rightarrow \Delta \rightarrow p + \pi^0 ; p + 2\pi^0 ; n + \pi^+$, with similar reactions for neutrons and nuclei. For a proton, the typical CMBR temperature of 2.7 K leads to a mean interaction length of the order of 5 Mpc [1]. After a few such interactions the proton has lost nearly all of its energy. The very existence of photo-pion production leads to a maximum observable energy for a proton of order 10^{20} eV, close to the observed "ankle" in the spectrum. It also leads to the notion that a cut-off of particles should occur, in theory, near $10^{19.5}$ eV. This cut-off is known as the *Greisen-Zatsepin-Kuzmin cut-off*
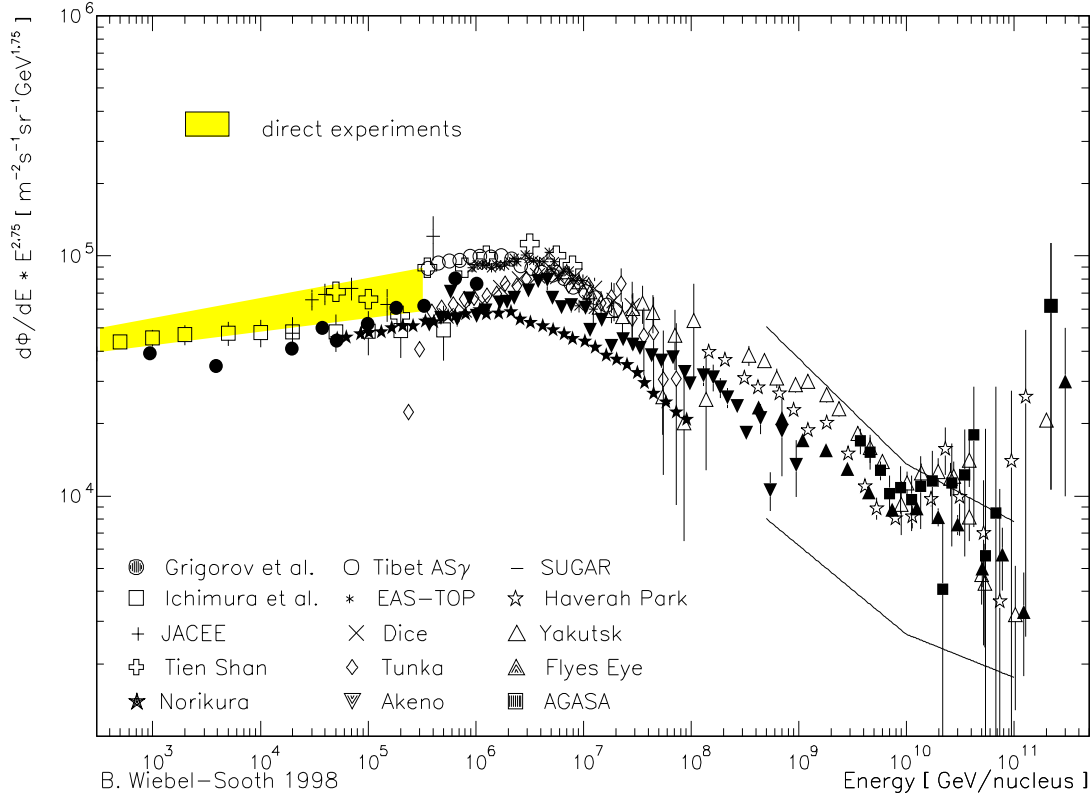
Fig. 2.1. The cosmic-ray all-particle spectrum for charged primaries. The knee and ankle are visible near 10^6 and $10^{9.5}$ GeV/nucleus [28].

[29; 30]. The existence of a particle flux with energy above ca. $10^{19.5}$ eV, defying theory, triggered the construction of experiments like the Auger project [31], which are designed specifically to study these events.

One of the main difficulties in the study of cosmic rays today is the unknown composition of the primary flux above the "knee" and near the "ankle". In this energy range, the flux diminishes so rapidly (at about 1/50 per energy decade) that statistics are barely sufficient to obtain information on the shape of the spectrum itself. Above 1 TeV/nucleon the primary flux is known with an accuracy of at most 15%, and the situation becomes worse the higher the energy. At energies below about 10 GeV/nucleon the flux is modulated by the solar activity, in an 11 year cycle (Fig. 2.2). This affects the cosmic-ray flux by a factor of two for energies near 1 GeV/nucleon and by $\sim$ 10% near 10 GeV/nucleon. The composition

Nucleus	A	γ
H	$6.65 \pm 0.13 \cdot 10^{-2}$	-2.75 ± 0.02
He	$3.28 \pm 0.05 \cdot 10^{-3}$	-2.64 ± 0.01
CNO	$1.40 \pm 0.07 \cdot 10^{-4}$	-2.50 ± 0.06

Tab. 2.1. Fit parameters to cosmic-ray spectra, see text [32].
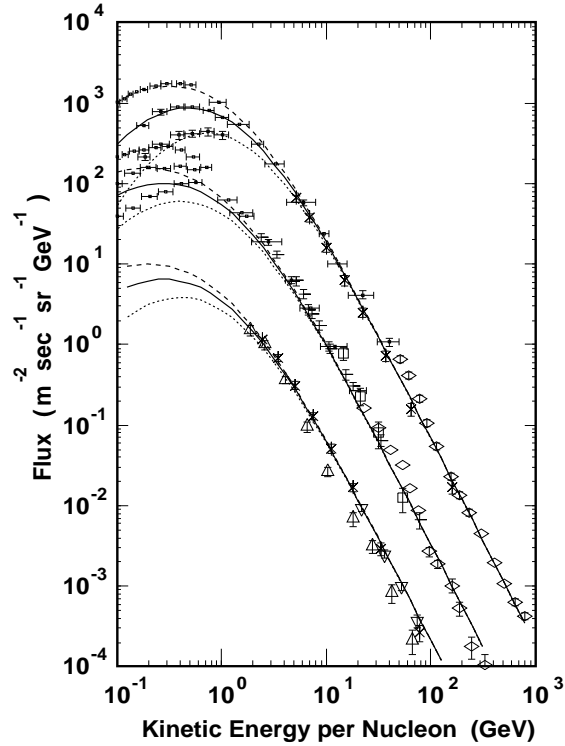
Fig. 2.2. Flux observed for protons (top curve), helium nuclei (middle curve) and CNO (lower curve) as a function of kinetic energy per nucleon and solar modulation strength. Solid lines are model fits for medium solar activity, dashed lines for minimum solar activity and dotted lines for maximum solar activity [32].

in the most important element groups up to energies near the "knee" has been determined as [32] H ($\sim 90.6\%, 95.2\%$), He($\sim 9.0\%, 4.5\%$) and CNO nuclei ($\sim 0.4\%, 0.3\%$), where the first numbers are for energies around ~ 100 MeV/nucleus, the second numbers for energies above ~ 2 GeV/nucleus. For the three groups H, He and CNO, Tab. 2.1 gives the results for an extrapolated function $F(E) = A \cdot (E/(100\,\mathrm{GeV/nucleon}))^\gamma$ describing the corresponding energy spectra up to the "knee".

2.2 Air showers

An air shower is created in our atmosphere every time a high-energy cosmic-ray particle enters the upper layers of the atmosphere and interacts with an air nucleus. The interaction creates a spray of new particles more or less in the same direction as the original primary (extremely relativistic) particle. Each constituent of this secondary flux can in turn interact by itself with air nuclei or decay, according to its mean lifetime. In both cases, new and more particles are created. As the shower develops, the mean energy available to each particle in the shower front will decrease. If the energy of the particle falls below the threshold for particle production, its energy will gradually be lost by ionisation and other, radiative, processes. An air shower will thus obtain a maximum number of particles as it develops as a function of atmospheric depth, after which it will deplete again by the loss of low-energy particles. The lateral extent of a shower increases as a function of depth.

This is mainly due to multiple Coulomb scattering of the electromagnetic component of the shower and, to a smaller extent, to the increasing opening angles of the (relativistic) particle interactions, as seen in the earth reference frame. An exception are any muons produced which have a long life time and, due to their large mass ($m_\mu/m_e = 207$), possess a lateral extent beyond the electromagnetic component.

Air showers can basically be divided into two types, according to whether the primary particle exhibits a hadronic or photonic nature. In case of a hadronic primary, strong interactions are involved in the collisions with atmospheric nuclei. These lead to a hadronic shower component, which constitutes the core of the air shower. This hadronic component generates mesons which, by decay, can create leptons which constitute the electromagnetic and muonic component of the shower (Fig. 2.3).
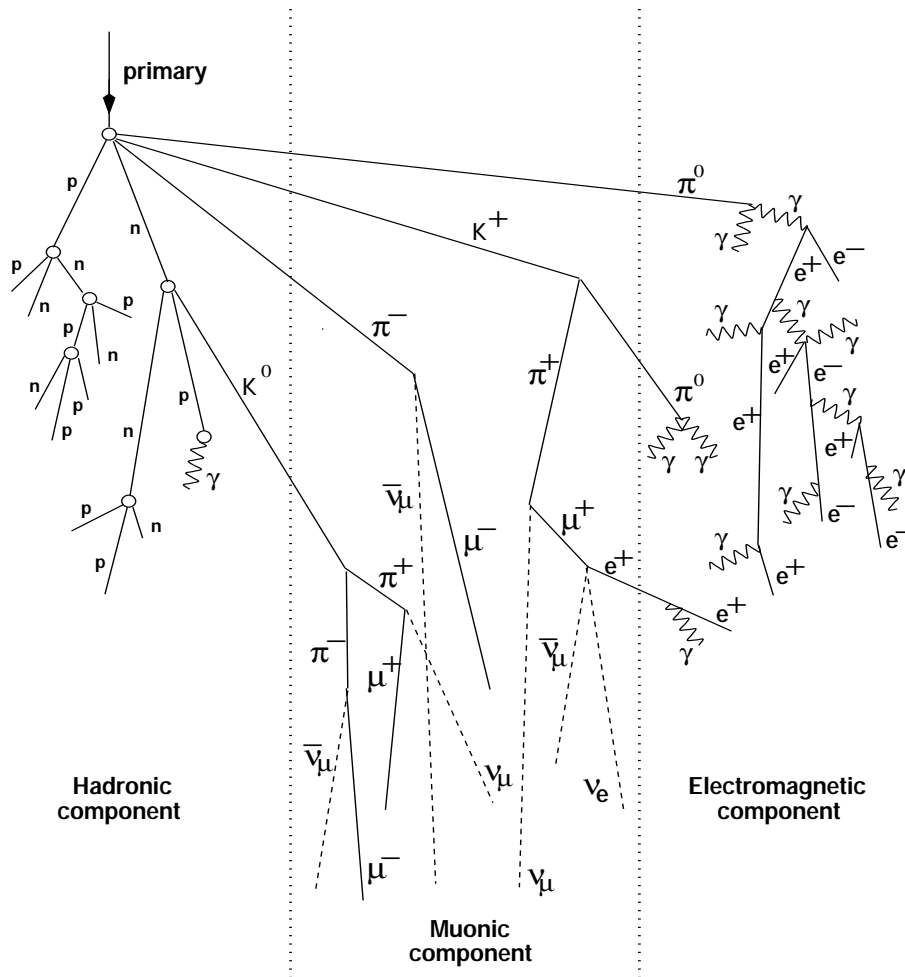
Fig. 2.3. Schematic development of a hadronic air shower, showing the hadronic, muonic and electromagnetic components. Only a few types of particles and interactions are visualized (adapted from [1]).

In case the primary is a photon, the shower largely consists of an electromagnetic component, developing by pair production and bremsstrahlung processes. The creation, via photoproduction, of hadrons, mesons or heavy leptons, as muons, is much less favourable

in such a shower than the creation of light leptons. This is due to the relatively low cross section of the former processes. Muon production usually proceeds by photoproduction (γ + nucleus $\rightarrow$ hadrons), with consecutive hadron decay. The relative occurrence of this process compared to e^+e^- pair production is (near 20 GeV photon energy) [33]

$$\sigma_{\gamma\rightarrow\text{hadrons}}/\sigma_{\gamma\rightarrow e^+e^-} \sim 2.8 \times 10^{-3}. \tag{2.1}$$

Pair production of muons is suppressed by a factor $(m_e/m_\mu)^2 \sim 2 \cdot 10^{-5}$ relative to pair production of electrons and positrons. The muon content of a photon shower will thus be much less (by a factor of ~ 30 [33]) than that of a hadronic shower. This difference is one of the main characteristics by which hadron and photon initiated showers can be distinguished experimentally. Each of the three components of the air shower of Fig. 2.3 develop in their own specific way:

– The *hadronic component:* This component determines largely how an air shower will develop. Protons, neutrons, other baryons and mesons are produced by interactions of the primary particle with air nuclei. These secondary particles can re-interact with air nuclei or can decay, depending on the value of the interaction length versus that of the decay length. For numerical values of interaction length and decay constant, for a number of particle types, see Tab. 2.2. In the case of interaction, new sub-showers are created if the available energy is large enough. Otherwise, the interactions can lead only to disintegration of the air nucleus or to creation of low-energy gamma rays by excitation of air nuclei. Secondaries which decay, mainly create mesons and refurbish the electromagnetic and the muonic components of the air shower.

– The *electromagnetic component:* This component represents the most copious part of an air shower. Part of the mesons produced by the hadronic component will decay into leptons and, sporadically, into other mesons. The heavier leptons produced will decay to lighter variants or will interact. By pair production, Compton scattering and bremsstrahlung, the electrons, positrons and photons generate a quickly developing electromagnetic shower. Accordingly, the mean energy per particle decreases rather quickly (radiation length for electrons ~ 37 gcm^{-2}). If the primary energy is $\gtrsim 10^{14}$ eV, this component can be detected easily at the earth surface, but it is not penetrating far below the surface due to its low mean energy and high interaction cross section.

– The *muonic component:* This component is the most strongly penetrating part of an air shower. The muons are created mainly by decay of pions and kaons, generated by the hadronic component. Due to the fact that the muon looses its energy primarily by ionisation of the surrounding medium, interactions do not prohibit its propagation in the air. The relativistic time dilation increases its lifetime long enough to enable it to reach the earth surface.
Another source of muons is the decay of charmed particles or particles of heavier flavour. The production of charmed particles is very low compared to that of other types of particles. The additional muon flux from charm decay is, therefore, negligible for primary particle energies much less than 100 TeV [33]. Due to the short lifetime of charmed particles, they will generally decay before interacting. The muons produced by them are for this reason called *prompt muons*.
Muons can, furthermore, be produced by neutrinos interacting with a nucleus, $\nu_\mu(\bar{\nu}_\mu) +$ n(p) $\rightarrow \mu^-(\mu^+) +$ p(n) $+ X$. The neutrinos need to be of energies $\gtrsim 1$ GeV in order to produce muons detectable by underground experiments ($E_\mu \gtrsim 0.2$ GeV) with a reasonable probability. For a neutrino energy of 1 TeV, the probability that it produces such a muon, in crossing the earth diameter, is about $5 \cdot 10^{-7}$ [33]. These neutrinos originate from an atmospheric air shower on the other side of the earth or from an

astrophysical source at many lightyears distance. The RMS angle between the original neutrino direction and the muon produced by its interaction is approximately given by

$$\theta_{\mathrm{RMS}} \sim \frac{1.8}{\sqrt{E_\nu/1\ \mathrm{TeV}}} \qquad (\text{degrees}), \qquad (2.2)$$

for neutrino energies between 10 GeV and 3 TeV [33]. Because of this angle, directionality between the muon and its parent neutrino is conserved to a high degree. Upward going muons can thus be used to study the neutrino flux from cosmic-ray air-showers, to look for galactic or extra-galactic sources of high energy neutrinos and to look for atmospheric neutrino oscillations.

Besides these three components, there is light generated by charged particles in the blue/UV region of the spectrum. This light consists of:

– *Cherenkov light:* The propagation of a charged particle in the atmosphere with a speed larger than the speed of light in this medium, will lead to the generation of Cherenkov light being emitted in a forward cone with opening angle $\theta = \arccos(c/nv)$ where n is the refractive index of the air and v is the velocity of the particle.
– *Fluorescence light:* The excitation of an atom by a charged particle results in the emission of ultraviolet scintillation light. Most of the light is generated by nitrogen atoms.

Both types of radiation can be detected on earth by light-collecting telescopes.

2.3 The atmosphere

Besides by the type of the primary interaction, the development of a cosmic-ray air shower is determined by the properties of the atmosphere. In particular, the muon component of an air shower depends largely on the decay of unstable mesons as pions and kaons, with a lifetime dictated by their energy through relativistic time dilation. The balance between decay of a meson and interaction with the atmosphere thus depends on the atmospheric density and composition and on the energy of the meson itself. The inclination of a particle track determines the relative path length spent in the upper and lower parts of the atmosphere and thus also influences this balance. At an altitude of 25 km, the atmospheric
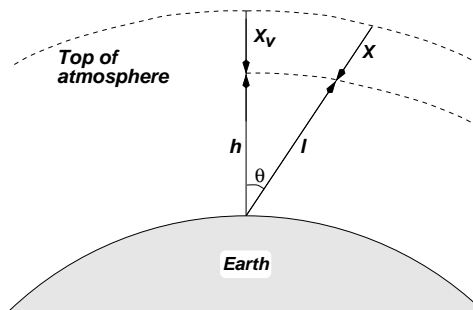

Fig. 2.4. Definition of variables to describe the atmosphere (the thickness of the atmosphere is grossly exaggerated).

density is only about 5% of the density at the surface. For most applications the atmosphere

can be approximated by a flat isothermal layer of gas extending to approximately 25 km in height. Only for zenith angles θ larger than $60°$, the curvature of the earth has to be taken into account. The slant depth $X(l, \theta)$ is defined as

$$X(l, \theta) = \int_l^\infty \rho(l', \theta) \mathrm{d}l', \tag{2.3}$$

where $\rho(l, \theta)$ is the density of the atmosphere at a distance l along the particle trajectory as seen from the earth's surface (Fig. 2.4). The vertical altitude h can be approximated by

$$h \cong l \, \cos\theta + \frac{l^2}{2R_\oplus} \sin^2\theta \tag{2.4}$$

where $R_\oplus$ is the earth radius and where we have assumed that $l/R_\oplus \ll 1$. The second term in Eq. (2.4) is important for $\theta > 60°$ only and will be neglected in the forthcoming discussion.

The ratio of atmospheric pressure p over density ρ is proportional to the temperature T. For an isothermal atmosphere, the vertical depth X_v as measured from the top of the atmosphere is given according to

$$\frac{p}{\rho} = \frac{X_v}{-\mathrm{d}X_v/\mathrm{d}h} = \frac{RT}{Mg} \quad \Longrightarrow \quad X_v = X_0 \, \mathrm{e}^{-h/h_0}, \tag{2.5}$$

where $h_0 \equiv \frac{RT}{Mg}$ is the *scale height* given in terms of the gas constant R, temperature T, molecular weight M and gravitational acceleration g. The total vertical atmospheric depth $X_0 \cong 1030 \text{ gcm}^{-2}$ defines the "top of the atmosphere". The real atmosphere is of course far from isothermal. The temperature drops with increasing altitude up to the tropopause and hence the scale height h_0 decreases accordingly. At sea level $h_0 \cong 8.4$ km, while at $X_v < 200 \text{ gcm}^{-2}$, $h_0 \cong 6.4$ km. In our case the temperature variation with height is however not taken into account. The density as a function of X_v is given by

$$\rho = -\mathrm{d}X_v/\mathrm{d}h = X_v/h_0. \tag{2.6}$$

2.4 An intermezzo of terminology

As an introduction to the transport equations to be treated in the next section, we will review some terminology commonly used in cosmic-ray theory. Sections 2.4-2.5 are largely based on [33].

2.4.1 Decay and interaction lengths

The global development of a cosmic-ray air shower is governed by the competition between decay and interaction of secondary particles. The strength of these two processes can be expressed in terms of the mean decay length d_i and the mean interaction length λ_i, where the subscript i labels a certain secondary particle. The *mean decay length* d_i of a particle with proper lifetime τ_i and rest mass m_i is defined as the slant depth X_i the particle traverses before decaying, $d_i = \rho \gamma_i c \tau_i$, where ρ is the local atmospheric density at altitude h. Expressed as a function of the particle energy E_i,

$$d_i = \frac{\rho c \tau_i E_i}{m_i c^2}. \tag{2.7}$$

From Eq. (2.4) we find $h \cong l \cos \theta$, so that $X_v \cong X \cos \theta$ and $\rho \cong X \cos \theta / h_0$. The decay length can then be expressed as

$$d_i = X \cos \theta \frac{E_i}{\epsilon_i}, \tag{2.8}$$

where $\epsilon_i = m_i c^2 h_0 / (c \tau_i)$.

The *mean interaction length* of a particle in air depends on the total inelastic cross section with the air nuclei

$$\lambda_i = \frac{\rho}{\rho_N \sigma_i}, \tag{2.9}$$

where ρ_N is the number-density of nuclei in the atmosphere and σ_i is the inelastic cross section on air for particle type i. Assuming a mean number of nucleons A ($\cong 14.5$) in an air nucleus, the mean interaction length is expressed as

$$\lambda_i = \frac{A \, m_p}{\sigma_i} \tag{2.10}$$

where m_p is the proton mass. In Tab. 2.2 a rough indication for the numerical value of decay and interaction lengths is given, evaluated at $h_0 = 6.4$ km and using extrapolated interaction cross sections (for reference $X_0 \cong 1030$ gcm^{-2}).

Particle type	ϵ_i (GeV)
$K^\pm$	850
K_S	$1.2 \cdot 10^5$
K_L	205
$\pi^\pm$	115
π^0	$3.5 \cdot 10^{10}$
$\mu^\pm$	1.0

Lab energy (TeV)	Interaction length λ_i (g cm^{-2})		
	p-air	π-air	K-air
0.1	86	116	138
1.0	83	107	-
1000	60	70	-
10^6	43	50	-

Tab. 2.2. Mean decay constant ϵ_i and interaction length λ_i for a few particle types [33].

2.4.2 Boundary conditions

The transport equations to be solved are subject to physical boundary conditions. The boundary condition most important is the specification of the differential primary flux at slant depth $X = 0$ and primary energy E. Between certain limits of energy, the spectral shape for a given type of primary can be approximated by a power law. The overall primary spectrum between 10^9 eV and 10^{15} eV is estimated as

$$\left. \frac{dN(E, X)}{dE} \right|_{X=0} \equiv N_0(E) \cong 1.8 \cdot E^{-2.7} \frac{\text{nucleons}}{\text{cm}^2 \text{ sr s (GeV}/A)}, \tag{2.11}$$

where A is the mass number of the incident nucleus.

2.4.3 Superposition approximation

Within the *superposition approximation* one assumes that an incident nucleus of mass number A and energy E_0 can be treated as A independent nucleons, each with an energy E_0/A. This can be justified since the binding energy between the nucleons is usually much less than the energies of interest in cosmic-ray physics. The degree of validity of this approximation depends on the problem under consideration.

2.4.4 Cross sections

The production of particles in collisions can be described by the Lorentz-invariant *n-particle inclusive cross section* σ_n, which is defined for uncorrelated production in the process (a + b $\rightarrow \sum_{i=1}^{n}$ c$_i$ + anything) as

$$\sigma_n = \prod_{i=1}^{n} \frac{E_i \, \mathrm{d}^3 \sigma_{\mathrm{ab}}^{\mathrm{c}_i}}{\mathrm{d}^3 p_i}, \tag{2.12}$$

where $\boldsymbol{p}_i$ and E_i are the momentum and energy of particle c$_i$ and $\sigma_{\mathrm{ab}}^{\mathrm{c}_i}$ is the interaction cross section for particle a on b to produce particle c$_i$. The total cross section is indicated by σ_0. If correlations between secondaries have to be taken into account, e.g. in strangeness conservation, higher-order cross-terms are necessary. Assuming independent production, the terms σ_0 and σ_1 usually suffice. For the single-particle inclusive cross section for the process (a + b $\rightarrow$ c + anything) we thus find

$$\sigma_1 = \frac{E_{\mathrm{c}} \, \mathrm{d}^3 \sigma_{\mathrm{ab}}^{\mathrm{c}}}{\mathrm{d}^3 p_{\mathrm{c}}} = \frac{\mathrm{d}^2 \sigma_{\mathrm{ab}}^{\mathrm{c}}}{\pi \mathrm{d}(p_{\mathrm{c}\perp}) \mathrm{d}(p_{\mathrm{c}\parallel}/E_{\mathrm{c}})} \equiv f_{\mathrm{ac}}^{(\mathrm{b})}(\sqrt{s}, p_\parallel, p_\perp), \tag{2.13}$$

where $\sqrt{s}$ is the center of mass (CMS) energy and where we have used that, for fixed E_{c}, $\mathrm{d}(p_\perp/E_c) = \mathrm{d}p_\perp/E_c$ holds. At energies much larger than the particle masses, one has $s \propto E_{\mathrm{lab}}$, where E_{lab} is the energy as measured in the reference (lab) system.

In the theory of transport equations one uses, instead of the inclusive cross section σ_n, the *dimensionless inclusive cross section* F_{ij} defined by

$$F_{ij}(E_j, E_i) = E_j \frac{\mathrm{d}n_{ij}(E_j, E_i)}{\mathrm{d}E_j} \tag{2.14}$$

where $\mathrm{d}n_{ij}$ is the average number of particles of type j having energy within $\mathrm{d}E_j$ around E_j, produced by an incident particle of type i. The precise details of the interaction are absorbed in the definition of F_{ij}.

2.4.5 Scaling behaviour

One of the most important ideas extending the testable theory of particle interactions to energies beyond direct experimental evidence is the *hypothesis of limiting fragmentation* (HLF) [34; 35]. In a nutshell, this hypothesis states that for any interaction the distribution of the longitudinal momenta of the secondary particles reflects the momentum distribution of the constituents of the incident particle. Thus, these longitudinal momenta $p_\parallel$ tend to *scale* with incident momentum. The transverse momentum distribution $\mathrm{d}\sigma_{ab}^c/\mathrm{d}(p_{c\perp}^2)$ of the secondaries is approximately Gaussian in $p_{c\perp}$. This is inherited from the uncertainty principle relating it to the size of the nucleus. Expressed in terms of the inclusive cross section and in the CMS system, indicated by the asterisk, HLF reads

$$f_{\text{ac}}^{(b)}(\sqrt{s}, p_{\parallel}^{*}, p_{\perp}) \xrightarrow{\sqrt{s} \to \infty} f_{\text{ac}}^{(b)}(x^{*}, p_{\perp}), \tag{2.15}$$

meaning that under $s \to \infty$, the dependence on the variable $x^{*} \cong 2p_{\parallel}^{*}/\sqrt{s}$ remains fixed. Here x^{*}, more precisely defined as $x^{*} = p_{\parallel}^{*}/p_{\parallel}^{*}(\text{max})$, is called *Feynman x* and is naturally limited to $-1 \leq x^{*} \leq 1$. In the laboratory system, x^{*} is replaced by $x_{\text{L}} = p_{\parallel\text{L}}/p_{\parallel\text{L}}(\text{max})$. We can now distinguish three regions according to x^{*}: the *beam fragmentation region* and the *target fragmentation region*, both characterized by $|x^{*}| \neq 0$ and the *central region* with $x^{*} \sim 0$. In the scaling limit, the beam fragmentation region does not depend on a specific target, nor does the target fragmentation region depend on the beam particle type. For the central region, HLF is found to be violated at high energies.

2.4.6 Approximation A

In the following sections, we will use approximations originating from electromagnetic cascade theory and collectively known as *Approximation A*. The most important approximations are:

– the ionisation energy losses of charged particles are neglected,
– the inclusive cross sections for bremsstrahlung and pair production scale with CMS energy,
– the mean interaction length λ is independent of energy.

These assumptions, although violated in reality, enable one to solve the transport equations analytically in a zeroth-order approximation while retaining their general qualitative aspects. The first assumption implies that there will be a lower bound on the energy of the secondary particles below which the results given by the theory under these assumptions will no longer be valid. For particle energies larger than $\sim 10\,\text{GeV}$ the gross properties of the spectra are however reproduced rather well. The transport equations are assumed here to propagate particles in one dimension instead of in three dimensions. Since we are not interested in spatial (i.e. lateral) properties of air showers and since the overall particle flux can be well described by the one-dimensional equations, this is a fair limitation.

2.5 Transport equations

A set of coupled integro-differential equations which describe the propagation of particles through the atmosphere as a function of slant depth X are called *transport equations*. The transport equations give rise to an expression for the muon flux and the muon charge ratio at sea level, which will be described in the next sections.

2.5.1 Transport of nucleons

The nucleonic flux is altered by interactions which decrease the initial flux and increase the secondary flux by newly created nucleons. Mathematically, the nucleon transport reads

$$\frac{\mathrm{d}N(E, X)}{\mathrm{d}X} = -\frac{N(E, X)}{\lambda_{\text{N}}} + \frac{1}{\lambda_{\text{N}}} \int_{E}^{\infty} N(E', X) F_{\text{NN}}(E, E') \frac{\mathrm{d}E'}{E}, \tag{2.16}$$

where the subscript N denotes a nucleonic particle. The first term on the right-hand side represents the depletion of nucleons by interactions with atmospheric particles, while the

second term represents the enhancement of nucleons by inter-nucleon interactions. This equation can be factorized into an energy dependent and a depth dependent term, using the ansatz: $N(E, X) = G(E)\,g(X)$. After substitution of $x_L = E/E'$ and elimination of $N(E, X)$ in lhs and rhs, we then find

$$-\frac{1}{\lambda_N} + \frac{1}{G(E)}\frac{1}{\lambda_N}\int_0^1 G(E/x_L)F_{NN}(E, x_L)\frac{\mathrm{d}x_L}{x_L^2} = \frac{g'(X)}{g(X)} \equiv -\frac{1}{\Lambda_N}, \tag{2.17}$$

where $-1/\Lambda_N$ is called the separation constant. The equation for $g(X)$ can be solved readily, giving

$$g(X) = g(0)\cdot \mathrm{e}^{-X/\Lambda_N}, \tag{2.18}$$

which shows that the nucleon flux decreases exponentially as a function of depth on a scale set by the *nucleonic attenuation length* Λ_N. The factorization implies that the functional form of the energy spectrum $G(E)$ is independent of depth. Assuming now a differential nucleon flux of the form

$$G(E) = E^{-(\gamma+1)}, \tag{2.19}$$

where $\gamma \sim 1.7$, we can solve for the inverse of the attenuation length giving

$$\frac{1}{\Lambda_N} = \frac{1}{\lambda_N}(1 - Z_{NN}), \tag{2.20}$$

where Z_{NN} is the spectrum weighted moment (see below).

The attenuation length for pions or kaons is defined similarly to that for nucleons. Typical values for this parameter are given in Tab. 2.3. In the above equation we introduced

Λ_N (nucleons)	Λ_π (pions)	Λ_K (kaons)
120	160	180

Tab. 2.3. Atmospheric attenuation lengths (gcm^{-2}) at 100 GeV particle energy [33].

the *spectrum weighted moment*

$$Z_{ij}(\gamma) = \int_0^1 (x_L)^{\gamma-1}F_{ij}(x_L)\mathrm{d}x_L. \tag{2.21}$$

This moment determines the uncorrelated flux of particles j produced by particles i in the atmosphere. In case $\gamma = 1$ we obtain with (2.14)

$$Z_{ij}(1) = \int_0^1 E_j\frac{\mathrm{d}n_{ij}(E_j, E_i)}{\mathrm{d}E_j}\mathrm{d}x_L = \frac{1}{E_i}\int_0^{E_i}\mathrm{d}E_j E_j\frac{\mathrm{d}n_{ij}(E_j, E_i)}{\mathrm{d}E_j}, \tag{2.22}$$

which is *the average fraction of interaction energy E_i going into particle type j*. For $\gamma > 1$, the factor $x_L^{\gamma-1}$ diminishes the significance of the inclusive cross section for $x_L \sim 0$, i.e. the central region. Thus, in this case, the uncorrelated fluxes depend mainly on the behaviour of the inclusive cross section in the fragmentation region. This is exactly the region where scaling works best and thus where Approximation A is most valid.

produced particle	projectile		
	p	π^+	K^+
p	0.263	-	-
n	0.035	-	-
π^+	0.046	0.243	0.030
π^-	0.033	0.028	0.022
π^0	0.039	0.098	0.026
K^+	0.0090	0.0067	0.211
K^-	0.0028	0.0067	0.012

Tab. 2.4. Indicative values for the spectrum weighted moments Z_{ij} for hadrons on air nulei [33].

In practice, γ is larger than 1 for primary particle energies above ~ 1 GeV. In Tab. 2.4 indicative values of the moments Z_{ij} for protons, pions and kaons on air nuclei are given, evaluated at $\gamma = 1.7$ and taking a mean air nucleus mass $A = 14.5$. Since particle production in nucleon-nucleus interactions proceeds via the strong interaction mechanism, isospin is a conserved quantity. The inclusive production cross section of mesons is thus invariant under isospin transformations. This means that the spectrum weighted moments Z_{ij} are the same for any combination of particles i, j from the same isospin multiplet, e.g. $Z_{p\pi\pm} = Z_{n\pi\mp}$. For the total nucleon flux we now find

$$N(E, X) = g(X) \cdot E^{-(\gamma+1)} \equiv g(0)\mathrm{e}^{-X/\Lambda_\mathrm{N}} E^{-(\gamma+1)}. \tag{2.23}$$

Since $N(E, 0) = g(0)E^{-(\gamma+1)} = N_0(E)$, this is equal to

$$N(E, X) = N_0(E)\mathrm{e}^{-X/\Lambda_\mathrm{N}}. \tag{2.24}$$

The flux for protons and neutrons separately can now easily be found from Eq. (2.16) considering the spectral moments Z_{pp} and Z_{np} for proton production and the spectral moments Z_{nn} and Z_{pn} for neutron production. By isospin symmetry, $Z_{pn} = Z_{np}$ and $Z_{pp} = Z_{nn}$, which leads to the solution:

$$p(E, X) \pm n(E, X) = (p(E, 0) \pm n(E, 0))\,\mathrm{e}^{-X/\Lambda_{\mathrm{N}\pm}}, \tag{2.25}$$

where

$$\Lambda_{\mathrm{N}\pm} = \frac{\lambda_\mathrm{N}}{1 - Z_{pp} \mp Z_{pn}} \tag{2.26}$$

and $\lambda_p = \lambda_n$ has been assumed. The ratio of proton to neutron flux follows as

$$\frac{p(E, X)}{n(E, X)} = \frac{1 + \delta_0 \, \exp(-X/\Lambda^*)}{1 - \delta_0 \, \exp(-X/\Lambda^*)}, \tag{2.27}$$

where

$$\Lambda^* = \frac{\Lambda_+ - \Lambda_-}{\Lambda_+ \Lambda_-}, \tag{2.28}$$

$$\delta_0 = (p(E, 0) - n(E, 0))/(p(E, 0) + n(E, 0))$$

and

$$\Lambda_+ = \Lambda_N \ ; \quad \Lambda_- = \lambda_N(1 - Z_{pp} + Z_{pn})^{-1} \tag{2.29}$$

with $Z_{NN} = Z_{pp} + Z_{pn}$, the nucleonic spectral moment. With $\delta_0 \approx 0.82$, the ratio is close to 10 at the top of the atmosphere, gradually approaching 1 for depth $X \gg \Lambda^*$.

2.5.2 Transport of mesons

Secondary mesons are the driving force behind the initial shower development, because these mesons fuel the electromagnetic component via their decay to muons, electrons and photons. The most important production mechanism for pions is the nucleon-nucleon interaction. Limiting ourselves to this channel, we get the following expression for the π-meson flux:

$$\frac{d\Pi(E, X)}{dX} = -\left(\frac{1}{\lambda_\pi} + \frac{1}{d_\pi}\right)\Pi(E, X) + \frac{1}{\lambda_\pi}\int_0^1 \Pi(E/x_L)F_{\pi\pi}(x_L)\frac{dx_L}{x_L^2}$$
$$+ \frac{1}{\lambda_N}\int_0^1 N(E/x_L)F_{N\pi}(x_L)\frac{dx_L}{x_L^2} \tag{2.30}$$

with a similar equation for the K-meson spectrum (replacing Π by K and π by K). The first term in this equation represents the depletion of pions by interaction and decay, the second term represents the regeneration of pions by pion-nucleon interaction. The last term describes the production of pions by nucleons on air. Factorization of energy and depth dependence by $N(E, X) = N(E/x_L)g(X) \cong (\frac{E}{x_L})^{-(\gamma+1)}g(X)$, which is based on the assumed similarity of dependence on energy and depth for both nucleon and pion flux, this last term can be rewritten as

$$\frac{Z_{N\pi}}{\lambda_N}N_0(E)e^{-X/\Lambda_N}. \tag{2.31}$$

To solve Eq. (2.30), we again use factorization of the energy and depth dependence: $\Pi(E, X) = q(X)P(E)$. From the nucleonic term alone we find that $d\Pi(E, X)/dX \sim E^{-(\gamma+1)}$. So, it is natural to take $P(E) = E^{-(\gamma+1)}$ (assuming γ to be fixed). Rewriting Eq. (2.30) gives:

$$\frac{d\Pi(E, X)}{dX} = -\left(\frac{1}{\Lambda_\pi} + \frac{\epsilon_\pi}{EX\cos\theta}\right)\Pi(E, X) + \frac{Z_{N\pi}}{\lambda_N}N_0(E)e^{-X/\Lambda_N}. \tag{2.32}$$

This is a standard differential equation which can be solved as:

$$\Pi(E, X) = N_0(E)\frac{Z_{N\pi}}{\lambda_N}e^{-(X/\Lambda_\pi)}\int_0^X dX' \ e^{-X'/\Lambda_{eff}}\left(\frac{X'}{X}\right)^{\epsilon_\pi/E\cos\theta}, \tag{2.33}$$

where $1/\Lambda_{eff} \equiv 1/\Lambda_N - 1/\Lambda_\pi$ is an effective attenuation length. In the limit of very low and very high energy E, this expression for the meson-flux reduces to

$$\Pi(E, X) = N_0(E)\frac{Z_{N\pi}}{\lambda_N}e^{-(X/\Lambda_N)}\begin{cases} XE\cos\theta/\epsilon_\pi & E\cos\theta \ll \epsilon_\pi, \\ \Lambda_{eff}\left(e^{X/\Lambda_{eff}} - 1\right) & E\cos\theta \gg \epsilon_\pi. \end{cases} \tag{2.34}$$

As expected, for low energies meson decay is favored above interaction, thus leading to an $(E\cos\theta)$ dependence of the flux. For high energies, interaction is favored above decay, leading to an exponential decrease of the meson flux with increasing depth.

2.5.3 Meson decay

Due to their short lifetime, any mesons produced in a hadron or meson collision will quickly decay, thereby producing new mesons and leptons. The pi-meson spectrum is given by

$$\mathcal{D}_\pi(E, X) \equiv \frac{\mathrm{d}\Pi(E, X)}{\mathrm{d}X} = \frac{1}{d_\pi}\Pi(E, X), \tag{2.35}$$

with a similar equation for K-mesons. The production spectrum of secondaries from decay of these mesons is

$$\mathcal{P}_i(E, X) \equiv \frac{\mathrm{d}N_i(E, X)}{\mathrm{d}E\,\mathrm{d}X} = \sum_j \int_{E_{\min}}^{E_{\max}} \mathrm{d}E'_j \mathcal{D}_j(E'_j, X)\frac{\mathrm{d}n_{ji}(E_i, E'_j)}{\mathrm{d}E_i}. \tag{2.36}$$

Here, $\mathrm{d}n_{ji}(E_i, E'_j)/\mathrm{d}E_i$ is the inclusive spectrum of secondaries of type i from decay of type j particles with energy E'_j and mass M_j. For a two-body decay it is equal to

$$\frac{\mathrm{d}n_{ji}(E_i, E'_j)}{\mathrm{d}E_i} = \frac{B_{ji}}{P_{\mathrm{L}}}\frac{1}{1 - r_M} \tag{2.37}$$

where B_{ji} is the branching ratio for the decay channel $j \rightarrow i+$ any other particle, P_{L} is the lab momentum of the decaying parent particle and $r_M = (m_i/M_j)^2$ with m_i being the muon or neutrino mass from the meson decay. A full treatment of all decay channels is outside the scope of this chapter. Only the channels

$$\begin{aligned}
\pi^\pm &\rightarrow \mu^\pm + \nu_\mu(\bar{\nu}_\mu) \quad (\sim 100\%) \\
\mathrm{K}^\pm &\rightarrow \mu^\pm + \nu_\mu(\bar{\nu}_\mu) \quad (63.51\%)
\end{aligned} \tag{2.38}$$

will be considered here. For both of these channels the decay distribution is flat in energy as well as in solid angle (in the meson rest system). The limits on energy attainable for the muon and the neutrino are

$$\begin{array}{ccccc}
E\,r_M & \leq & E_\mu & \leq & E \\
0 & \leq & E_\nu & \leq & (1 - r_M)E.
\end{array} \tag{2.39}$$

As a rough guide, the mean lab energy of the muon and neutrino in both types of decays are

$$\langle E_\mu \rangle = 0.79(0.52)E, \qquad\qquad \langle E_\nu \rangle = 0.21(0.48)E, \tag{2.40}$$

where the numbers outside(inside) parentheses are for pion decay, and respectively for kaon decay.

2.5.4 Muon production

Now that we have obtained estimates for the meson production spectrum and the meson decay spectrum, the muon spectrum (differential in X) is obtained from Eq. (2.36) by summing over pion and kaon parents:

$$\mathcal{P}_\mu(E_\mu, X) = \frac{B_{\mu\pi}}{1 - r_\pi} \int_{E_\mu}^{E_\mu/r_\pi} \frac{\mathrm{d}E'_\pi}{E'_\pi}\frac{\Pi(E'_\pi, X)}{d_\pi} + \frac{B_{\mu\mathrm{K}}}{1 - r_\mathrm{K}} \int_{E_\mu}^{E_\mu/r_\mathrm{K}} \frac{\mathrm{d}E'_\mathrm{K}}{E'_\mathrm{K}}\frac{K(E'_\mathrm{K}, X)}{d_\mathrm{K}} \tag{2.41}$$

under the assumption that the mesons are highly relativistic. This equation is only valid if the energy loss by the muons in the atmosphere is neglected. The differential muon flux is found by integrating Eq. (2.41) over the slant depth

$$\mathcal{D}_\mu(E_\mu, X) \sim \frac{\mathrm{d}N_\mu(E_\mu)}{\mathrm{d}E_\mu} = \int_0^X \mathcal{P}_\mu(E, X')\mathrm{d}X'. \tag{2.42}$$

To solve this equation, we again consider the expression for the meson flux

$$\Pi(E, X) = N_0(E)\frac{Z_{\mathrm{N}\pi}}{\lambda_{\mathrm{N}}}\mathrm{e}^{-(X/\Lambda_\pi)}X^{-\epsilon_\pi/E\cos\theta}\int_0^X \mathrm{d}X'\ \mathrm{e}^{-X'/\Lambda_{\mathrm{eff}}}\ X'^{\epsilon_\pi/E\cos\theta}. \tag{2.43}$$

The exponent under the integral can be expanded into a power series and each term can be integrated separately. Taking only the first three terms of this expansion into account, the pion flux is transformed to

$$\begin{aligned}
\Pi(E, X) = &N_0(E)\frac{Z_{\mathrm{N}\pi}}{\lambda_{\mathrm{N}}}\mathrm{e}^{-(X/\Lambda_\pi)}X \\
&\left(\frac{1}{1 + \frac{\epsilon_\pi}{E\cos\theta}} - \frac{X/\Lambda_{\mathrm{eff}}}{2 + \frac{\epsilon_\pi}{E\cos\theta}} + \frac{(X/\Lambda_{\mathrm{eff}})^2}{2!\,(3 + \frac{\epsilon_\pi}{E\cos\theta})} - \cdots\right).
\end{aligned} \tag{2.44}$$

The production spectrum of muons has to be summed over the pion and kaon flux. Since both fluxes exhibit the same functional form, the summation is done *implicitly* over the identifier i, which produces the following result:

$$\begin{aligned}
\mathcal{P}_\mu(E_\mu, X) = &\frac{\epsilon_i}{X\cos\theta}\frac{B_{\mu i}}{1 - r_i}\int_{E_\mu}^{E_\mu/r_i}\frac{\mathrm{d}E_i'^2}{E_i'}\,N_0(E_i')\frac{Z_{\mathrm{N}i}}{\lambda_{\mathrm{N}}}\mathrm{e}^{-(X/\Lambda_i)}X \\
&\left(\frac{1}{1 + \frac{\epsilon_i}{E_i'\cos\theta}} - \frac{X/\Lambda_{\mathrm{eff}_i}}{2 + \frac{\epsilon_i}{E_i'\cos\theta}} + \frac{(X/\Lambda_{\mathrm{eff}_i})^2}{2!\,(3 + \frac{\epsilon_i}{E_i'\cos\theta})} - \cdots\right)
\end{aligned} \tag{2.45}$$

Introducing a variable $z = E_i'/E_\mu$ and assigning $N_0(E_i') = z^{-(\gamma+1)}N_0(E_\mu)$, this can be rewritten as

$$\begin{aligned}
\mathcal{P}_\mu(E_\mu, X) = &\xi_i(E_\mu)\frac{B_{\mu i}}{1 - r_i}\frac{Z_{\mathrm{N}i}}{\lambda_{\mathrm{N}}}\mathrm{e}^{-(X/\Lambda_i)}N_0(E_\mu) \\
&\int_1^{1/r_i}\frac{\mathrm{d}z}{z^{\gamma+2}}\left(\frac{1}{\xi_i(E_\mu) + z} - \frac{X/\Lambda_{\mathrm{eff}_i}}{\xi_i(E_\mu) + 2z} + \frac{(X/\Lambda_{\mathrm{eff}_i})^2}{2!\,\xi_i(E_\mu) + 3z} - \cdots\right),
\end{aligned} \tag{2.46}$$

where $\xi_i(E_\mu) = \epsilon_i/E_\mu\cos\theta$.

To find the differential muon flux, the integration over the slant depth X can be performed, effectively replacing the numerator of each term in brackets by an incomplete gamma function

$$\left(\frac{-1}{\Lambda_{\mathrm{eff}_i}}\right)^n\int_0^X \mathrm{d}X'\mathrm{e}^{-X'/\Lambda_{\mathrm{eff}_i}}X'^n, \tag{2.47}$$

where $n = 0,1,2,\cdots$. Under the reasonable assumption that $X \gg \Lambda_i$, the upper limit can be taken to infinity, replacing the incomplete gamma function by an integer factorial. The final expression for the muon flux then obtained is

$$\mathcal{D}_\mu(E_\mu, X) = \xi_i(E_\mu)\frac{B_{\mu i}}{1 - r_i}\frac{Z_{\mathrm{N}i}}{\lambda_{\mathrm{N}}}\Lambda_i N_0(E_\mu)$$

$$\int_1^{1/r_i}\frac{\mathrm{d}z}{z^{\gamma+2}}\left(\frac{1}{\xi_i(E_\mu) + z} - \frac{(\frac{\Lambda_i}{\Lambda_{\mathrm{N}}} - 1)}{\xi_i(E_\mu) + 2z} + \frac{(\frac{\Lambda_i}{\Lambda_{\mathrm{N}}} - 1)^2}{\xi_i(E_\mu) + 3z} - \cdots\right). \quad (2.48)$$

The above expression is integrable, but can for general γ only be expressed in terms of a class of hypergeometric functions, which are difficult to approximate numerically. We therefore adapt an expression [33] which interpolates between the high and low energy solutions of Eq. (2.48):

$$\mathcal{D}_\mu(E_\mu, X) \cong \frac{N_0(E_\mu)}{1 - Z_{\mathrm{NN}}}\left(\frac{B_{\mu i}\mathcal{R}_{\mu i}}{1 + \mathcal{S}_{\mu i}/\xi_i(E_\mu)}\right), \quad (2.49)$$

where

$$\mathcal{R}_{\mu i} \equiv \frac{Z_{\mathrm{N}i}(1 - r_i^{\gamma+1})}{(1 - r_i)(\gamma + 1)} \quad (2.50)$$

and

$$\mathcal{S}_{\mu i} \equiv \frac{(1 - r_i^{\gamma+1})(\gamma + 2)}{(1 - r_i^{\gamma+2})(\gamma + 1)}\frac{(\Lambda_i - \Lambda_{\mathrm{N}})}{\Lambda_i \ln(\Lambda_i/\Lambda_{\mathrm{N}})}. \quad (2.51)$$

Using specific values for the parameters in the above equations as found from experimental data, the following result is obtained:

$$\mathcal{D}_\mu(E_\mu, X) \cong 0.14\, E_\mu^{-2.7}\left\{\frac{1}{1 + \frac{1.1 E_\mu \cos\theta}{115\ \mathrm{GeV}}} + \frac{0.054}{1 + \frac{1.1 E_\mu \cos\theta}{850\ \mathrm{GeV}}}\right\}\quad (\mathrm{cm}^2\ \mathrm{s}^1\ \mathrm{sr}^1\ (\mathrm{GeV/c}))^{-1}, \quad (2.52)$$

where the first term in braces is the contribution from pions and the second term the contribution from kaons.

Equation (2.52) shows the qualitative behaviour of the muon flux as a function of zenith angle and energy (above ~ 10 GeV of muon energy). The two terms in braces show that the contribution to the muon flux from kaon decay becomes increasingly important with higher energies, with a maximum relative contribution of about 28% at asymptotically high energies. Further, the typical "decay terms" appear for both types of mesons, with energy scales of 115 GeV and 850 GeV.

2.5.5 Muon charge ratio

From the principle of charge conservation, one would naively expect the secondary charged-particle flux to reflect the mean charge composition of the primary cosmic rays. However, copious production of charged particles would eventually lead to a mean charge ratio near one, even with an excess of positively charged primaries.

So, there must be another basic reason why the ratio of positively to negatively charged muons is larger and *remains* larger than unity for all energies. The answer lies in the expression for the spectrum-weighted moment Z_{ij}, Eq. (2.21). Since the spectral index γ of primary cosmic rays is near 1.7, the moment's magnitude increases with increasing x^*, i.e. the forward fragmentation region (with $x^* \uparrow 1$) is most significant and in fact determines the secondary flux. The secondary flux thus reflects *the charge composition*

of the proton (or any other primary) and hence the charge ratio of secondary muons will be larger than one for all energies.

Using the equations for the secondary meson flux, as derived earlier, one can obtain a simple expression for the muon charge ratio. Up to muon energies of about 200 GeV (where the contribution to the muon flux from kaon decay is near 10% relative to that from pion decay), the pion flux alone gives a reasonable estimate of the muon flux. Consider now Eq. (2.30), split up for the negatively and positively charged pions. The spectral moments involved are $Z_{\pi^+\pi^-} = Z_{\pi^-\pi^+}, Z_{\pi^+\pi^+} = Z_{\pi^-\pi^-}, Z_{\mathrm{p}\pi^+} = Z_{\mathrm{n}\pi^-}$ and $Z_{\mathrm{p}\pi^-} = Z_{\mathrm{n}\pi^+}$, with the identities implied again by isospin invariance. Defining $\Delta_{\pi_\pm} = \Pi^+(E, X) \pm \Pi^-(E, X)$ and $\Delta_{\mathrm{N}_\pm} = p(E, X) \pm n(E, X)$, the differential equation for the pion flux is

$$\frac{\mathrm{d}\Delta_{\pi_\pm}}{\mathrm{d}X} = -\left(\frac{1}{\lambda_\pi} + \frac{1}{d_\pi}\right)\Delta_{\pi_\pm} + \frac{\Delta_{\pi_\pm}}{\lambda_\pi}(Z_{\pi^+\pi^+} \pm Z_{\pi^+\pi^-})$$
$$+ \frac{\Delta_{\mathrm{N}_\pm}}{\lambda_{\mathrm{N}}}(Z_{\mathrm{p}\pi^+} \pm Z_{\mathrm{p}\pi^-}). \tag{2.53}$$

Using the solution for the low energy limit of the meson flux Eq. (2.34), the ratio of positively to negatively charged muons is deduced as

$$R_\mu \equiv \frac{N_{\mu^+}}{N_{\mu^-}} = \frac{1 + \delta_0 \mathcal{A}\mathcal{B}}{1 - \delta_0 \mathcal{A}\mathcal{B}} \tag{2.54}$$

where

$$\mathcal{A} = (Z_{\mathrm{p}\pi^+} - Z_{\mathrm{p}\pi^-})/(Z_{\mathrm{p}\pi^+} + Z_{\mathrm{p}\pi^-}),$$
$$\mathcal{B} = \Lambda_-/\Lambda_+, \tag{2.55}$$

using the same definitions as in Sec. 2.5.1.

From the dependence on the spectrum-weighted moments, it follows that the muon charge ratio contains information on the charge- (and hence mass-) composition of the primary flux. For energies above about 200 GeV, kaon production leads to an extra increase of the muon charge ratio.

2.6 Atmospheric pressure variations

At the beginning of this chapter we have seen that the development of a cosmic-ray air shower depends, among others, on the atmospheric pressure. This implies that pressure variations should be taken into account for accurately normalized measurements of the cosmic-ray muon flux. If not, the error on the normalization of the muon flux will be increased by the variation of the muon flux through atmospheric pressure variations.

The mechanism by which a pressure variation influences the muon rate consists of a change in the ratio of mean decay to mean interaction length of the mesons producing the muons. An increased local temperature for example, will decrease the local density of the atmosphere, thereby increasing the mean interaction length. This leads to a higher fraction of mesons which will decay to muons before interacting. The muon rate at the earth's surface will thus increase. As an example, the CosmoAleph collaboration, performing cosmic-ray muon measurements using the HCAL subdetector of the ALEPH experiment, has measured a variation of the muon flux as a function of the local atmospheric pressure [36]. The anti-correlation between muon-rate and pressure is clearly seen (Fig. 2.5).
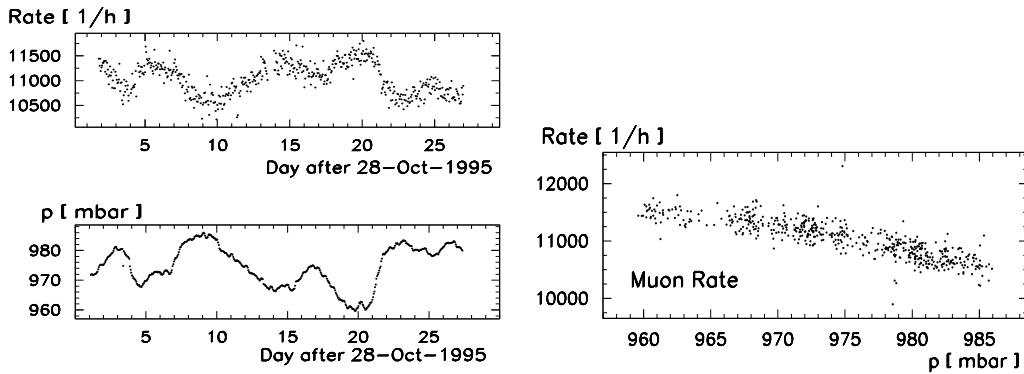
Fig. 2.5. Cosmic-ray muon rate versus atmospheric pressure as measured by the CosmoAleph experiment [36].

2.7 Solar wind and geomagnetic cutoff

On a scale of days up to years, the solar wind influences the low energy primary cosmic ray flux impinging on the earth's atmosphere. The earth's magnetic field and the solar wind, entangled with its own magnetic field, act as an effective shield for the low-energy part of primary cosmic rays. For primary energies above ca. 10 GeV per nucleon, the influence of the solar wind can be neglected. The earth's magnetic field itself acts as an effective shield for low energy primary cosmic rays. Depending on latitude, there exists a minimum energy for a particle to reach the earth's surface, the so-called geomagnetic cut-off energy, which has a value in the range of 0.5-15 GeV.

For ground-based cosmic muon experiments, measuring muon energies above $\sim$20 GeV, these mechanisms do not play a significant role in the determination of the absolute muon flux and the direction of the initiating primary particle.

Chapter 3

Status & motivation

The results of an up-to-date numerical estimation of the muon energy spectrum and the muon charge ratio are presented. The experimental results of former experiments are discussed. Finally, an accurate measurement of the muon momentum spectrum by the L3 detector is motivated by referring to the status of the neutrino oscillation hypothesis.

3.1 Theoretical status

3.1.1 Muon momentum spectrum

To gain insight into the quantitative behaviour of the cosmic-ray muon flux, a detailed treatment is necessary and this involves a numerical or semi-numerical evaluation of the transport equations. Today, special programs exist that treat the development of air showers and particle interactions numerically. A compilation of some up-to-date predictions for the differential muon spectrum is shown in Fig. 3.1. The predictions agree mutually up to about 30%. Of course one has to take into account the uncertainties on the parameters used for input to the models. As an estimate, the prediction by Bugaev et al. is thought to be accurate up to 10-15% between 10 and 1000 GeV/c[1]. This prediction can be fitted within a 2% accuracy to the following expression:

$$\mathcal{D}_\mu(p_\mu, X = 1030 \text{ gcm}^{-2}, \theta = 0°) = C \, p_\mu^{-(\gamma_0 + \gamma_1 \log p_\mu + \gamma_2 \log^2 p_\mu + \gamma_3 \log^3 p_\mu)}$$

(3.1)

with the parameters as given in Tab. 3.1.

3.1.2 Muon charge ratio

Various authors have calculated the muon charge ratio as a function of energy. A compilation of some up-to-date predictions for the muon charge ratio is shown in Fig. 3.2.

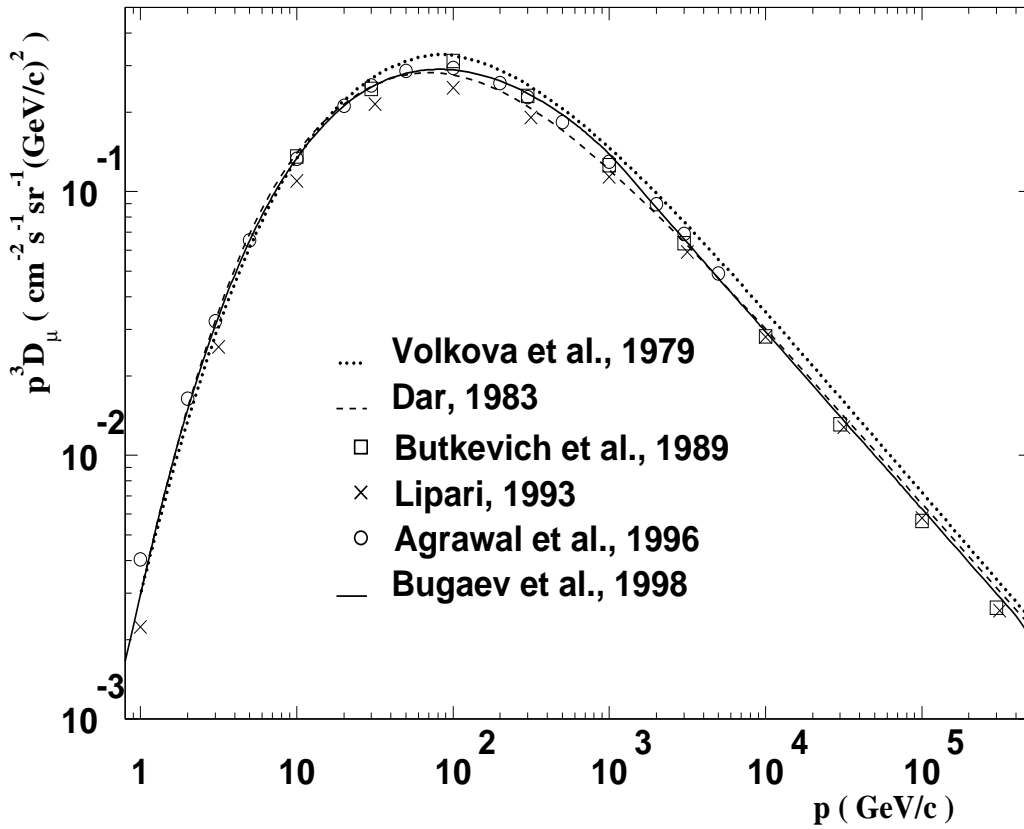[1] Private communication P. LeCoultre.

Fig. 3.1. A compilation of the vertical differential muon energy spectra as predicted by a number of up-to-date models [37].

The predictions agree mutually upto about 15%. They all predict a mean overall ratio of 1.25-1.30 below 100 GeV and an apparent increase of the ratio above this energy.

Momentum range (GeV/c)	C (cm^{-2}s^{-1}sr^{-1}GeV^{-1})	γ_0	γ_1	γ_2	γ_3
$1.0 - 9.2765 \cdot 10^2$	$2.950 \cdot 10^{-3}$	0.3061	1.2743	-0.2630	0.0252
$9.2765 \cdot 10^2 - 1.5878 \cdot 10^3$	$1.781 \cdot 10^{-2}$	1.7910	0.3040	0	0
$1.5878 \cdot 10^3 - 4.1625 \cdot 10^5$	$1.435 \cdot 10^1$	3.6720	0	0	0
$> 4.1625 \cdot 10^5$	10^3	4.0	0	0	0

Tab. 3.1. Fit parameters to calculated muon spectrum of Bugaev et al. [37].

3.2 Experimental status

3.2.1 Muon momentum spectrum

The cosmic-ray muon momentum spectrum has been measured several times already in different experiments, within an energy range from a few GeV to about 10^5 GeV
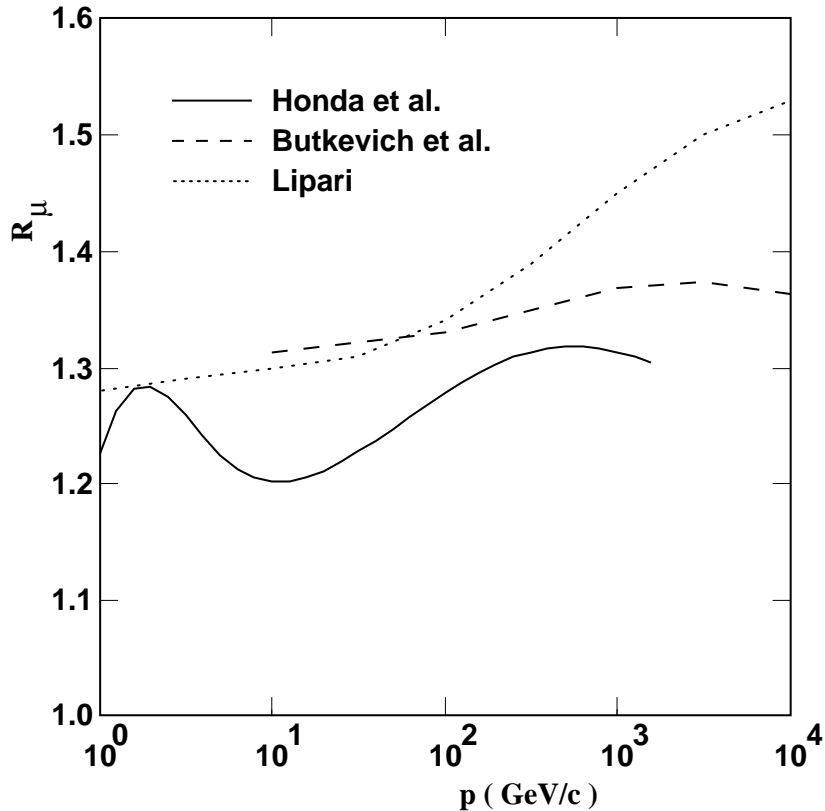
Fig. 3.2. A compilation of the vertical muon charge ratio as predicted by some up-to-date theories [32].

(see [37] and references therein). Experiments obtain the spectrum either in an *absolute*, a *non-absolute* or an *indirect* way. Absolute measurements contain all the necessary information to enable a normalization of the flux and are conducted by a magnetic or range spectrometer. Non-absolute measurements are normalized with respect to a previously measured absolute muon spectrum. These types of experiments usually consist of tracking chambers only, with no magnetic field present to obtain a momentum estimate. Indirectly-measuring experiments are located far underground or underwater where they measure the cosmic-ray muon intensity as a function of angle and depth below ground level. Such measurements provide a *depth-intensity relation*, which can be fitted to a theoretical model and subsequently converted to an absolute muon flux at the surface. This type of experiment is appropriate to measure the muon spectrum at TeV energies.

In Fig. 3.3, a compilation of the measured muon momentum spectrum is shown for momenta below about 1 TeV/c. The experiments shown are absolute measurements. A few things can be noted from this figure:

1. Most of the various measurements mutually disagree about the absolute value of the flux. The errors shown on the data points strongly suggest that this disagreement is due to systematic errors involved in the measurements and/or analysis. These errors amount to 20-30% in mean over all the experiments. Most of the experiments do not

state in their publications how they *define* the vertical flux, i.e. which method they used to measure the vertical component of the flux. This can lead to differences in the absolute normalization of the spectrum between different experiments.

2. Some measurements show relatively large statistical errors, on top of the previously mentioned apparent systematic shift.
3. There seems to be a slight disagreement about the slope of the spectrum at various energies.

The main improvement to the present-day data would, therefore, be to perform a measurement of which the systematic errors are under control. At the same time, the amount of data taken should be large enough to obtain statistical errors less than, or comparable to the systematic errors. To obtain these goals, the experiment and the relevant surroundings of it should be simulated well. This is necessary to obtain accurate estimates of the detector acceptance and efficiency and the muon energy loss as a function of angle. In case of a magnetic spectrometer, the smearing of the surface muon momentum by energy loss straggling and limited accuracy of the momentum measurement has to be taken into account. The shape of the muon spectrum as well as the absolute flux depend on the zenith angle. The variation of the spectrum as a function of the zenith angle is sensitive to the physics involved in the air-shower interactions (see Ch. 2), and is thus a measurement desirable for any cosmic-ray muon experiment.

In 1993, cosmic muon data taken with the L3 detector have partially been analyzed in a feasibility study [46]. Due to problems concerning the event reconstruction, at that time, an absolute flux could not be given. In this thesis, the same data are analyzed, but now the complete set of data is used and the L3 reconstruction and simulation software has been specially adapted for this particular purpose.

3.2.2 Muon charge ratio

To determine the charge of a muon track, it is necessary for an experiment utilizing tracking or drift chambers to utilize a magnetic field. The direction of curvature of the track in this field then provides the sign of the charge. The probability that the charge as measured by the experiment agrees with the real charge, depends on the precision with which the deviation of the muon track from a straight line can be determined. This deviation is called the *sagitta*. When the error on the sagitta increases, also the probability increases that the sign of the sagitta (i.e. the direction of deviation of the track with respect to a straight line) is wrong. Once this error is within the intrinsic accuracy of the measuring device, all significance on the charge measurement is lost: the *charge confusion* (see Sec. 7.7) becomes 100% (the chance of measuring the correct charge sign is as large as the chance of measuring the opposite sign).

In Fig. 3.4, a compilation of the measured charge ratio is shown for momenta below about 1 TeV/c. As can be seen, the measurements do not provide much information about the functional behaviour of the charge ratio versus momentum. The ratio averaged over all momenta from a few GeV to 1 TeV is about 1.25-1.30. With regard to these measurements it is important to realize that the charge ratio *must* be corrected for charge confusion. The unavoidable presence of charge confusion will always lead to a *measured* charge ratio *closer to one* than the actual charge ratio. When the charge confusion approaches 100%, the measured charge ratio will obviously approach 1.0. The level of charge confusion itself also naturally limits the maximum possible charge ratio that can be measured. It is rather strange that none of the experiments in Fig. 3.4 seem to correct for charge confusion.

The precision by which the muon momentum can be measured with the L3 detector amounts to circa 3.5% at 45 GeV/c, and rises linearly with increasing momentum. This
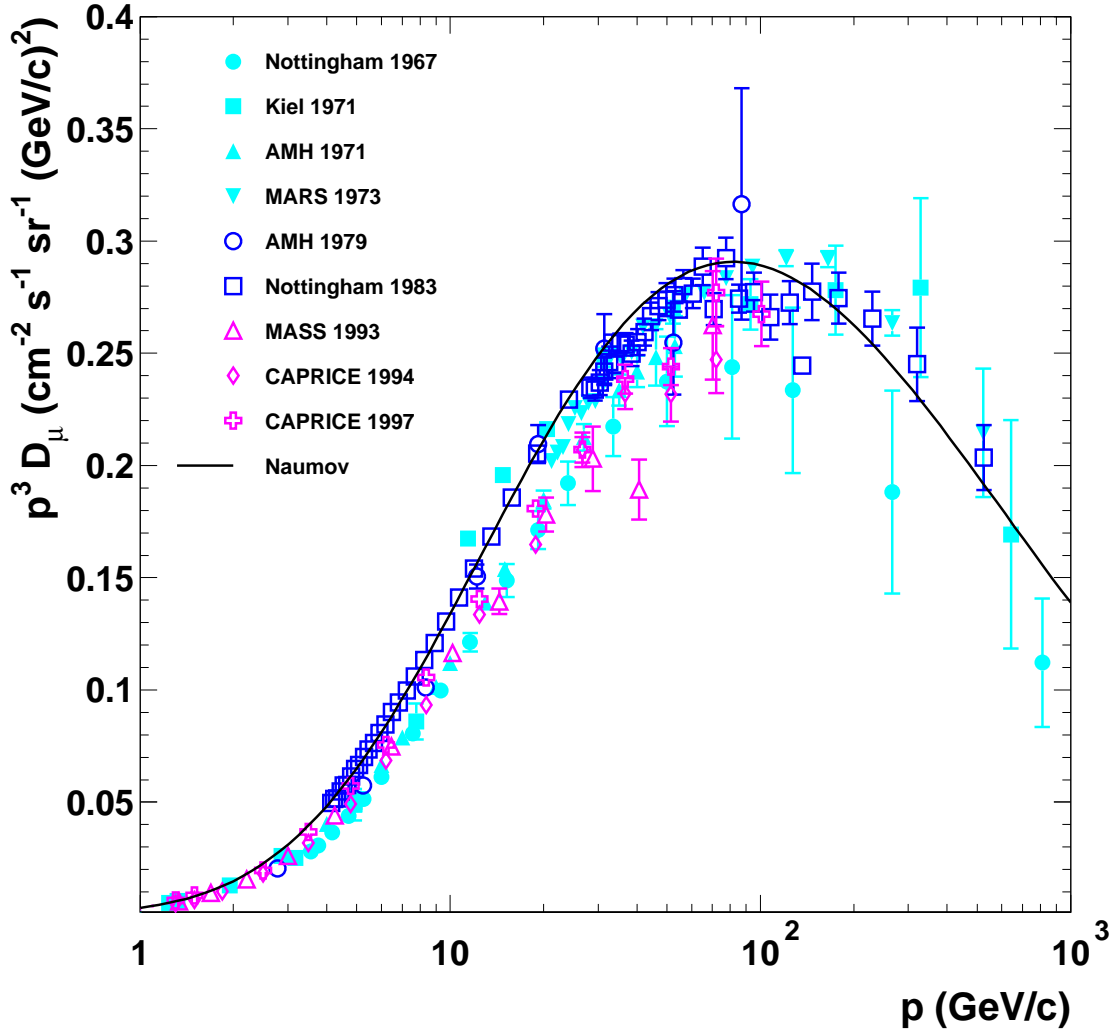
Fig. 3.3. A compilation of the measured vertical differential muon momentum spectra at sea level up to about 1 TeV momentum. The flux D_μ is multiplied by p^3. The solid curve is the result of a semi-analytical calculation (see Sec.2.5.4). The data are from [38; 39; 40; 41; 42; 43; 44; 45]

gives a momentum of about 3 TeV/c as the point where the error on the momentum is 100%. From analysis of dimuon data ($e^+e^- \rightarrow Z^0 \rightarrow \mu^+\mu^-(\gamma)$), the charge confusion near 45 GeV has been determined as $0.021 \pm 0.003\%$ [51]. This small value makes the L3 detector an ideal instrument to measure the cosmic-ray muon charge ratio with high precision over a large range of energies.

3.3 Motivation

The cosmic-ray muon spectrum is closely related to the cosmic-ray neutrino spectrum. This is because almost all of the muons and neutrinos have common parent particles,
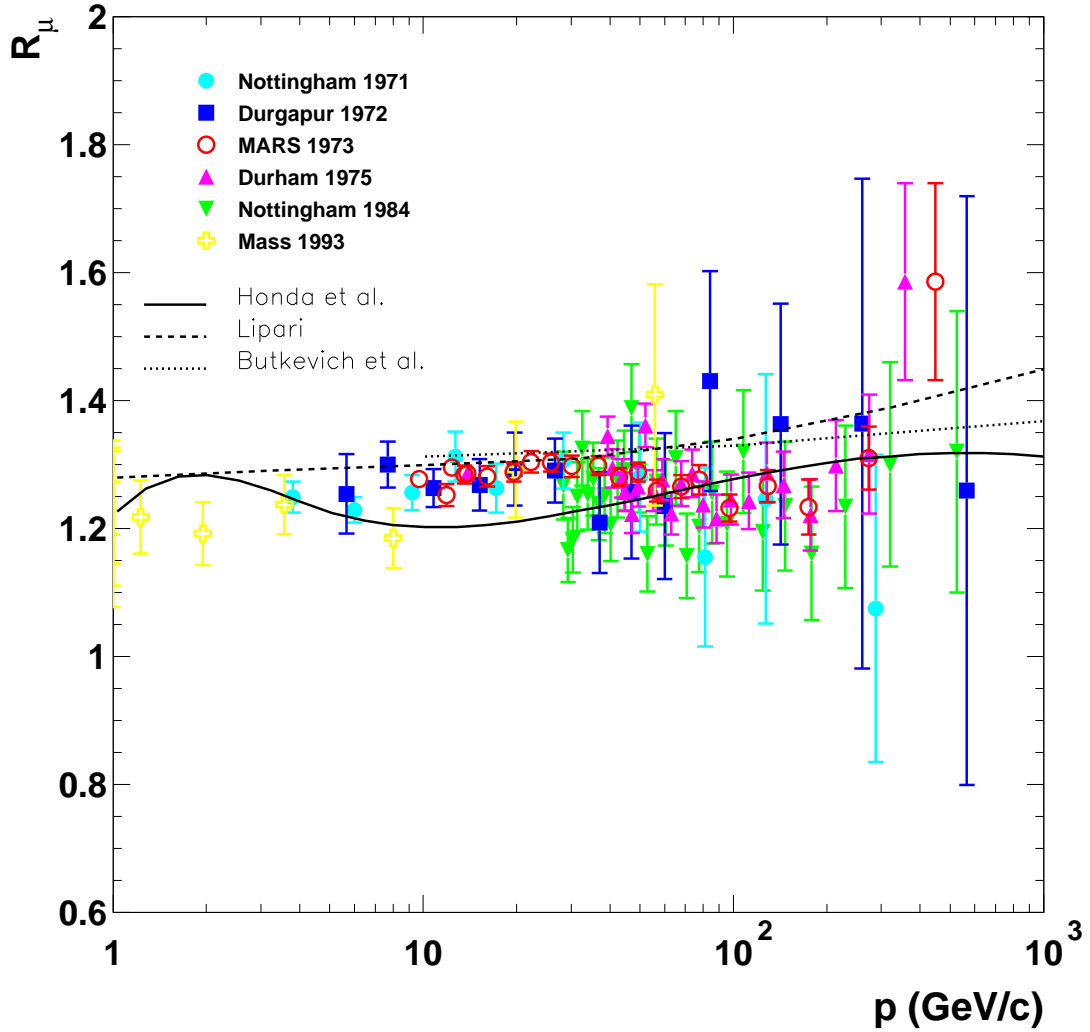
Fig. 3.4. A compilation of the measured near-vertical μ^+/μ^--ratio as a function of momentum. The curves are the result of some semi-analytical calculations. The data are from [47; 48; 49; 50; 44]

being the charged pions and kaons originating from the hadronic interactions. Only few of the muons and neutrinos have a different origin. The production chain is given by

$$\pi^{\pm}, \mathrm{K}^{\pm} \rightarrow \mu^{\pm} + \overset{(-)}{\nu}_{\mu}$$

$$\mu^{\pm} \rightarrow \mathrm{e}^{\pm} + \overset{(-)}{\nu}_{\mathrm{e}} + \overset{(-)}{\nu}_{\mu}. \tag{3.2}$$

Both particle spectra have to be folded with the production spectrum of the pions and kaons, while the neutrino spectrum has to be folded with the decay kinematics of the muon to produce its corresponding neutrino spectrum. The main uncertainty in the muon and neutrino spectra is in the meson production spectrum which is caused in turn by

the uncertainty in the primary cosmic-ray spectrum. Since the latter variation obviously induces a roughly *similar* effect in both the muon and neutrino spectra, the muon spectrum can be used to *fit* the ν_μ neutrino spectrum. Since it is mainly the absolute level of neutrino flux that is uncertain, it is necessary for this that the muon spectrum is measured up to the percentage level in absolute normalization. A precise determination of the neutrino spectrum at sea level is important for experiments which look for neutrino oscillations in the cosmic-ray neutrino flux.

3.3.1 Neutrino oscillations

Until recently, the experimentally determined mass of any neutrino was compatible with zero. The upper limits on their masses together with the confidence level are given in Tab. 3.2. Several experiments [53; 54; 55; 56; 57] found a cosmic-ray neutrino flux

Neutrino flavour	mass	confidence level (%)
ν_e	< 15 eV	see [52]
ν_μ	< 0.19 MeV	90
ν_τ	< 18.2 MeV	95

Tab. 3.2. Upper limits on the neutrino masses as known by 1999 [52].

which showed enrichments or depletions of certain neutrino flavours when compared to a Monte Carlo model. The evidence was, however, not convincing and sometimes even contradictory between different experiments. Recently, the Superkamiokande experiment [58; 59] announced a similar finding, but now the effect was convincing. Superkamiokande measured the neutrino flux of the electron and muon flavours as a function of zenith angle for energies below about 10 GeV. For the downward direction they measured directly the neutrino flux from air showers. For the upward direction, the neutrino flux of air showers at the opposite side of the earth was measured. The results of the measurements were compared to the corresponding simulations and demonstrated two things:

– The measured ν_e flux agreed with the expected flux for this flavour, for all zenith angles from 0 to 180 degrees.
– The measured ν_μ flux showed a depletion with respect to the expected flux. This depletion was compatible with zero near the local zenith and increased as a function of zenith angle to reach a maximum at 180 degrees.

Apparently, part of the ν_μ flux had disappeared, depending more or less linearly on the path length the neutrinos had covered from their production to their detection (the *baseline*). This result can be explained by assuming that neutrinos can change flavour. The necessary conditions for such *flavour oscillations* are that at least one of the masses of the neutrino flavours is different from the others and that individual lepton numbers are not conserved. In the current case, the ν_μ neutrino could change flavour to either the ν_e or ν_τ, or to an unknown "sterile" (non-interacting) neutrino. Transformation into ν_e neutrino is, however, excluded by the results of the CHOOZ experiment [60] and by the measured ν_e flux.

   The probability that a neutrino changes flavour from type i to type j in traversing a baseline L is given by

$$P_{\nu_i \to \nu_j} = \sin^2(2\theta)\sin^2(\pi L/L_{\text{osc}}), \tag{3.3}$$

where

$$L_{\text{osc}} \approx 2.48 \text{ km } \frac{E_\nu(\text{GeV})}{\Delta m^2(\text{eV}^2)}, \tag{3.4}$$

$\Delta m^2 = m_i^2 - m_j^2$, with m_i and m_j being the masses of the neutrino mass-eigenstates and θ is the mixing-angle [33]. Assuming such oscillations to explain the ν_μ deficit, Superkamiokande found $5 \times 10^{-4} < \Delta m^2 < 6 \times 10^{-3}$ eV^2 and $\sin^2(2\theta) > 0.82$ as the most probable parameter values [58; 59].

From Eq. (3.2), one would naively expect a ratio of muon-like over electron-like neutrinos of

$$\frac{\mu}{\text{e}} \equiv \frac{\nu_\mu + \overline{\nu}_\mu}{\nu_{\text{e}} + \overline{\nu}_{\text{e}}} = 2. \tag{3.5}$$

Since low-energy muons will decay before reaching the earth surface this is indeed what is expected for low energies. On the other hand, high-energy muons will not all decay so that this ratio will increase as a function of energy. Simulations show that for neutrino energies from about 0.1 - 1.0 GeV, the value of $\frac{\mu}{\text{e}}$ is indeed close to 2. This ratio also is relatively insensitive to any uncertainties in the parent meson flux, since these will largely cancel due to their similar effect on both neutrino flavours. For a comparison with Monte Carlo models the "ratio of ratios"

$$R \equiv \frac{(\mu/\text{e})_{\text{Data}}}{(\mu/\text{e})_{\text{MC}}} \tag{3.6}$$

is determined in order to be less dependent on normalization. A Monte Carlo model predicting the same ratio as is being measured, will lead to $R = 1$. Any deviation of the measurements from the Monte Carlo model will result in an R-value different from 1. Superkamiokande found [58; 59]

$$\begin{aligned} R =&0.61 \pm 0.03 \pm 0.05 &\text{(sub-GeV)} \\ &0.66 \pm 0.06 \pm 0.08 &\text{(multi-GeV)} \end{aligned} \tag{3.7}$$

for the ratio (the sub-GeV notation stands for a visible energy in the detector less than 1.33 GeV and electron (or muon) momentum larger than 100 MeV/c (200 MeV/c), while the multi-GeV notation stands for $E_\nu \gtrsim 1$ GeV). The first errors are statistical while the second errors are systematic in nature. The larger part of the systematic uncertainty is due to the uncertainty of the simulated (μ/e) ratio.

In Figs. 3.5 and 3.6, the ratios predicted by a number of models are shown for both energy regions [32]. All models are evaluated for the Kamioka site in Japan. The uncertainties in the (μ/e) ratio can be reduced by a determination of the neutrino spectrum from accurate measurements of the muon spectrum.

The L3 experiment measures the cosmic-ray muon energy spectrum above ca. 15 GeV. This means that the ν_μ spectrum can be normalized above about 20 GeV. This leads to a prediction of the number of up-going muons in for instance the Kamiokande experiment. Today, this number has an uncertainty of about 30%. The L3 experiment can reduce this uncertainty to about 5%, allowing for a test of the neutrino oscillation hypothesis, more strict than available today.
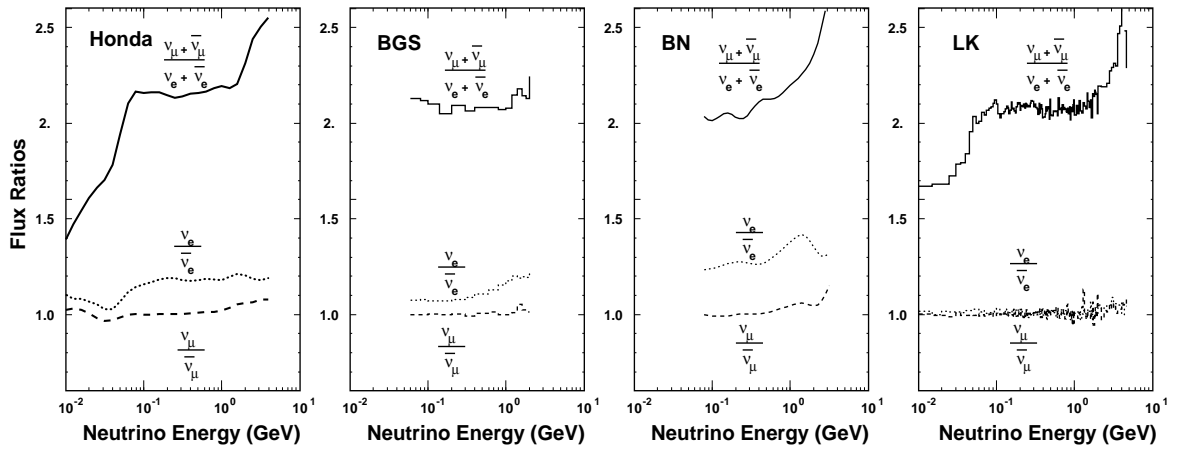
Fig. 3.5: The predicted ratio of muon-like over electron-like neutrinos for sub-GeV energies, calculated for the Kamioka site for four different models [32]. Honda are from [32], BGS from [61], BN from [62] and LK from [63].
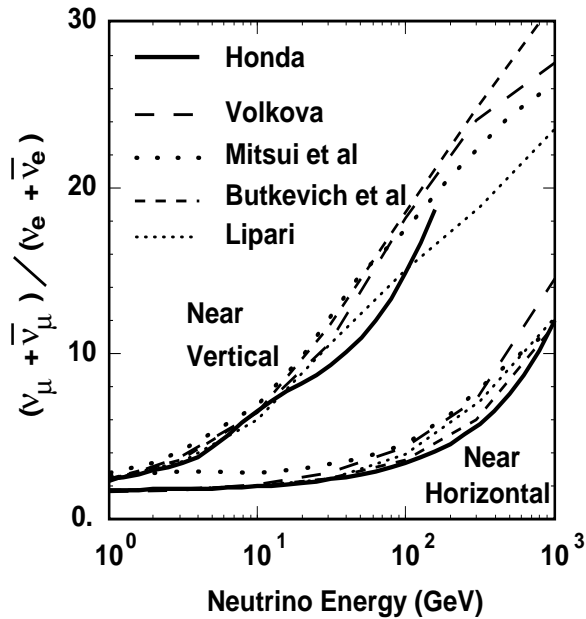

Fig. 3.6: The predicted ratio of muon-like over electron-like neutrinos for multi-GeV energies, calculated for the Kamioka site for four different models [32]. Honda are from [32], Volkova from [64], Mitsui et al. from [65], Butkevich et al. from [66] and Lipari from [67].

Chapter 4

Experimental setup

The data used for the current analysis were collected at CERN, near Geneva, Switzerland. At a varying depth of about 50 to 170 meters below ground level and located between the Jura mountains and lake Geneva, a Large Electron-Positron accelerator ring (LEP) provides high energy particles which collide with each other at four equidistant points along its circumference. Linear accelerators and subsequent pre-accelerator rings as the PS and SPS provide the particles with the necessary energy before injection into the LEP ring. The particles resulting from the collisions are collected by sophisticated detectors, one at each of the four vertex points along the ring. One of these, referenced by the poetic name "L3", provides an excellent environment for the study of muons, either created by the collisions at its vertex or by particle collisions high in the earth's atmosphere. In this chapter we will describe the L3 detector, especially those parts of it relevant for cosmic-ray muon detection during the 1991 dedicated cosmics run. The experimental halls and the geophysical circumstances are described. The special trigger used in these types of runs is explained.

4.1 The L3 detector

The L3 detector [27; 68; 69] is designed to measure events containing photons, electrons and/or muons. Subdetectors, positioned inside each other like the shells of a "russian doll" (Fig. 4.1), each measure a specific class of particles. Moving outward from the center of the detector, the following subdetectors are encountered (listed by their mnemonic):

❍ **SMD**   Silicon Microvertex Detector
The SMD is a tracking chamber for the purpose of measuring short-lived charged particles. It is positioned close to the vertex. It was installed prior to the 1993 data-taking period and became operational in 1994.

❍ **TEC**   Time Expansion Chamber
The TEC is a tracking chamber measuring charged particles within a radius of 46.9 cm. It is accompanied by the Forward Tracking Chamber (FTC).

❍ **ECAL**   Electromagnetic Calorimeter
The ECAL is an electromagnetic calorimeter made of BGO (Bismuth Germanium Oxyde) crystals which are arranged in a barrel and two end caps.
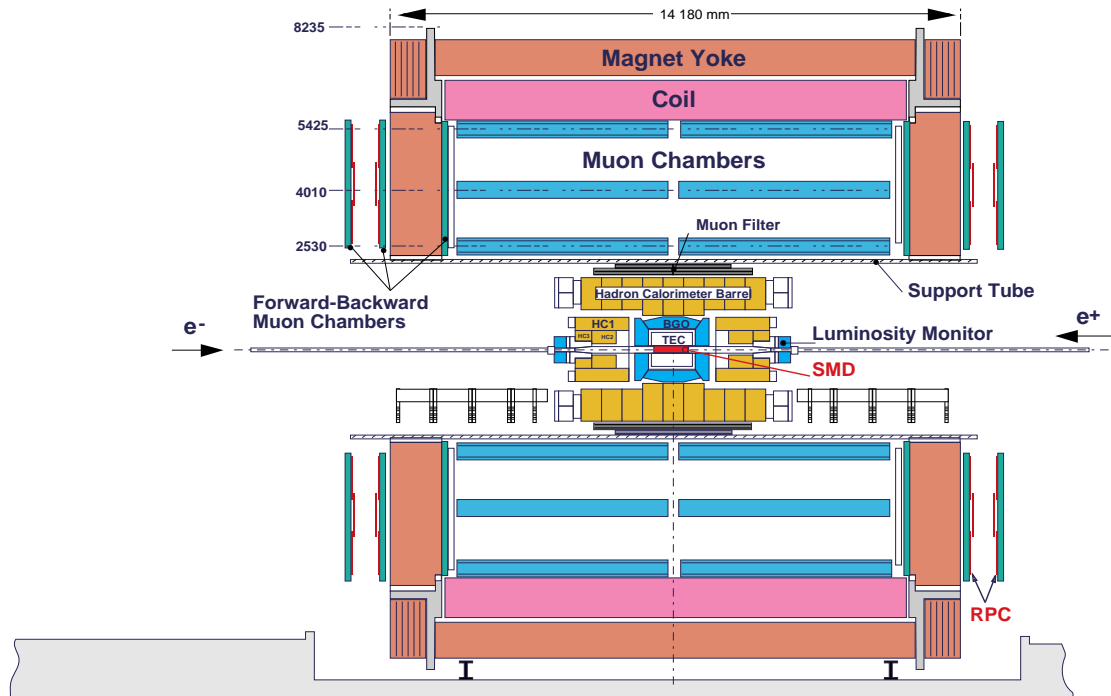
Fig. 4.1: Side view of the L3 detector as of 1997.

○ **LUMI**   Luminosity Monitor
The luminosity monitor measures the luminosity during data-taking. It consists of two disks of BGO crystals positioned around the beam pipe.

○ **SCNT**   Scintillators
The scintillation counters are arranged in a barrel and two end caps. They are located between the ECAL and HCAL detectors and around the HCAL end caps, respectively. Their primary function is to reject cosmic muons which contaminate the L3 muon data. During dedicated cosmic runs, they serve as one of the trigger devices.

○ **HCAL**   Hadronic Calorimeter
The hadronic calorimeter barrel and its two end caps consist of layers of depleted uranium interspersed with proportional wire chambers. Hadronic particles from the vertex encounter about 7 absorption lengths in the barrel.

○ **MFIL**   Muon Filter
The muon filter, positioned just at the inside of the support tube, contains brass absorber plates interspersed with layers of proportional drift chambers. Its use is as an additional absorber for leaking hadrons and as a supplement to the HCAL.

○ **MUCH**   Muon Chambers
The muon chambers consist of a barrel part of drift chambers and a forward/backward

part of drift chambers (**FBMU**) and resistive plate chambers (**RPC**). The forward/backward chambers were installed in 1994 at either side of both magnet doors. At the outside of the doors the drift chambers include two RPC chambers. The barrel chambers are built around three so-called P-chambers, measuring the track position in the transverse plane, and four Z-chambers, measuring the track position in longitudinal direction. The innermost and outermost P-chambers are sandwiched by two Z-chambers each.

○ **MGNT**   Magnet
The last part of the detector we encounter is the magnet, which supplies all the inner detectors with a longitudinal magnetic field of about 0.51 Tesla. It consists of an iron yoke, closed at the front and backside by two iron doors. The yoke and doors are guiding the field at the inner detectors along the Z-axis. Inside the yoke, a warm aluminium coil generates the necessary field while maintaining a current of near 30 kA. Since the resolving power of a magnet spectrometer is proportional to BL^2, where B is the field strength and L the lever arm, it is more efficient to choose for a moderate field of about 0.5 Tesla and a relatively long lever arm (~ 2.9m) for a given budget.

The essential parts for the measurement of cosmic-ray muons are the scintillators, the muon chambers and the magnet. These will be described in more detail below.

4.1.1 The scintillators

The scintillator detector consists of a barrel and two end caps (Fig. 4.2). The purpose of
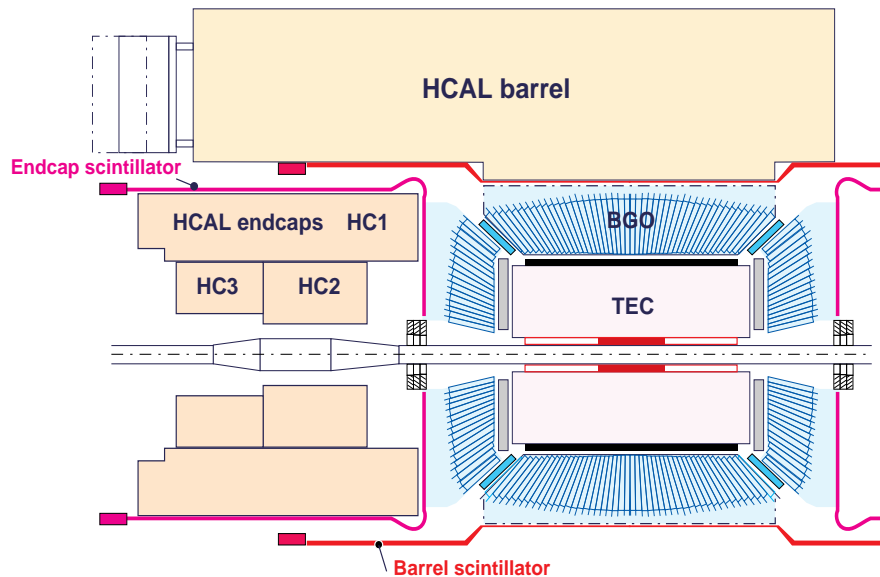

Fig. 4.2: The location of the barrel and endcap scintillators.

the endcaps is mainly their use as a bunch tagger and to reject cosmics by timing the track passage. In the current analysis of the 1991 cosmics runs only the barrel is used.

The barrel scintillator [70] is made of 30 tiles, arranged to fit closely to the inner dimensions of the HCAL barrel. Each tile consists of a piece of BC-416 plastic scintillator
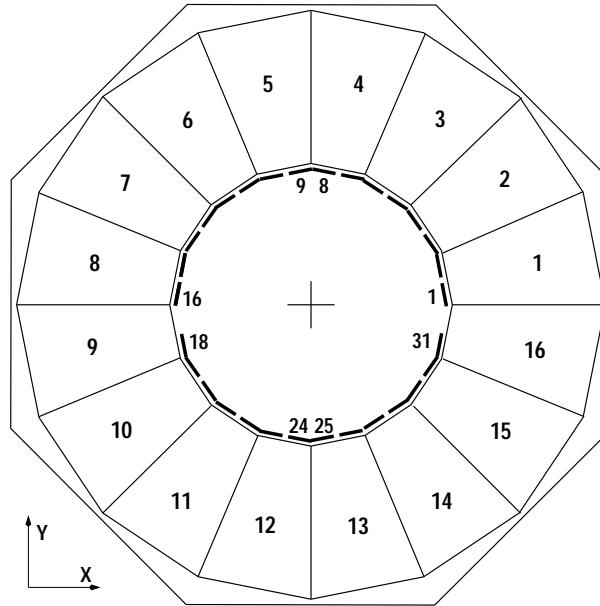
Fig. 4.3: Geometry of scintillator barrel in the transverse plane. Shown are the 16 HCAL barrel segments with the 30 scintillator tiles near their inner radius.

material, with a projected length of 2.9 meters, at both ends connected to plexiglass light guides. The tile is bent near its ends to follow the increasing inner radius of the HCAL barrel. Every two tiles are fitted closely together to cover one HCAL segment, except for two of them; these two have different dimensions to allow for the rails holding the ECAL calorimeter. As a consequence, tiles 17 and 32 do not exist physically, and their accompanying tiles 18 and 31 cover only half of the HCAL segment (Fig. 4.3). The radius from the vertex to the inner scintillator barrel part is about 885 mm, increasing to 974 mm at the ends (Fig. 4.2). The range covered by the barrel in polar angle (wrt beam direction) amounts to

$$|\cos\theta| < 0.83 \ \ (34° < \theta < 146°). \tag{4.1}$$

The light guides at both ends of a tile are connected to photomultiplier tubes (PMT) which convert the visible[1] scintillation light into a charge build-up at their output electrodes.

Signal processing. The charge output of the PMT is converted to a voltage which is guided to the electronics located in the so-called blockhouse. Here, it is amplified by a factor 10 and fed into an Analog to Digital Converter (ADC) as well as a discriminator (Fig. 4.4). The 15-bit ADC (LeCroy 1885) measures the integrated charge of the PMT during a fixed integration-time interval. The discriminator converts the analog signal into a logic pulse, where the comparison of a fixed threshold voltage with the signal voltage determines the transition from a logic-0 to a logic-1 level. The output of this discriminator is fed into a high-resolution Time to Digital Converter (TDC) as well as to a mean-timer. The 15-bit TDC (LeCroy 1875) has a resolution of about 0.1 ns per channel and is limited to a range of 400 ns. All these TDCs are stopped commonly by an external stop signal. Due to the uranium in the HCAL, there is a continuous noise signal present at the amplifier output which may lead to false triggers of the ADCs and TDCs. To suppress noise, the TDCs are enabled only just before a signal is expected to be present at their input.

---

[1] The visible light has been converted from UV light by a fluorescence material acting as a wavelength shifter.
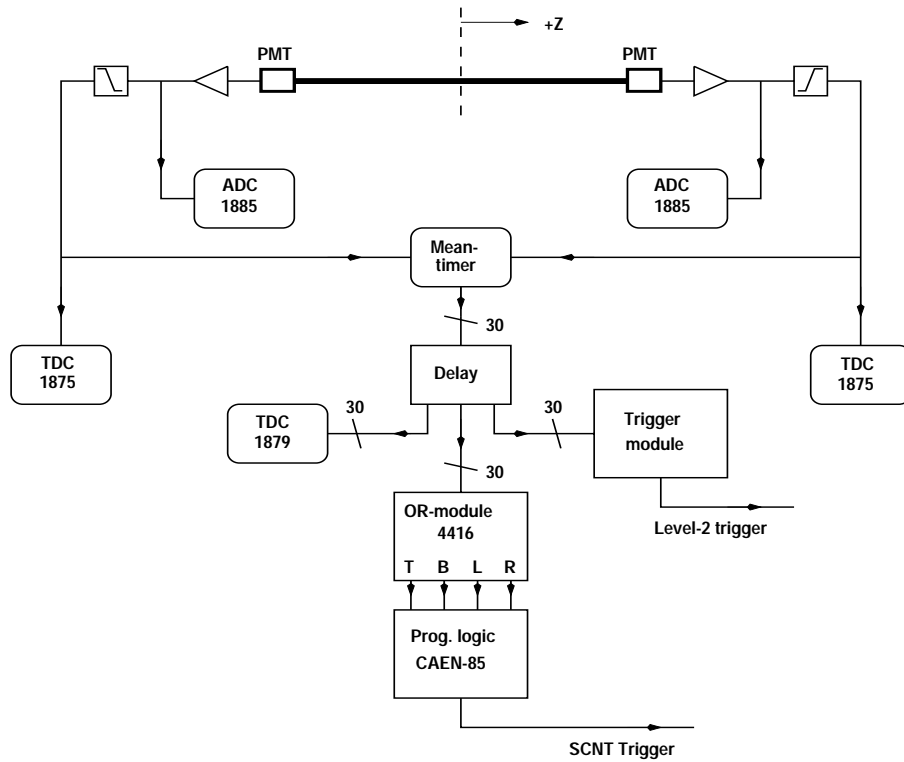
Fig. 4.4: Simplified scheme of the barrel scintillator signal flow.

The mean-timer builds the arithmetic mean in time (up to a fixed delay) of the pulses generated by the two PMT's at both ends of a scintillator tile. While the time of arrival of the light pulse at both ends of a tile depends on the longitudinal position of the particle crossing the tile, the mean of both these times is independent of the crossing position. All 30 mean-timer signals, one for each tile, are delayed by a fixed amount of time and subsequently fed into an "OR-module" (LeCroy 4416). This module delivers 4 signals at its output, T (top), B (bottom), L (left) and R (right), which are constructed from a logical OR of the top, bottom, left and right scintillator tiles, respectively.[2] The delayed mean-timer signals are also fed into a 10-bit mean-timer TDC (LeCroy 1879) with a resolution of about 10 ns per channel and a range of 10 μs, as well as a trigger module which redirects the correlated mean-timer outputs to the Level-2 and the calorimetric trigger. The mean-timer TDCs have a multi-hit capability of up to 6 hits.

The 4 signals from the OR-module serve as input to the "Programmable Logic module" (CAEN-85). The output of this module represents a (programmable) logic combination of the input signals and is used as the "scintillator trigger" which, together with the trigger signals from other subdetectors, is used to build the Level-1 trigger decision.

4.1.2 The muon chambers

During the 1991 dedicated cosmics run, only the barrel muon chambers were installed. For a discussion of the forward-backward muon chambers we refer to [71]. The barrel muon

---

[2] The top, bottom, left and right assignments are with respect to the horizontal and vertical axes through the vertex in the transverse plane of the detector.

chambers [69] are divided between 2 Ferris wheels (a "master" and a "slave", Fig. 4.5), each one consisting of 8 octants positioned concentric with respect to the beam axis around the support tube. Each of the 16 octants consists of 3 layers of drift chambers parallel to
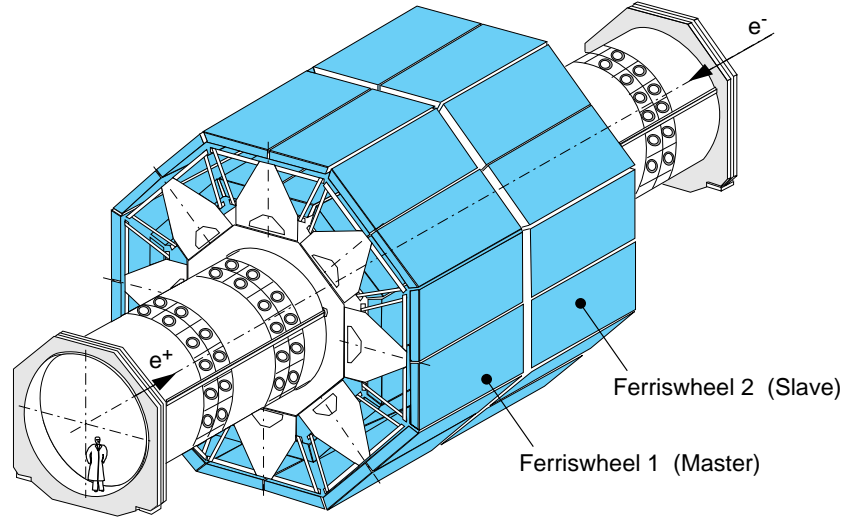

Fig. 4.5: View of both MUCH Ferris wheels installed around the support tube.

the beam-axis at mean radii of 2530 mm (inner chamber: MI), 4010 mm (middle chamber: MM) and 5425 mm (outer chamber: MO) (Fig. 4.6). The wires are directed along the beam axis. An MM chamber consists of two times 15 drift cells, where each cell contains 24 wires. The MI and MO chambers have 19 and two times 21 drift cells, respectively. Each of these cells contains only 16 wires. Since these chambers measure the muon-track coordinates in the perpendicular plane they are called *P-chambers*.

In addition, the inner and outer P-chambers are each sandwiched by *Z-chambers*. Each Z-chamber at either side of a P-chamber has 2 layers of single-wire drift-cells, where one layer is offset by half a cell with respect to the other layer, to resolve ambiguities. The wires are aligned perpendicular to the beam-axis, in order to measure the z-coordinates of a muon track. Each layer contains close to 58 drift cells, depending on the kind of the chamber.

The P-chambers are filled with a gas mixture of 61.5% argon and 38.5% ethane, while the Z-chambers are filled with a mixture of 91.5% argon and 8.5% methane. These mixtures, together with the high-voltage applied on the wires results in a drift velocity of about 48 μm/ns for the P-chambers and near 30 μm/ns for the Z-chambers.

Since the magnetic field is aligned parallel to the beam-axis, the curvature of the muon track, determining its transverse momentum, is measured by the P-chambers. This curvature results in a sagitta S, which is related to the transverse momentum as:

$$s \cong \frac{0.3 B_z L^2}{8 p_T} \; [mm] \tag{4.2}$$

where B_z is the longitudinal component of the magnetic field, L is the straight distance between the track intercepts with the innermost and outermost chamber in the bending
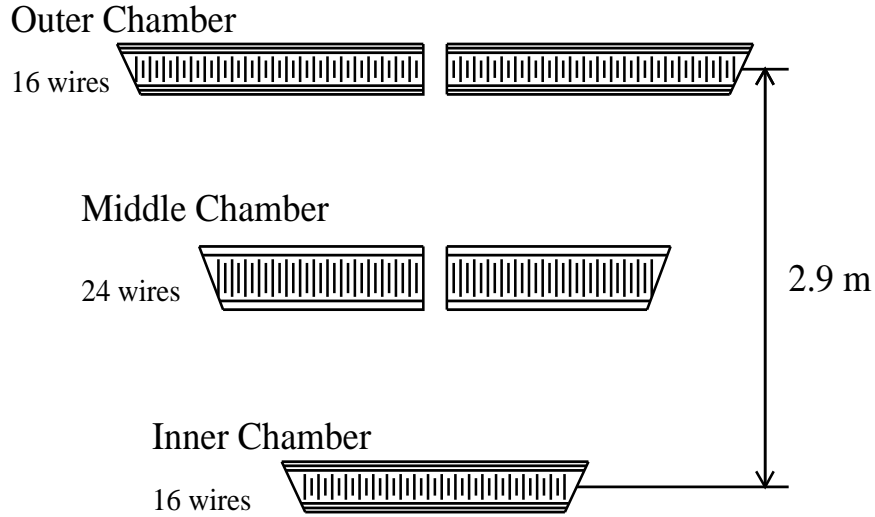
Outer Chamber

16 wires

Middle Chamber

24 wires

2.9 m

Inner Chamber

16 wires

Fig. 4.6: View of the three muon chambers in an octant.

plane and p_T is the transverse momentum (Fig. 4.7). A typical track with a momentum of
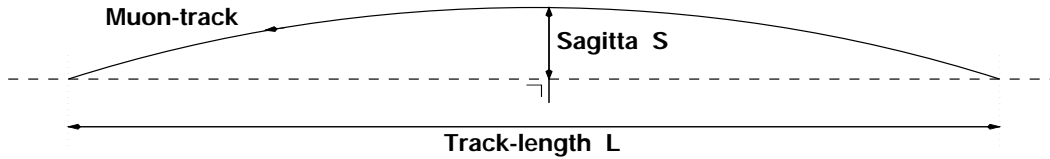
Muon-track

Sagitta S

Track-length L

Fig. 4.7: Definition of the sagitta s.

45 GeV has a sagitta s of ~ 3.7 mm. Knowing the sagitta and thus the related transverse momentum, the total momentum p of the track can be calculated from

$$p = p_\text{T} \sqrt{1 + \gamma^2},\tag{4.3}$$

where γ is the tangent of the pitch-angle of the track[3] as measured by the Z-chambers.

The single-wire resolution of the P and Z-chambers has been measured to be about 200μm and $\sim 670 \mu$m, respectively. Apart from its dependence on the single-wire resolution, the precision with which the track momentum can be measured depends on the relative alignment accuracy between the chambers in one octant, on the error introduced by multiple scattering in the MUCH volume and on a number of various small contributions, as the systematic error introduced by the magnetic-field determination along the track. Tracks crossing more than one octant also suffer from the relative alignment error between the octants, the magnitude of which generally out-sizes all other errors involved.

---

[3] If we neglect energy loss and scattering, a muon track passing through the magnetic field traverses a helical path. This (part of a) helix has a pitch angle $\arctan(\gamma)$.

For (non-radiative) Z^0 events, the precision of the momentum measurement $\Delta p/p$ has been determined to be $\sim 3.5\%$ at 45.6 GeV/c.

Signal processing. The avalanche of electrons created by an ionizing track in a muon chamber is picked up by the sense wires. For both P and Z-chambers the sense wires are connected in pairs. In case of the P-chambers, a wire in a master-octant is electrically connected with the corresponding wire of the opposite slave-octant. This means that P-hits on themselves do not contain any *direct* information about the z position of that hit. The Z-layers at the inner chamber contain only 1 wire across the entire length perpendicular to the beam-axis. For the Z-layers at the outer chambers, corresponding wires of the opposite chambers are electrically connected. Thus, also Z-hits do not contain *direct* information on the position of a hit along its corresponding wire. A combination of a set of P-hits
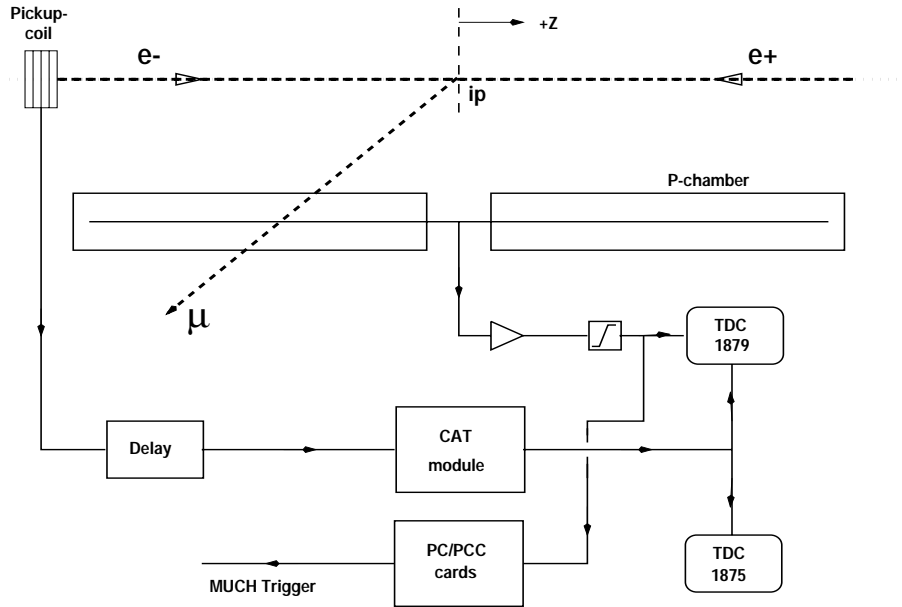

Fig. 4.8: Simplified scheme of the muon chamber signal flow. A muon created at the interaction point is passing through a P-chamber.

with a set of Z hits resolves all coordinate information, however, and the correct set of related P and Z-hits can be obtained from the "goodness of fit" of the combination. The "goodness-of-fit" is determined by the time the signal needs to propagate along the wires (at roughly 240 μm/ns) from the position of the hit to the pre-amplifiers between the two Ferris wheels (Fig. 4.8).

The output from the discriminators is directed by about 30 m of cable to the electronics in the blockhouse. This logical signal is then fed into a multi-hit TDC (LeCroy 1879) with a resolution of about 2.4 ns/channel and having 512 channels in total. The maximum possible time interval measured is thus ~ 1.2 μs, slightly larger than the maximum obtainable drift time.

To suppress noise, the TDCs are disabled when no interaction takes place. They are armed at a fixed time interval from the moment of interaction. From the moment a TDC is armed, it is continuously recording its input and actually triggers on the leading edge of an incoming signal. The TDCs are all stopped by a common stop signal which,

during normal LEP data-taking, is derived from a beam-pickup signal.[4] The time from the leading edge to the common stop signal is measured and gives the drift time (including all propagation time intervals) as further described in Sec. 5.4.2 below. The common stop signal is distributed by a special module (CAT) to all TDCs. During 1991, extra TDCs (LeCroy 1875) with a resolution of 0.025 ns/channel were installed which measure the arrival time of the stop signal at the 1879 TDCs. In this way any deviation in the exact time the stop-signal arrives at the TDC can be corrected for. During the cosmics runs on which this work is based, these common-stop TDCs were not yet installed.

To build the muon chamber Level-1 trigger, the discriminator outputs are monitored by Personality Cards (PC) which, in combination with other logic modules, determine if a track signature was found in the chambers. The recognition of tracks proceeds by comparing a specific set of wires with predefined "roads", e.g. it could require at least 6 wires being hit in all three chambers.

4.1.3 The global trigger

After a Level-1 trigger has occured, a more refined Level-2 trigger decision can be made, which is based on geometrical, time and energy-related properties of the subdetector signals. A positive Level-2 trigger passes the complete digitized data of all subdetectors to a Level-3 trigger which takes care of saving the data to tape and/or disk. A granularity increasing with the level of the trigger is necessary to reduce the time spent in making a trigger decision. Since only a small fraction of all Level-1 triggers are useful for physics analysis, the first trigger level should make a fast (thus coarse) decision. The Level-1 trigger rate is typically 8 Hz during normal L3 physics runs.

4.1.4 The magnet

The L3-magnet, supplying the tracking chambers with a magnetic field, consists of a solenoidal aluminium coil, a soft-iron yoke and two doors, being steel structures filled with iron, at its ends (Fig. 4.9). The magnet system is octagonally shaped and rests in a concrete cradle being the floor of the experimental hall. The coil consists of 168 windings, divided in 28 packages of 6 each. Each of these packages has a cooling system welded onto its inner and outer edges. The yoke has an outer radius of 7.9 m and serves as a field-return. Both halves of a door at either end of the magnet rest on a grease skate and can rotate around large hinges.

At the inside of the support tube the field produced by the magnet is probed by Hall plates, at the outside of the support tube by 992 magneto-resistors installed on the muon chambers. In addition, the absolute field value is continuously being measured by five NMR probes. Each of the magneto-resistors measures the field with a maximum error of ~ 20 Gauss. In the muon chambers the field is not exactly directed along the beam axis, but also contains a small radial component.

4.2 The L3 environment

While standard L3-physics is confined to the L3 detector itself, a measurement of cosmic-ray muons extends the physical environment far out to the slopy meadows near the Jura mountains. The main physical effects of the material below ground level through which a

---

[4] This signal gives the time at which the e^+ and e^- bunches collide at the vertex of the L3 detector.
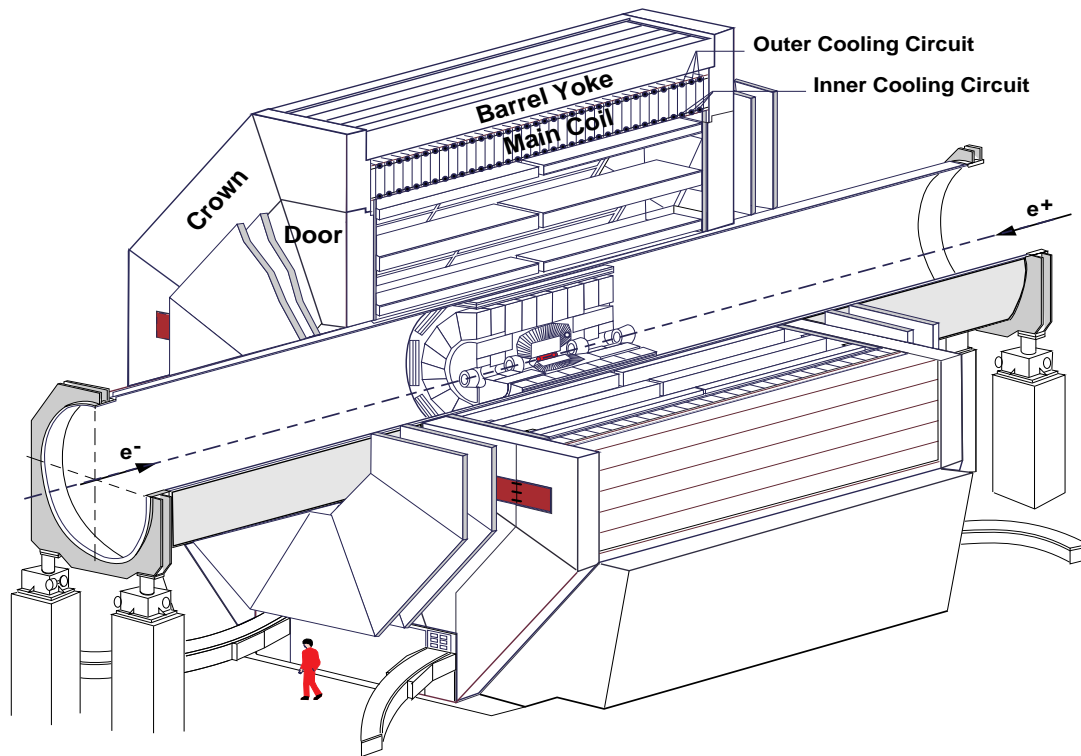
Fig. 4.9: The L3-magnet system showing the yoke, coil and doors (with FB-muon chambers).

cosmic-ray muon is passing are energy loss, scattering and, occasionally, interactions with its nuclei. To enable a simulation of these processes during the offline track reconstruction, the geological situation has to be known accurately. The aspects of the L3 environment with respect to its simulation can be grouped into 3 items:

❍ The location and dimensions of the main experimental hall underground, including the nearby parts of the tunnels, the shafts and the diverse caverns.
❍ The composition of the material below ground level, including the mapping of features like layers of material with specific properties.
❍ The location and structure of the buildings etc. at ground level and the structure of the ground level itself.

To start with the last item, it is obvious that effects like temporal storage of concrete blocks etc. cannot easily be accounted for. Even if that possibility would exist it should be compared to the error due to incomplete knowledge and/or simulation of the solid and lasting objects nearby. The errors made by neglecting these objects are assumed to be acceptable. Moreover, the mean surface energy of a muon being detected with L3 increases rapidly with increasing zenith angle, so that any obstruction not accounted for on the muon's path looses part of its significance as the angle grows. For nearly vertical muons, any obstructions are smeared out in the energy-loss distribution as well as in coordinate space due to scattering and a limited precision of measurement of the muon momentum and the simulation of its energy loss. For the purpose of this work, the simulation of the L3 environment does not include any objects at or above ground level and the ground level itself is assumed to be flat. This is a good approximation for zenith angles up to at least $60°$ (Fig. 4.10).

Fig. 4.10: An aerial view of the L3 site. The main building towards the middle of the picture is situated about 40 m above the detector.

Surface altitude above sealevel (m)	449
L3 depth wrt vertex (m)	44.78
L3 longitude $(^o.'.'')$	6.01.17060
L3 latitude $(^o.'.'')$	46.15.06578
L3 orientation of beam axis $(^o)$	37.505 West

Tab. 4.1. Geocentric coordinates of the L3 detector.

The location and the dimensions of all underground man-made caverns (filled with air at near-standard pressure and temperature) are accurately known from the blue-prints of the LEP-design. The LEP tunnel itself is inclined by 1.39% with respect to ground level. The reason of this slope was to make sure that the main part of the tunnel and all underground caverns are located in solid rock (molasse) while at the same time the access shafts are limited in depth (actually less than ~ 150 m). As a result, the L3 detector is on a slope of 1.39% with respect to ground level, in the vertical plane parallel to the beam axis. In September 1997, the exact coordinates of the surface directly overhead of L3 were measured[5], as given in Tab. 4.1. The surface layer in the region between Geneva and the

---

[5] Private communication P. LeCoultre.

Element	Z	Mass percentage			
		Molasse	Soil	Concrete, ord.	Concrete, shld.
H	1	.0080	.0211	.0115	.0020
C	6	.0430	.0109	.0136	.0022
O	8	.4850	.5646	.4996	.3187
Na	11	.0070	.0047	.0079	.0026
Mg	12	.0420	.0150	.0086	.0005
Al	13	.0370	.0352	.0355	.0132
Si	14	.2150	.2480	.2180	.0406
S	16	-	-	.0010	.1064
K	19	.0230	.0073	.0083	.0062
Ca	20	.1000	.0666	.1813	.0542
Mn	25	-	-	.0007	-
Fe	26	.0400	.0266	.0140	.0063
Ba	56	-	-	-	.4471

Tab. 4.2. Composition of molasse, soil, ordinary concrete and shielding concrete used at CERN [72].

Jura mountains is almost entirely composed of Subalpine Molasse with a thin layer of soil on top. The composition and the properties of the molasse are tabulated in Tab. 4.2 and Tab. 4.3, together with those of the soil on top of the molasse and two types of concrete used in CERN structures [72]. The most important ones, being the main hall, the main access shaft, the bypass shaft and an additional (now unused) shaft, have been modeled using the GEANT detector simulation package [73], which also simulates the complete L3 detector. Only a few necessary additional objects have been defined, as the concrete shielding positioned inside the main access shaft. Due to the small amount of material encountered by muons passing through this shaft, the shielding of 1.8 m thickness has a noticeable effect on muons below about 20 GeV. In Fig. 4.11 the surface layer, shafts,

Composite	Mean mass nr (A)	Density ρ (gcm^{-3})
Molasse	23.644	2.40
Soil	22.014	2.40
Concrete (ordinary)	24.083	2.20
Concrete (shielding)	74.279	3.30

Tab. 4.3. Physical properties of molasse, soil, ordinary concrete and shielding concrete used at CERN [72].

main hall and detector volume are shown. The scale of the volumes can be related to the figure standing at the bottom of the main access shaft. The coordinate axes shown are aligned with the L3 beam axis and originate at its vertex. The main hall, shafts and surface are tilted by 0.8° around the x-axis with respect to the detector. The position of the L3 detector with respect to the Jura mountains and the definition of the azimuth are shown in Fig. 4.12.
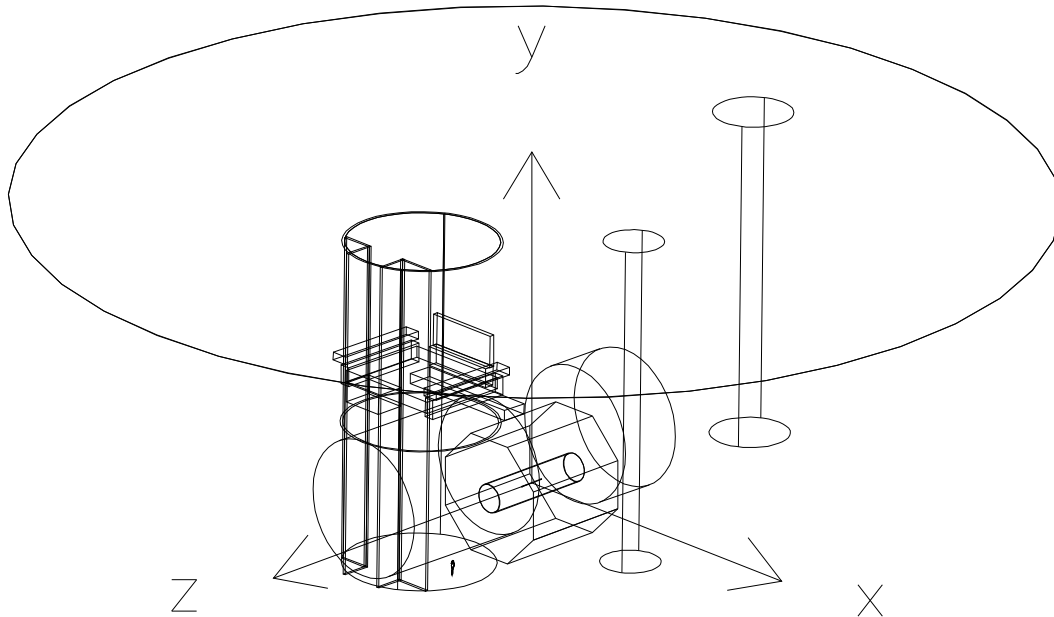
Fig. 4.11: View of the shafts, main hall and detector volume. For clarity the main hall part near the detector is not shown.
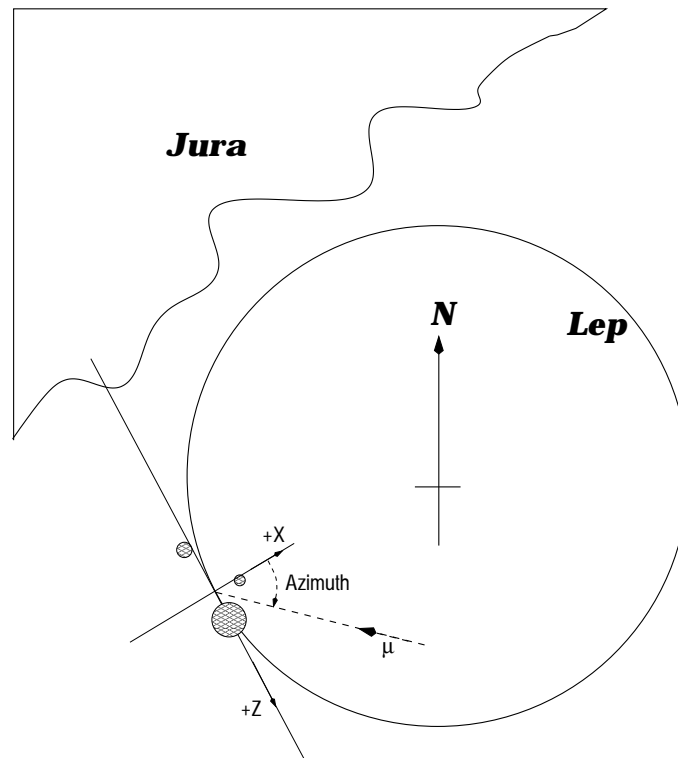

Fig. 4.12: Position of the shafts of the L3 site with respect to Jura mountains and definition of azimuth angle. The dimensions of the shafts are grossly exaggerated.
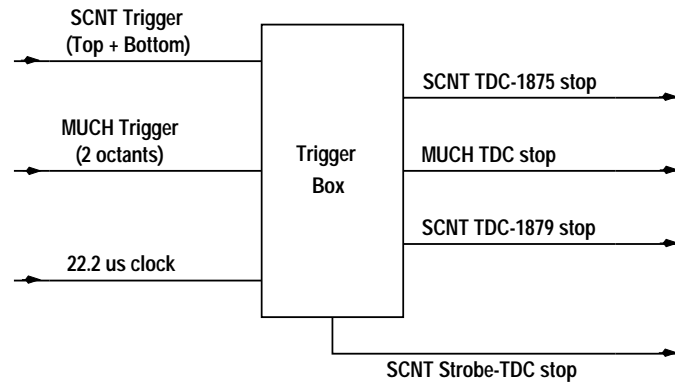
Fig. 4.13: Simplified scheme of the cosmic muon trigger logic.

4.3 The L3 cosmic-ray muon trigger

The trigger for cosmic-ray muon data taking [74; 75; 70] is different in many respects from the standard L3-trigger for beam events. Since cosmic-ray muons can enter the detector at any moment, there is no relation of the occurrence of an event with the beam-crossing signal. For this reason, cosmic-ray muons are taken in a self-triggering mode; the occurrence of a set of simultaneous subdetector triggers, triggers the data taking of all subdetectors involved. For the cosmic runs taken by L3 in 1991 for the purpose of the ECAL calorimeter calibration, the MUCH, SCNT and ECAL detectors were operational, but only the MUCH and SCNT sub-triggers were used to build the global trigger. The trigger settings were known under the name "COSMIC3" during the time of data taking [76].

Since a number of signals used in the trigger (and in the data-taking) depend on the beam-crossing signal, during the cosmic runs this signal was replaced by an artificial clock, being the clock source of the ECAL read-out electronics. The time a beam needs to complete one revolution in the LEP accelerator is 88.92446 μs. With four bunches per beam, equally spaced along the circumference, the beam-crossing frequency at L3 becomes 44.982 kHz leading to a beam-crossing interval of 22.231 μs which equals the artificial clock period. The timing of a cosmic-ray muon event was as follows:

– During 5 μs after the beam-gate signal, a gate is opened in which a cosmic-ray muon may enter the detector and produce signals for building the level-1 triggers.
– A positive global trigger decision was taken if
  – the scintillator barrel showed at least one hit in the upper half of its barrel tiles as well as in the lower half of the tiles, and in *coincidence*
  – the muon chambers showed the presence of a track in at least two octants, separated by at least one octant.
  The scintillator and muon chamber trigger are combined in the trigger box (Fig. 4.13), which sends the stop signals to the various TDCs.
– If a trigger decision is negative, the system is ready for a new event at the immediate next beam-crossing signal. If the trigger decision is positive, the electronics take 220 μs to digitize the subdetector data, before the system is ready for the next event.
– At a positive trigger decision the *Trigger-box* sends stop signals to the scintillator and muon chamber TDCs.

– In order to check the time stability of the scintillator TDC stop signal, this signal was send to a spare 1875 TDC (since 2 scintillator tiles are missing, there are 4 spare TDCs) and is called here the SCNT *strobe signal*. The TDC channel of this signal can be related to the time within the gate that a muon track was passing through the detector (see Sec. 7.4).

The self-triggering mode of the cosmics runs also implies that the drift time corrections to be applied to the muon-chamber hits might be (and in fact are) different from those applied for normal beam-beam events. Also the reconstruction of the scintillator-hit position along a tile depends on the relation between the start and stop of the 1875 TDCs, at least in principle, since the reconstruction of the z-position is based on the mean-times, which are independent of the position of a track-crossing point along the tile. A detailed discussion of these aspects related to time corrections is presented in the next chapter.

Muon reconstruction

The task of the muon reconstruction is to convert a set of low-level data to one or more muon-track objects. The low-level data are converted to geometrical addresses of the muon-chamber wires that are hit and their corresponding time stamps. In addition, the barrel scintillators deliver hit and timing information useful for reconstruction. This hit information is used to create muon tracks inside the L3 detector. In this chapter, we will explain the way in which tracks are reconstructed inside the muon chambers. Also the role of the scintillator barrel detector in the reconstruction process will be examined. The reconstruction algorithms per subdetector are discussed. Finally, the backtracking of the muon-chamber tracks towards the surface will be explained.

5.1 Introduction

The muon reconstruction software must be capable of handling standard Z^0 dimuon events, as well as cosmic-ray muons, from the data acquisition and from the simulation program. The dimuon data are important in the sense that they provide events with a well defined signature. The software can be calibrated and checked using these events. Tracks from this type of events always emerge from the vertex and are almost perpendicular to the muon chamber planes. The reconstruction software can be adapted to this particular signature. That's what is done for the standard L3 muon reconstruction software. Cosmic-ray muons emerge from any point and can cross the detector under any angle. Also their energy is not limited, as is the case in beam-beam events, but can take on any value allowed by nature. These circumstances make the reconstruction software more complex than in the case of standard dimuon event reconstruction.

A second aspect in which cosmic-ray muon events differ from normal dimuon events is the number of tracks present in a single event. Whereas for dimuon events there are only two tracks present, for cosmic-ray muons the number of tracks can occasionally be far larger than two. In most of the cases, however, only a single muon track is found per event. In this work, we concentrate on this latter type of single-muon events.

The reconstruction algorithms contain parameters which limit the possible types of tracks to be reconstructed. For instance, the maximum zenith angle a track can have in order to be reconstructed, is limited to $60°$. In the same sense, the upper limit on muon energy depends on the simulation software. The GEANT [73] package possesses an upper

limit on the energy of 10 TeV. Above this limit the muon interaction processes are not known well enough to be able to simulate them. The lower limit on particle energy inside the muon chambers is set to 3 GeV. This limit is chosen such that low-energy tracks, like electrons, are not reconstructed in the muon chambers.

The sequence in which data are processed by the reconstruction software can be divided into a few distinct blocks (Fig. 5.1). The input of the program consists of a number of
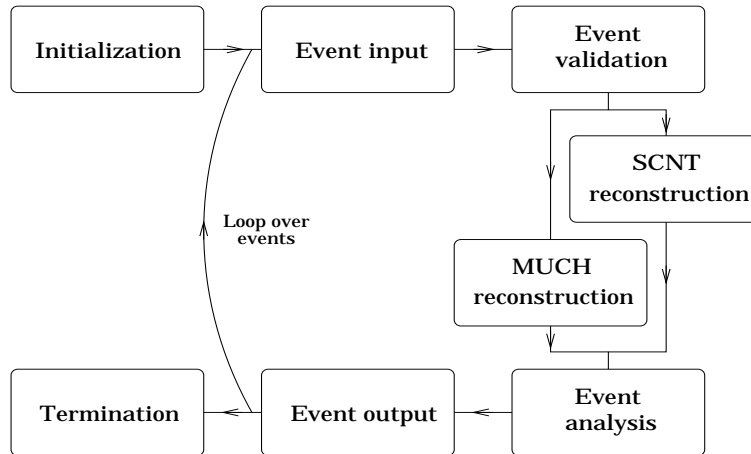

Fig. 5.1: Simplified flow-scheme of the REL3C offline reconstruction software.

runs, where each run contains a varying number of events. Before starting to process the input data, the program needs to be initialized, e.g. the geometry of the detector has to be defined, the various material properties have to be set and the data structures used by the program have to be declared. After the initialization, an event loop is entered. At termination of the program, this loop is left and the execution of the software is stopped in a controlled way. The event loop contains five blocks:

– *Input of event.* The data from one event are read into memory structures, separated per subdetector.
– *Validation of event.* The run number is checked versus the current run number and, if a difference is observed, time-dependent parameters are updated from the database for this new run. The event is checked on consistency of its contents. A validated event is passed to the next block, otherwise the event is skipped.
– *Reconstruction of event per subdetector.* The validated event contains data for each subdetector which was active during data-taking. For the BGO calibration cosmic-ray muon data, these were the barrel muon chambers, the barrel and end-cap scintillators and the electromagnetic calorimeter. The latter, however, is not used by our program, as are the scintillator end-caps[1]. Each subdetector requires its own specialized reconstruction algorithms, which convert the raw data at input to physical objects at output. These blocks are discussed in more detail in the sections to come.
– *Analysis of event.* The reconstructed objects are analyzed and (optionally) pass a selection. In case an interactive interface is being used these same objects are converted to graphics objects for display.

---

[1] The end-caps did not participate in the cosmic muon trigger.

– *Output of event.* Optionally, the event information can be stored in a selective way to a file or to a so-called ntuple. The ntuple contains all information on the physics objects, as they are returned by the reconstruction, necessary for a further, more detailed, analysis.

Monte-Carlo simulated data are processed in much the same way as real data. Merely the data structure itself is slightly different from that of real data.

5.2 Magnetic-field map

The muon momentum is measured from the curvature of the particle trajectory due to the magnetic field inside the muon chamber region. The radius of curvature depends on the actual muon momentum and the local magnetic field strength. The magnetic field inside the detector is, to zeroth order, constant with a magnitude of about 0.51 Tesla parallel to the detector's z-axis. The *real* field strength deviates from this constant value, depending on the coordinates, due to edge effects and the presence of materials with a non-unit magnetic permeability. Also the field *components* vary in strength since the direction of the field changes slightly as a function of spatial coordinates.

The trajectory of a particle with fixed momentum passing through a magnetic field with variable strength and direction will display a varying radius of curvature. This means that the local field should be known well by the reconstruction algorithms, if the momentum of a muon has to be determined accurately. The field component along the z-axis inside the L3 detector is measured by magneto-resistors and Hall plates (see Sec. 4.1.4). These measurements serve as calibration points for a global fit of the magnetic field inside the detector using specialized software, as the POISSON/SUPERFISH or TOSCA and OPERA packages. These programs return a magnetic field map in the form of a matrix containing the field values at certain positions in the magnetic volume. The field at a specific coordinate is found by interpolation of the sampled field strength from nearby points. Currently, the field-map matrix contains 60 points spread along the z-direction (from z = 0. to 5.9 m) and 60 points spread along the radial direction (from R = 0. to 5.9 m). From tests done on the magnetic field-map before 1989, the error on the z-component of the field was found to be [77]

$$\Delta B_z \leq 30 \text{ Gauss}. \tag{5.1}$$

An error of 20 Gauss in this field component was found to introduce a systematic error of about 10 μm [77] in the position of a muon chamber track segment (which consists of a set of 6 to 24 hits in one muon chamber). Furthermore, the absolute field strength was found to vary by about 0.1 Tesla over the muon chamber area, with larger variations near the magnet doors.

The field map for the muon-chamber region as used by L3 can be used without any modification for the purpose of cosmic-ray muon reconstruction. Outside the muon-chamber region (at R>5.9 m or $|z| > 5.9$ m), this field map does not apply anymore. Cosmic-ray muons have to be tracked back from the muon-chamber region, through the magnet coil and yoke up to the surface. So, we need an additional field map covering the region just outside the muon chambers to just outside the magnet volume.[2] The latter fieldmap was generated by the TOSCA program and is defined with 50 points spread along the local-octant y coordinate (from y = 5.45 to 7.90 m), 67 points spread along

---

[2] The residual field just outside the magnet volume and the earth magnetic field are neglected, since they have only a minor influence on the muon direction, compared to the uncertainties in the magnet coil/yoke field map.
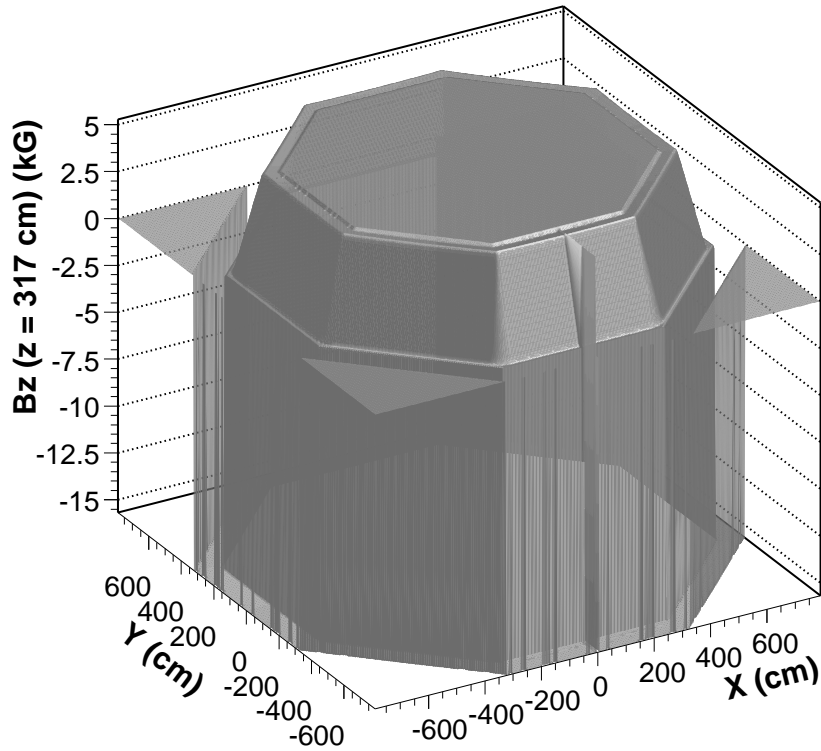
Fig. 5.2: The z component of the magnetic field strength as returned by the coil/yoke fieldmap, as a function of the x and y coordinates and at z = 3.17 meters. The coordinates are defined with respect to the detector vertex.

the local-octant x coordinate (from x = 0. to 3.30 m) and 24 points spread along the local-octant z coordinate (from z = 0. to 7.05 m). This region includes the muon-chamber area, but in case a point is inside this region, the standard L3 field map is used, since the yoke field map assumes a constant field in the muon-chamber region. In Fig. 5.2 the z-component of the field is shown as a function of the x and y coordinates, at z = 3.17 meters. The field in the magnet yoke is reversed as compared to that outside the yoke and amounts to slightly more than 1.5 Tesla.

5.3 Scintillator reconstruction

The barrel scintillators play an essential role in the reconstruction of the BGO calibration data, since the scintillators provide part of the trigger. The calibration of the scintillator barrel is described well in [70; 78]. As explained in Ch. 4, the start and stop signals related to the scintillator electronics are different with respect to normal data taking. This does not affect the scintillator reconstruction as used in this work. The timing corrections used for the BGO calibration data only depend (up to constant offsets, to be calibrated) on the scintillator time slewing, as explained below.

The trigger, as given by the scintillator barrel counters, results from two counters (one in the upper and one in the lower part of the barrel) which have been hit by a particle during its flight through the detector. The hit time is measured by a TDC and the amount of energy deposited in the tile is measured by an ADC. The number of scintillator tiles being hit in a single event is usually larger than two, due to the noise from the depleted uranium inside the hadron calorimeter, the production of delta-rays (knock-on electrons) by the muon and the possibility of multiple parallel cosmic-ray muons in a single trigger event.

For the reconstruction of a cosmic-ray muon, the only important parameters of a scintillator hit are the number of the tile which has been hit and the corresponding ADC (LeCroy 1885) readings. The TDC (LeCroy 1875) readings are not used. They provide a means of obtaining the longitudinal hit position along the counter, which can be displayed using the interactive interface. The only important time stamp for the reconstruction of cosmic-ray muons using the BGO calibration data, is the time as given by the mean-timer (Fig. 4.4). Any signal delivered by the photomultiplier tube (PMT) of a counter being hit, is amplified and sent through a discriminator. The signal at the amplifier can be described by [70]

$$V(t) = C(\mathrm{e}^{-t/\tau_{S_z}} - \mathrm{e}^{-t/\tau}), \qquad (5.2)$$

where C is a constant ($\sim$ -0.2), depending on the PMT and its electronics, τ_{S_z} is the decay constant of the scintillation light in the scintillator counter ($\sim$ 4 ns) and τ is the decay constant of the RC-network hanging on the PMT output ($\sim$ 2 ns). The pulse height and
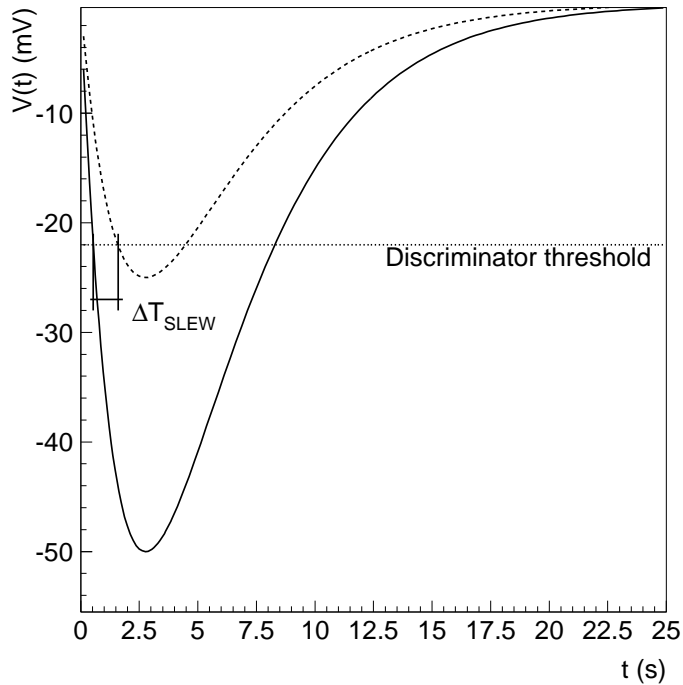

Fig. 5.3: Two signals from the PMT amplifier, passing the discriminator threshold. The resulting time slewing is caused by the different signal amplitudes.

shape of the signal are variable. They depend largely on the longitudinal position of the scintillator hit and the amplification factor of the PMT. This means that the time at which the signal will pass the threshold of the discriminator will vary. This variation is called the *time slewing*. In Fig. 5.3, two signals with different amplitudes are shown together with the resulting time slewing.

The amplitude of the signal is measured by the ADC counters for each PMT separately. The time slewing has to be applied as a correction to the time when the discriminator changes its output as a response to a signal. This slewing is defined relative to a calibration pulse height. The time of arrival of the scintillation light on the PMT, relative to a time
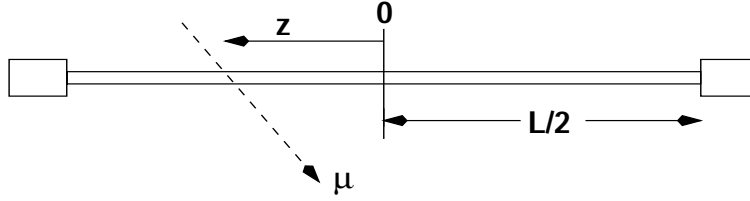

Fig. 5.4: A scintillator tile with a muon crossing it at ordinate z.

T_0 at which the muon is passing the scintillator tile, is found from

$$t_{1,2} = T_{0_{1,2}} + \frac{L/2 \pm z_{1,2}}{C_{S_z}}, \qquad (5.3)$$

where L is the total length of the scintillation counter, z is the position of the hit with respect to $z = 0$ and C_{S_z} is the effective propagation speed of the light in the counter (Fig. 5.4). The plus/minus signs apply to the PMT at $z \gtrless 0$. This time has to be corrected for the time slewing and is in addition converted to TDC counts according to

$$N_{\text{TDC}} = N_0 - (t_{1,2} + \Delta t_{\text{slew}})/C_c. \qquad (5.4)$$

In this equation, N_0 is the TDC *offset*, Δt_{slew} is the time slewing of the PMT signal and C_c is the counts-to-time conversion constant (i.e. bin-size) of the TDC. The cosmic-ray muon trigger does not depend on the TDC (LeCroy 1875) reading itself, since the output from the discriminators is fed directly into a mean-timer which builds a signal proportional to the mean of both signal arrival times. This signal does not depend on the z-position of the hit, since the mean of both arrival times t_1 and t_2 of the pulse at the PMT's at either end of a counter is independent of z:

$$t_{\text{mean}} = \frac{T_{0_1} + T_{0_2}}{2} + \frac{L}{2C_{S_z}}. \qquad (5.5)$$

The time slewing, however, which is different for both PMT's at either end of a counter, *does* have an effect on the above mean-time. To account for this, we have to add the term

$$\Delta t_{\text{slew}} = \frac{\Delta t_{\text{slew}_1} + \Delta t_{\text{slew}_2}}{2} \qquad (5.6)$$

to Eq. (5.5). This means that the time of a trigger, and therefore the related time offset correction to be applied to the muon chamber hits, *does* depend on this time-slewing term.

In principle, the TDC (LeCroy 1875) readings can be used to obtain the z position of the muon impact point on the tile. For the BGO calibration data this is not possible, however, since the TDC readings were regularly in overflow. This was due to the electronics timing schedule being different from that for regular dimuon runs.

5.4 Muon-chamber reconstruction

The muon detector is a sampling detector. For an ionizing track passing through, it returns a number of geometrical coordinates which are either on, or close to the actual path followed by the particle. The coordinates are not returned directly but have to be determined from the time information delivered by the muon-chamber TDCs. The TDC readings are labeled according to the position of the sense wire in a chamber and octant. This information of TDC counts has to be converted into a drift time, which is defined as the time span needed by the electrons in the muon chamber gas to drift towards a sense wire. Once the drift time (or a first-order approximation of it) is known, the position from which the electrons emerged (the *hit position*) can be estimated by means of a *cell map*. This cell map determines the hit position according to a drift-path parameterization inside a P or Z-cell. This procedure is repeated for all the TDC readings in the data, thus providing us with a map of hits which constitute a sampled track path.

Normally, only part of these hits really belong to a muon track. A variable number of hits are caused by knock-on electrons (delta-rays), or malfunctioning of the readout electronics. It is the main task of the muon-chamber reconstruction to find out which hits belong to a real track and to get the best possible estimate for the position, angles and momentum of this track.

The reconstruction of a muon track consists of three consecutive parts.

❍ Reconstruction of hits into segments, and segments into tracks inside one muon chamber. This is done per projection plane (the xy-plane and the yz-plane) and is called the *pattern-recognition* phase (Sec. 5.4.1).
❍ Reconstruction of three-dimensional tracks inside a single octant from the projections. This is the *track-fit and refit* phase (Sec. 5.4.2).
❍ Reconstruction of single-octant tracks and segments into cross-octant tracks. This is the *track-matching and inter-octant matching* phase (Sec. 5.4.3).

The reconstruction algorithms use three different systems of coordinates: the global coordinate system, the local-octant coordinate system and the local P-cell coordinate system. The global system uses the detector vertex as origin and has orthonormal axes with the y-axis vertical and the z-axis along the beam pipe. The local-octant coordinate system has its y-axis perpendicular to the chamber plane and is further defined as to coincide with the global system in the *vertical* octant. The local P-cell system has its origin defined in the middle of a P chamber at the sense wire plane of the cell under consideration. It is used in the pattern-recognition phase only. Further, we define a "half-octant" as being an octant in a single Ferris wheel and a "double-octant" as two aligned octants, one from each Ferris wheel.

5.4.1 Pattern-recognition phase

The pattern-recognition task is to construct higher-level objects, i.e. segments, out of all the P and Z hits. To perform this task, an algorithm is used which assumes a certain

parameterization of a track. In the xy-plane one assumes a circular arc (i.e. a fixed radius of curvature). In the yz-plane one assumes part of a sine curve (Fig. 5.5). Any shape different from these will be not or badly recognized by the algorithm. This is a trade-off of every pattern-recognition algorithm and it does not impose any problems in our case. The charged particle, in this case a muon, enters a homogeneous magnetic field when
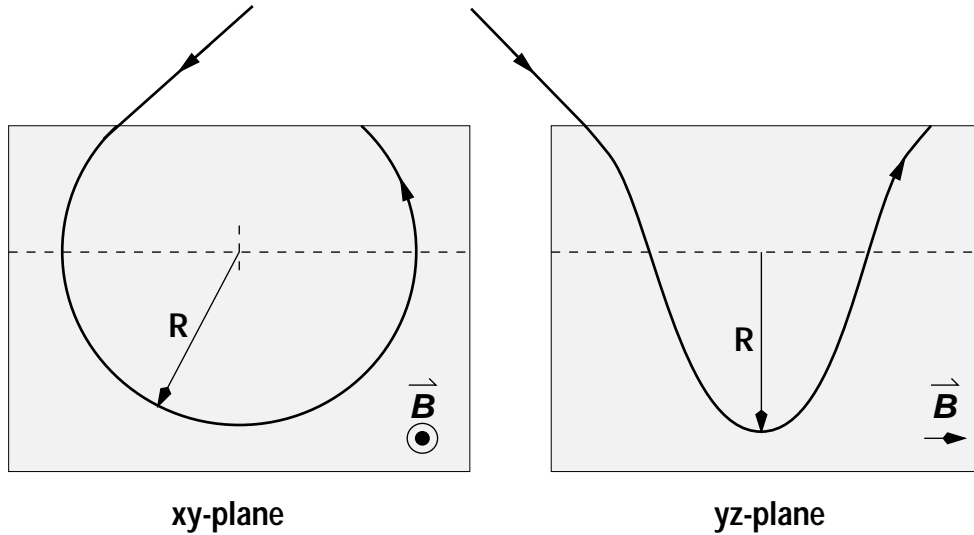

xy-plane   **yz-plane**

Fig. 5.5: The path followed by a charged particle entering a magnetic field is a helix which decomposes into a circular arc and a sinusoid when viewed in a plane perpendicular and parallel to the field respectively.

having passed the magnet yoke and coil from the outside. Inside this field, an almost helical path will be followed if no catastrophic energy losses are experienced. This helix, when viewed in a plane perpendicular or parallel to the magnetic field lines, decomposes into a circular arc and a sinusoid, respectively.

Usually, the radius of curvature of the track is at least an order of magnitude larger than the dimension of the magnetic field region. In that case, only a small part of the helix will be present in the field region. This has consequences for the shape of the track in the yz-plane. When viewed in a yz-plane where the track enters vertically into the magnetic field region, the sinusoid can be expanded in a Taylor series of which the first term is linear in the dimension along the axis of the helix. So, in a good approximation, the yz-track projection can be fitted by a straight line. For data like the BGO calibration data, all tracks pass near the center of the detector. The straight-line yz-track then is a good approximation of the real yz-track. This approximation is only used in the pattern recognition and fit/refit phase. In the final fit (swimfit), the angle of the track in the yz-plane is a parameter that is allowed to vary versus the cord distance along the track.

For general tracks, passing through three or more half-octants, the direction of the track can be almost parallel to the Z-chambers. No good track reconstruction in the yz-plane is possible then. One should keep in mind that the L3 muon chambers were designed for tracks emerging from the vertex, so that the reconstruction is optimal for this type of tracks.

The pattern recognition has to be able to recognize tracks over a large range of momentum, so also tracks with a radius of curvature comparable to the detector dimensions. For such low-energy tracks, any energy loss in the detector will change the radius of curvature

such that the overall track is no longer circular. The multiple scattering involved in the propagation of the particle through the muon detector and local variations in magnetic field strength will also alter the circular shape to non-circular, but these effects are only marginal. A larger effect is caused by the propagation of a track through the inner detector. Low-energy tracks will experience a relatively large energy loss. In this way, the track is split up into two nearly circular parts, each inside the muon chambers, and an intermediate part with varying curvature in the inner detector. To implement a general algorithm which works for all track topologies in the detector, the following scenario was chosen:

– Reconstruct tracks from P and Z-hits per half-octant.
– Reconstruct the trajectory to a certain common plane.
– Match tracks at these common planes to form a complete physical track across the detector.

The "common planes" are planes parallel to the z-axis, containing the vertex of the detector and crossing the xy-plane under a certain azimuthal angle. The azimuthal angle of the plane is chosen such that the track passes the plane nearly perpendicular.

P-chambers. The pattern recognition is performed per single P-chamber. All the hits present inside one complete chamber are examined in one go, so no division of the hits into smaller groups is made. The reason why all hits are examined at once is that we try to recognize general segments, thus segments under any possible angle. For instance, there can be segments which pass the wire planes almost perpendicular and which have a span almost as wide as the P chamber itself. These segments should be recognized as good as possible.

The algorithm used to perform the pattern recognition is a slight variation to the so-called *Hough transform* method [79]. For a set of N points (x_i, y_i), the muon chamber
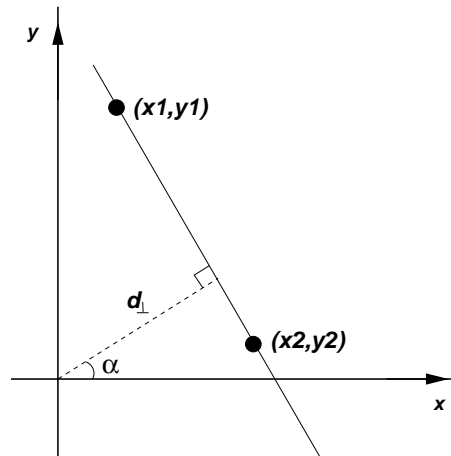
Fig. 5.6: Two points defining a perpendicular distance and an angle with respect to the origin.

hits, there are $\frac{1}{2}N(N-1)$ possible combinations of 2 hits out of the N. Each combination acquires an angle α and a distance $d_\perp$ from the origin perpendicular to the line connecting both points (Fig. 5.6). These two parameters describe the normal-form equation of a straight line through both hits:

$$(x_i - x_j)\cos\alpha + (y_i - y_j)\sin\alpha - d_\perp = 0. \tag{5.7}$$

For every combination of two hits, the angle α and perpendicular distance $d_\perp$ are

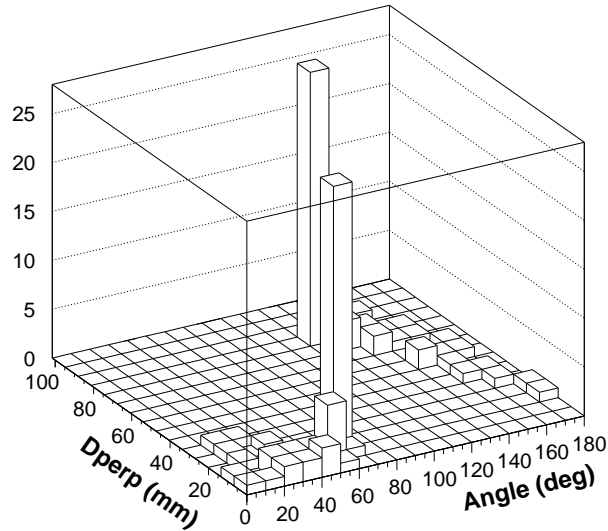Fig. 5.7: Example of the matrix M, showing two peaks at ordinates occupied by a P-segment and its ambiguity.

accumulated into a two-dimensional matrix $\mathsf{M}(\alpha, d_\perp)$ which is dimensioned such that the two parameters for every possible hit combination are within its range (Fig. 5.7). Note that $d_\perp$ has a sign corresponding to the sign of the y-intercept at $x = 0$. Using this sign, the angular range of M in α can be reduced to $[0, \pi]$ while different point combinations with the same angle α are still separated. If a pattern of the form (5.7) is present in the set of data points, the density of points in the matrix M will increase for the matrix elements containing the pattern's α and $d_\perp$. The bin width in α and $d_\perp$ determines the resolving power of the pattern recognition. A bin width larger than the typical separation of data points in the bin's parameter will obviously lead to a loss of accuracy and to inclusion of noise hits. Too small a bin width will lead to a loss of recognized patterns, unless no noise is present. If noise *is* present, the data points of interest can be more or less scattered. One then needs to take into account a minimum bin width due to this scattering.

With a large number N of hits present, the time spent for pattern recognition is proportional to N^2. To increase the efficiency of pattern recognition, the boundaries in the $d_\perp$ variable are set such that all hit combinations are only just included. Furthermore, a distance cut is introduced such that a hit combination is only taken into account if it satisfies

$$d_{\min} < d < d_{\max}, \tag{5.8}$$

where d is the distance between the hits in the xy-plane. The distances $d_{\min}$ and $d_{\max}$ are set to 3.0 mm and 100.0 mm, respectively. The lower cut rejects the combinations of hits which are close to each other, which are likely to contain at least one noise hit. The upper cut prohibits hit combinations being used from 2 hits separated by a large distance, which is not efficient.
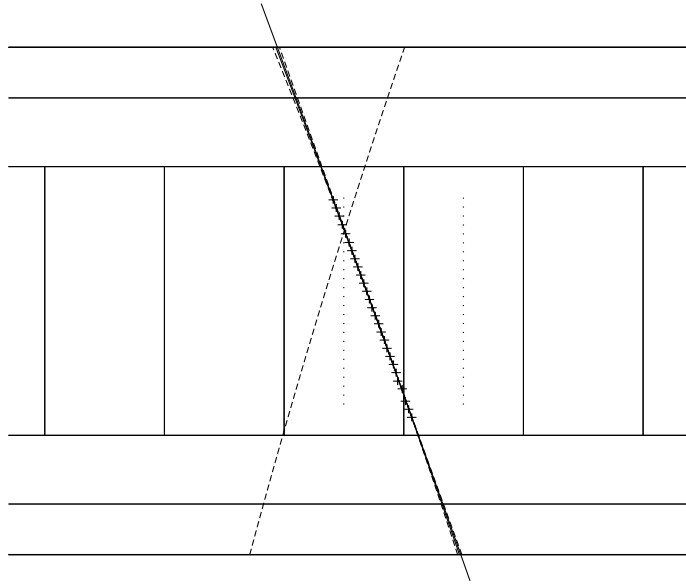
Fig. 5.8: View of P-cells, showing a segment, its ambiguity and the track crossing the sense wire plane.

The maximum number of P-segments allowed per single P-cell is fixed to 15. Usually, there will be only 1 P-segment per cell. The full cell width is divided into 15 bins of about 7 mm in $d_\perp$ and 18 bins of $10°$ in α. With these bin sizes, it is evident that some noise will always be picked up and that segments with a large curvature will only partially be recognized. For this reason, the above pattern-recognition phase is followed by so-called *pick and drop* phases.

For a bin of the matrix M to become a potential segment, it must contain at least 6 hits. The bins satisfying this cut, are sorted in the order of largest number of hit combinations. Since storage space is limited, the hit combinations of the best segment candidates are stored first such that only worse candidates could eventually not be stored.

The pick and drop phases use the hit combinations as found from the matrix M and apply a circular fit to them [80; 81]. In the pick phase the hits used up to then are fitted by a circle. Then, for every hit the perpendicular distance to the circle is calculated. If this distance is smaller then 4.0 mm, the hit is included in a new circle fit. In the drop phase, the hit is excluded from the new circle fit if it has a perpendicular distance larger then 3.0 mm. In practice, first a drop phase is applied after which two pick phases and a subsequent drop phase are applied. The resulting hits define a so-called Muon P Segment (MPSG).

Since the only information we have at this stage is which *wires* were hit at certain times, every P segment is accompanied by its ambiguous P segment, which is the mirror image of the original segment on the sense wire plane, see Fig. 5.8.

Z-chambers. All information we have in case of the Z-chambers is the wire which has been hit. Most ambiguities are, however, resolved by the fact that the Z layers are shifted with respect to one another by one half cell. The pattern recognition for the Z-chambers is performed per double-octant. Each octant contains 8 layers of Z-cells, 4 layers for the MI chamber and 4 layers for the MO chamber (Fig. 5.9). The pattern recognition is very basic in this case, it consists of a straight-line fit to any number (≥ 3) of hits. If the RMS residual of the fit is below a threshold of 10.0 mm, the hits in the fit are said to constitute a Z-segment. This brute-force method is necessary here, because the matrix method cannot be used due to the dimensions of the double-octant compared to the resolution that the

matrix M should have. The matrix simply would become very big, with only a few entries filled. The small number of hits on a recognized Z-track (≤ 8) would also make this method sensitive to noise.

Depending on the distribution of the hits over the 8 Z-layers, hits from different layers are combined into a fit. If 3 or 4 layers in both the MI and MO chamber are hit, each chamber is fitted individually. If less than 3 layers are hit in both chambers, the hits from both chambers are combined into a single fit. Any segments found inside one chamber
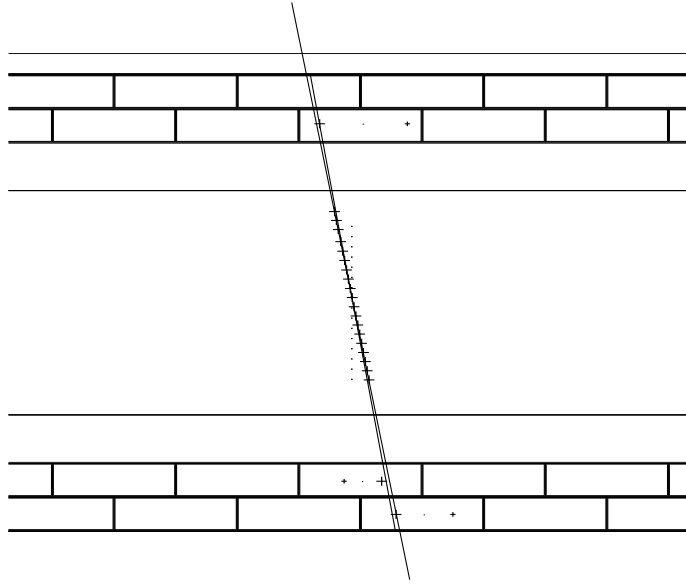

Fig. 5.9: View of Z-cells, showing a segment and the track crossing the 4 Z-layers of the chamber.

are stored as a Muon Z Segment (MZSG). If the pattern recognition is performed per two chambers at once, the segments are stored as the hit combinations inside one chamber. The combination of two Z-segments (or one Z-segment if no more hits are present) is stored as a Muon Z Track (MZTK). A MZTK track represents the full yz-track in an octant.

5.4.2 Track-fit and refit phase

Segment matching. Once the P- and Z-segments have been found, one can start to look for three-dimensional tracks. For this, we loop over all Z-tracks in order to match information from the P-segments and create three-dimensional tracks. In the pattern-recognition phase, the P segments are corrected for time of flight and time of propagation according to the mean z position of all Z segments in the octant. For every Z track the possible P segments are re-fitted using the z-ordinate of the Z track. Depending on the actual z position of the P segment, the quality of the P segment is reflected in the alignment of its hits and thus in the χ^2 of the segment fit. A high quality P segment, displaying a small fit-χ^2, thus is likely to have had the correct z position used. If the fit result is good enough, the P segment is associated with the Z track. Since a single P segment does not have a well determined momentum, the number of P segments associated with a certain Z track are required to be 2 or 3. This makes up a so-called *doublet* or *triplet* track, respectively. If a matching set of P segments and a Z track is found, the compounds are stored as a Muon Track (MUTK).

Track ambiguity resolvement. Once we have found three-dimensional tracks, usually there will be tracks which contain the same Z track and/or a number of the same P segments. These tracks are defined ambiguous with respect to each other. Tracks ambiguous to each other can be put in a ambiguity group. The problem now is to find the best track from all tracks in a certain ambiguity group. The criterium "best" is defined according to the parameter

$$Q = 10^6 * (100 * \mathrm{P} + \mathrm{Z}) + (1000.0 - \chi^2/\mathrm{DoF}), \qquad (5.9)$$

where P and Z denote the number of P and Z segments in a track, and χ^2/DoF is the chi-squared over degrees of freedom of the last circle fit applied to the constituent P segments of the track. This criterium may seem rather arbitrary, but tests show that the "real" track usually is composed of a triplet P segment combination. If any track ambiguities are left after the segment criterium has been applied, we choose that track which has the best circle fit. Whereas this is a *quality* selection of the tracks, we also select tracks on their *charge*. The best track with positive and the best track with negative charge are stored for further processing.

Scintillator track-intercept. For the BGO calibration runs, the time correction to be applied to the MUTK track depends on the scintillator barrel intercept. Once the track has been (roughly) reconstructed, the intercept with the scintillator barrel can be computed. One should note that only the *intercept* of the track with the barrel is computed. The presence or absence of a *real* hit near the intercept is not of influence on the intercept coordinates.

Refit phase. As described above, the MUTK track objects are obtained from a simple circular fit to the hits which make up the segments of the track. The hits were only corrected for their positions due to the time of flight and time of propagation delays. To obtain a precise measurement of the track, more corrections to the hits have to be applied. In sequential order these are:

❍ Corrections for updated time of flight (ToF) and time of propagation (ToP) delays.
❍ Corrections for the alignment of the muon chambers and for the wire sag.
❍ Corrections for the track curvature versus the segment curvature (3σ cut).

The corrections to be applied all influence the so-called *master point* of the P and Z segments. The master point can best be described as the center of gravity of the P or Z hits of a segment. In principle any point on the segment can be used as a master point. The importance of the master point lies in the fact that the final fit to the muon track (swimfit) only uses the position and directional information of the master point. Thus, the master point represents its *whole* segment. After the pattern-recognition phase, a first estimate of the master point is obtained by the circle fit of the P-segments, where the y-position of the master point is put at the middle y-ordinate of the chamber. During later refit stages the master point is corrected. This correction takes into account the fact that the actual track position is measured more accurately by the complete track fit than by the P-segment fit itself. By shifting the master point after each refit such that it lies on the circle fit, the best estimate of the master point is obtained with least chance of any systematic error in its position. The variables contained in the master point, the three coordinates x, y and z and an angle in the xy-plane, serve as reference coordinates for the final *swimfit* (see below).

ToF and ToP corrections. The corrections on the muon-chamber TDC times are calculated once after the three-dimensional tracks have been found. The scintillator-track intercept has to be known beforehand. The position of the intercept used here corresponds

to the position (i.e. tile) of a real hit if and only if the real hit does not lie further away from the track intercept than 2 tiles. If the difference is larger than two tiles, the track intercept is used as the lower scintillator intercept. In the latter case, the time slewing factor is approximated by its mean value, 1.8 ns. In the BGO calibration data, the stop time for
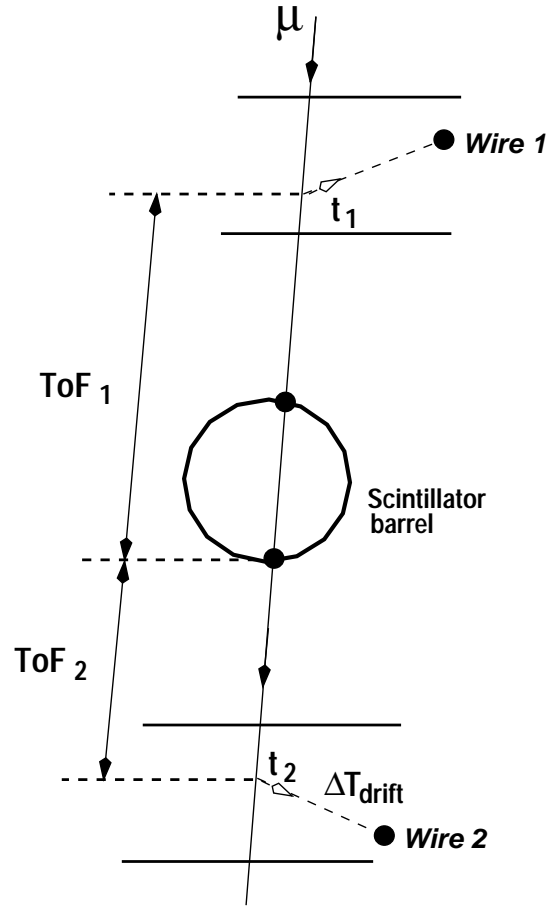

Fig. 5.10: Track passing through two muon chambers and the scintillator barrel, see text.

the muon chamber TDCs is (up to a constant term) equal to the time of the scintillator barrel coincidence signal. The start time of the TDCs is given by the time a signal from a wire being hit reaches the TDC. Assuming that muons always enter such that the upper scintillator tiles are hit earlier than the lower scintillator tiles (thus examining downward muons only), the muon-chamber TDC start and stop times equal (Fig. 5.10)

$$t_{\text{stop}} = t_1 + ToF_1 + \Delta t_{\text{slew}} + C_{\text{SCB}},$$
$$t_{\text{start}} = t_1 + ToP_1 + \Delta t_{\text{drift}} + C_{\text{MUCH}}.$$

The terms C_{SCB} and C_{MUCH} are constants, where the first depends on the actual scintillator tile which gave the trigger and the second depends on the muon chamber octant. The term ToP_1 is the Time of Propagation the signal needs to pass the muon chamber P-wire. The time measured by the TDC equals the difference between t_{start} and t_{stop}:

$$\Delta t_{\text{TDC}} = t_{\text{start}} - t_{\text{stop}} = ToP_1 - ToF_1 - \Delta t_{\text{slew}} + \Delta t_{\text{drift}} + C_{\text{MUCH}} - C_{\text{SCB}}.$$

(5.10)

To find the drift time, the time Δt_{TDC} as given by the TDC must be corrected by Δt_{corr}

$$\Delta t_{\text{drift}} = \Delta t_{\text{TDC}} - \Delta t_{\text{corr}}.$$

(5.11)

Since

$$t_1 + ToF_1 = t_2 - ToF_2,$$

(5.12)

the correction to be applied to the drift time for hits in the upper and lower octants, respectively, equals

$$\Delta t_{\text{corr}_1} = ToP_1 - ToF_1 - \Delta t_{\text{slew}} + C_{\text{MUCH}} - C_{\text{SCB}},$$

(5.13)

$$\Delta t_{\text{corr}_2} = ToP_2 + ToF_2 - \Delta t_{\text{slew}} + C_{\text{MUCH}} - C_{\text{SCB}}.$$

(5.14)

The constants C_{MUCH} and C_{SCB} have to be calibrated versus the muon octant and the scintillator tile which was intercepted (i.e. the lower scintillator barrel hit). Since they are not independent of each other, the correction procedure is iterative. For calibrating these constants (which just alter the muon chamber T0 offsets), segments crossing the sense plane are used (App. A).

Alignment corrections. The muon-chamber octants all suffer from material stress, as well as temperature and pressure variations. Therefore, the alignment of the chambers must be continuously corrected. The track reconstruction assumes a perfect detector in the sense that positions and alignments are absolute and stable. However, the *real* position of a wire differs from its ideal position. All the P-chamber hits on a track are corrected for this effect. The correction factors are calculated using alignment information from the muon chamber data base. Besides the alignment, the P-chamber wires themselves are also regarded as perfect, i.e. they are assumed to be perfectly straight. In reality, the wires sag due to gravity according to a catenary. The hits are corrected for this wire-sag. The tension of the wires is assumed constant. Having applied these alignment and wire-sag corrections, the P segments are refit.

Curvature corrections and 3 σ cut. After the alignment and wire-sag corrections have been applied, an ideal segment would be coincident with the trajectory of the muon through the muon chambers. The segments are not ideal however. Since the span of a P segment is only about 30 cm the precision of the segment fit is much worse than the precision of the track fit, over a length of about 3 meters. This means that the curvature obtained from the segment fit can be quite different from the track curvature. To obtain a precise measurement of the master point of a segment, we drop hits from the segment that are further off than 3σ from the segment fit. For this, the segment should be fit such that noise hits are of minor influence to the fit results. For ideal segments, we can "subtract" the track curvature from the segment (Fig. 5.11). The segment will then be straight and can be fit by a straight line. Using this straight-line fit, we can safely drop hits using the 3σ limit. In practice, the curvature-corrected hits are fit by *absolute deviations* rather than by a least-squares fit. This is a method to obtain a fit that is not sensitive to noise hits. After the 3σ cut is applied, the segments are exposed to a circular refit after which the segment master points are re-determined.

Particle trajectory
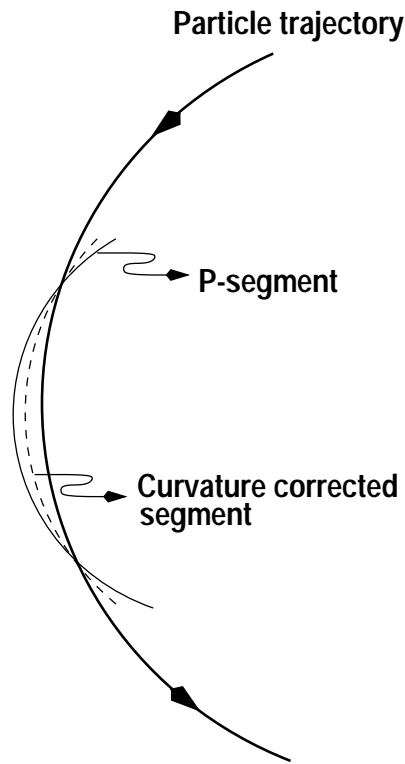
→ **P-segment**

→ **Curvature corrected segment**

Fig. 5.11: Track-curvature correction. The track curvature is subtracted from the segment curvature which gives the dashed segment.

Swimfit. Up to now, in all segment and track fits we assumed that the trajectory of the muon was perfectly circular. In practice, the trajectory is only locally circular since scattering and magnetic-field variations change the curvature of the muon path. These variations should be taken into account if one wants to estimate the particle direction, position and momentum. Since the scattering is a stochastic process, one can only try to reconstruct the *mean* trajectory of the muon. Knock-on electrons, for example, are not taken into account. The segment master points play an important role in the reconstruction of the trajectory. They serve as reference points to which the global trajectory is fitted. Starting from one of the outer master points on the track, the mean trajectory is being *swam* to the other outer master point. The term "swam" is used because local field strengths are taken into account, as well as scattering by the muon-chamber material. The agreement of the swam position is checked against the position of the near master point. The difference between the swam position and the real position determines how the track parameters at the start of the swimming procedure will be changed. This procedure is repeated 6 times at maximum, after which the adapted starting points of the swim procedure are stored. For a review about the mathematical background of the swimfit we refer to [82].

If the final χ^2 of the swimfit is below a certain value, the track is accepted, otherwise it is rejected. The χ^2 distribution peaks at zero since the number of degrees of freedom of the swimfit is zero. The latter is due to the fact that the swimfit *forces* a track to pass through a predefined set of coordinates.

5.4.3 Track matching

After the tracks have been fitted inside the muon chambers by the swimfit, we need to match those parts of a track that belong to one and the same muon. In the BGO calibration runs, the tracks almost always pass through the inner detector. We have, therefore, chosen to track the muon trajectory back to a plane parallel to the z-axis and across the vertex (called hereafter a *vertex plane*). Such a plane can only take certain azimuthal orientations and is chosen such that it is as perpendicular as possible to the track direction. The backtracking is done with the help of the GEANE package [82]. The mean particle trajectory is being reconstructed. The coordinates are stored at 15 points along the trajectory.

Once all tracks have been backtracked towards a vertex plane we calculate the *correlation coefficient (Pearsons r)* for two tracks from different octants. The correlation coefficient is defined in terms of the coordinates along the trajectory as

$$r = |r_x r_y r_z|, \tag{5.15}$$

where r_x is defined as

$$r_x = \frac{\sum_i (x_i^1 - \bar{x}^1)(x_i^2 - \bar{x}^2)}{\sqrt{\sum_i (x_i^1 - \bar{x}^1)^2 \sum_i (x_i^2 - \bar{x}^2)^2}}, \tag{5.16}$$

where the superscripts correspond to the two track pieces. Similar equations hold for r_y and r_z. If two track pieces are part of one and the same muon track, we expect that their coordinates are highly correlated. The track-pairs having the largest correlation coefficient, for like-sign and unlike-sign charged tracks, are memorized. The track pair with unlike-sign charged tracks is compared to a possible track pair with like-sign charged tracks. If the like-sign charged track pair has a larger correlation coefficient than the unlike-sign charged track pair, and the value of its correlation coefficient exceeds 0.75, the like-sign charged track pair is chosen, otherwise the unlike-sign charged track pair is chosen. The chosen track pair is stored if the correlation coefficient exceeds the value of 0.4. If a track pair fails this cut, it is rejected by the reconstruction.

This matching procedure turns out to work well. In order to calculate the efficiency of the track matching, we select events with one upper and one lower track part. For both track parts the standard quality cuts are applied (except for the cut on Pearsons r). The efficiency is now defined as

$$\epsilon = \frac{N_1}{N_1 + N_2}, \tag{5.17}$$

where N_1 and N_2 are the number of selected events with one and two (LEP3-) backtracked tracks, respectively. The matching efficiency is shown in Fig. 5.12, versus the zenith and azimuth angle and versus surface momentum. For momenta below about 50 GeV/c, the matching efficiency drops relative to the value at higher momenta. This is caused by the fact that for low momenta, the correlation coefficient is less well defined than for higher momenta, due to the bending of the tracks in the magnetic field. The dip for small zenith angles is caused by the access shaft, since in this region we have a large flux of low momentum muons. The dips in the azimuth distribution are caused by the fact that the matching efficiency for two tracks from different Ferris wheels is low. Tracks are not corrected for the alignment difference between both Ferris wheels. Thus, two tracks from different Ferris wheels will in general be misaligned, causing the correlation coefficient to decrease.
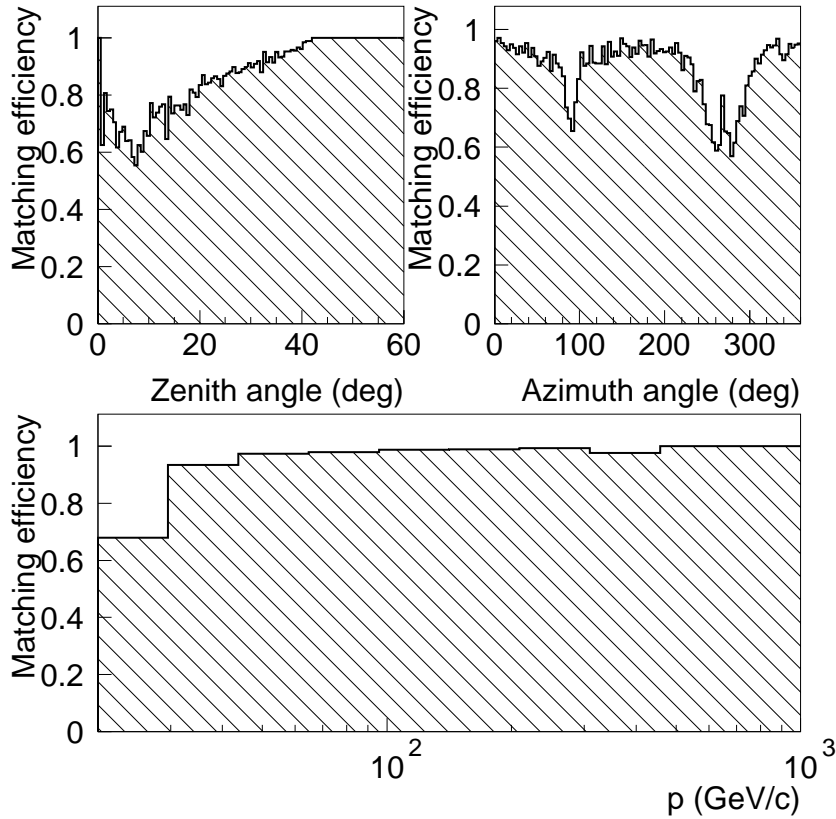
Fig. 5.12: Track matching efficiency for cosmic-ray muons versus zenith angle, azimuth angle and surface momentum.

In case dimuon data are being reconstructed, the difference of the coordinate intercepts at the vertex plane is used instead of the correlation coefficient, to select the two best matching tracks. This proves to be a safer method than the correlation method since the dimuon tracks are *confined* to the vertex.

5.4.4 Backtracking towards LEP3 and surface

From the track-matching procedure we now have found muon tracks which passed through the molasse and through the L3 magnet. In order to reconstruct the tracks on the surface they have to be backtracked through the magnet and through the molasse. The backtracking is again done using GEANE. The starting point of the backtracking is chosen as the uppermost master point of a track. Tracks are first backtracked through the magnet to the LEP3 volume which just encloses the magnet. This tracking endpoint is stored and is used as the starting point for the back tracking towards the surface. The accuracy of the latter backtracking depends mainly on the accuracy with which the halls and shafts are simulated. The backtracking is considered successful only if the track reaches the surface disk within its radius of 77.6 m. In about 2% of the data and 0.2% of the Monte Carlo the surface backtracking fails due to this reason.
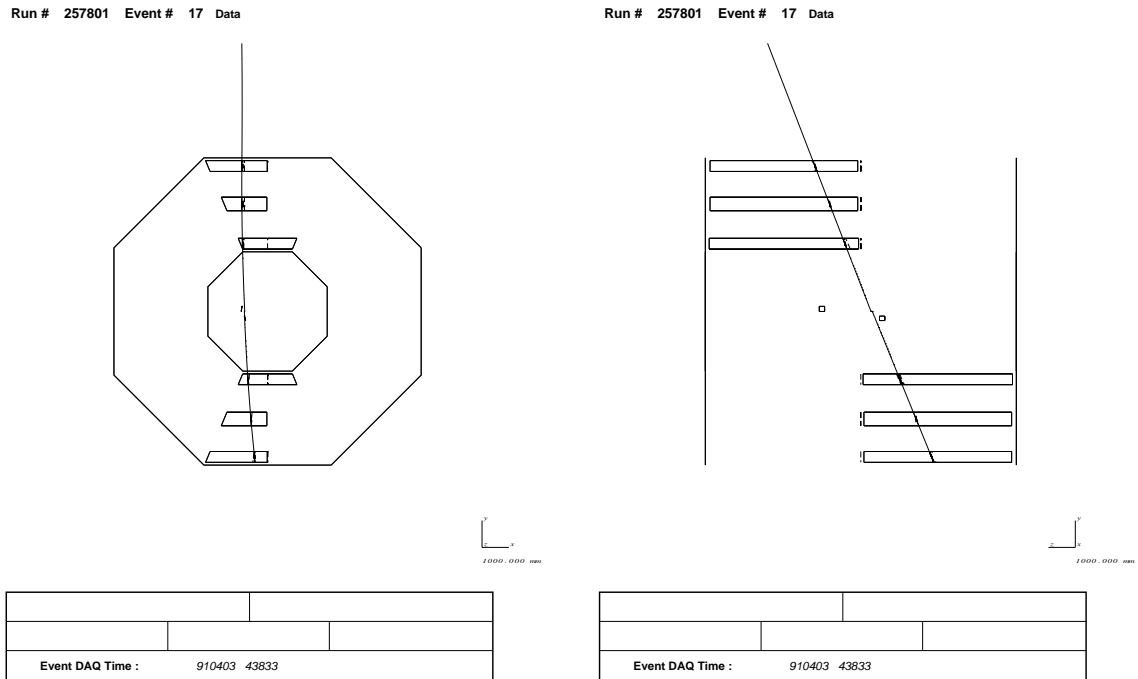
Run #   257801   Event #   17   Data

1000.000 mm

1000.000 mm

Event DAQ Time :	*910403 43833*	

Event DAQ Time :	*910403 43833*	

Fig. 5.13: The front and side view of a cosmic-ray muon event.

L3C Interactive Interface V1.0

File   Motion/Proj   Info   Options   Edit   Utils   Help

*** L3C Interactive Interface V1.0 ***

User: col3
Program: REGE
Steering: INL3C V2.11/01 981002 18:45 Interact
Input: /user/albert/BGOcal_data/KV5022.65.sl
Output: None

Serial #   2
Run #   257801
Event #   17

DAQ Date 910403 Time   43833

Event contains:

        2 MUTK tracks
        1 LEP3 tracks
        1 SURF tracks
        2 SCNT hits
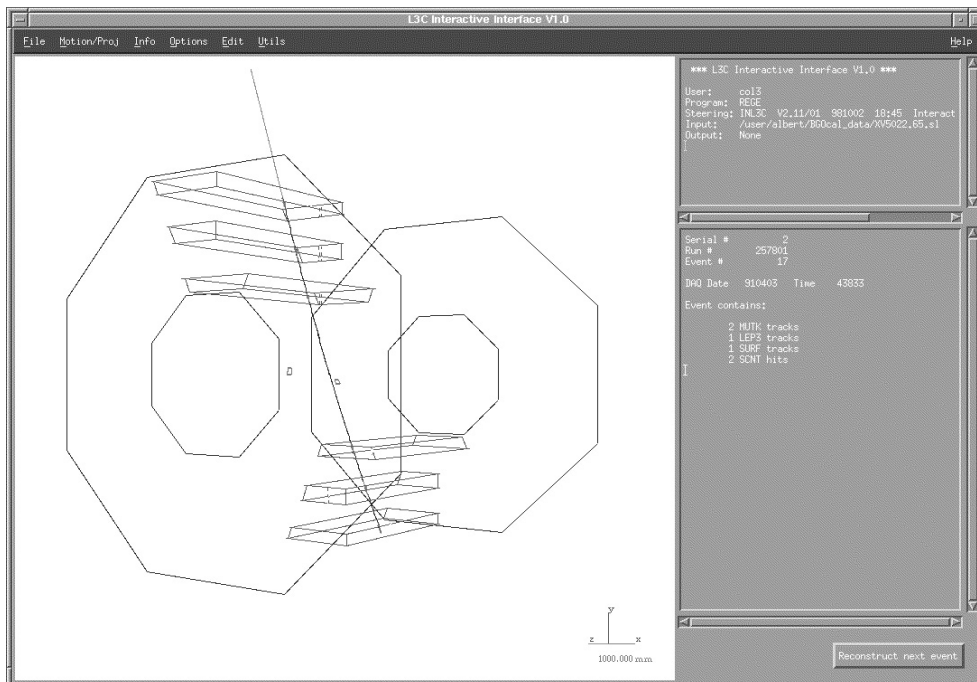
1000.000 mm

Reconstruct next event

Fig. 5.14: The graphical interface to the reconstruction and simulation software showing a cosmic-ray muon event.

5.5 Visualization

To visualize the reconstructed muon track and its P- and Z-chamber hits, the event and the detector, including the hall and shafts, are represented by graphical objects. In a graphics interface, these objects can be examined from every angle. In addition, information on the graphical objects can be retrieved. This is a very useful tool for debugging the reconstruction and simulation software and for obtaining insight into an event. In Fig. 5.13 and 5.14 the front and side view of a cosmic-ray muon event and the graphical interface displaying the same event is shown.

Monte Carlo simulation

For a complex experimental setup as the L3 detector, it is necessary to know the exact response of the detector to any event configuration. Also, the geometry of the detector and its immediate surroundings have to be simulated. The physics processes that the particles experience, as energy loss and interactions with matter, have to be taken into account. In this chapter, the different types of acceptances and efficiencies being used are presented. The setup used to simulate cosmic-ray muon events is explained and tested in a toy model. Some characteristics of the generator are shown. Finally, the method to obtain the effective geometrical acceptance is explained.

6.1 Cosmic-ray muon event simulation

Simulating cosmic-ray muon events in the L3 detector immediately implies that the particles should enter the detector volume from the outside. This is contrary to the usual situation in colliding beam experiments, where an event is generated at the center of the detector. This difference results in a Monte-Carlo setup that is different from the usual beam experiment Monte-Carlo generators. The simulation and subsequent reconstruction of cosmic muons consists of three parts (Fig. 6.1):

❍ Generation of the cosmic-ray muon vertex at a surface layer and forward tracking through the molasse and through the L3 detector.
❍ Reconstruction of the cosmic-ray muon inside the L3 detector.
❍ Back tracking of the cosmic-ray muon from the L3 detector towards the surface layer.

6.2 Acceptances and efficiencies

The Monte Carlo provides us with estimates on the various acceptances and efficiencies. These consist of

❍ The *geometrical acceptance* of an ideal detector, expressed in $[cm^2 sr]$. The molasse is not included here, neither is any efficiency. This number is determined by the geometry of the sensitive detector, for a fixed type of muon flux (in our case homogeneous). In
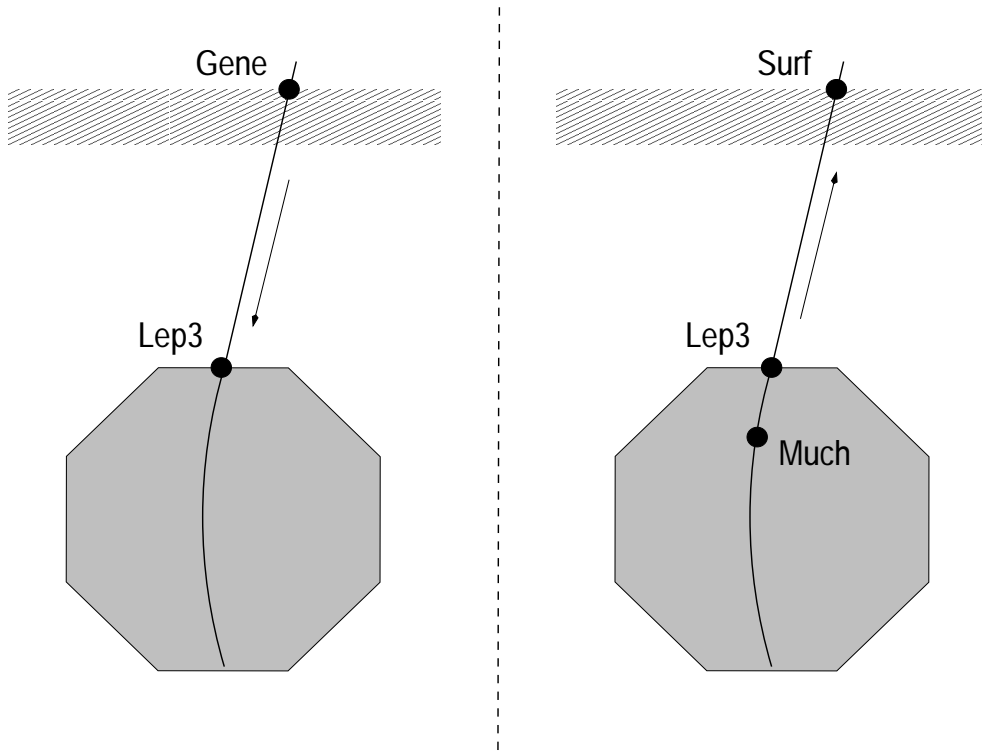
Fig. 6.1: The simulation and reconstruction phase during cosmic-ray muon simulation. Shown are the stages at which event information is recorded.

this work, the geometrical acceptance is mainly determined by the scintillator barrel volume since this volume gives the trigger for an event. We can also define the *relative geometrical acceptance* which is determined by the ratio of tracks passing the sensitive part of the detector over the total number of tracks generated. This just equals the geometrical acceptance divided by the total phase space $\Sigma\Omega$, Eq. (6.8).

○ The *molasse relative acceptance*. This number reflects the ratio of the number of muons passing through the molasse over the total number of generated muons at the surface. It depends on the angles, position and momentum of a muon, since the amount of molasse seen by the muon is determined by the geometry of the halls and shafts. When neglecting the variation of this acceptance versus position (on the surface layer), this will only depend on the muon momentum. In Fig. 6.2, the relative acceptance is shown for muon tracks passing through the molasse from the surface to the LEP3 volume. The surface energy of the tracks varies between the generator limits of 18.8 GeV and 1 TeV and is distributed according to a power law, Eq. (6.12). The relative acceptance is close to unity for small zenith angles since the momentum loss then is less than 18.8 GeV/c and almost all tracks make it to the detector. In Fig. 6.3 the momentum loss in the molasse versus zenith and azimuth angle is shown for tracks in the same momentum range. In Fig. 6.4 the energy loss rate of a muon passing through molasse is shown versus muon energy.
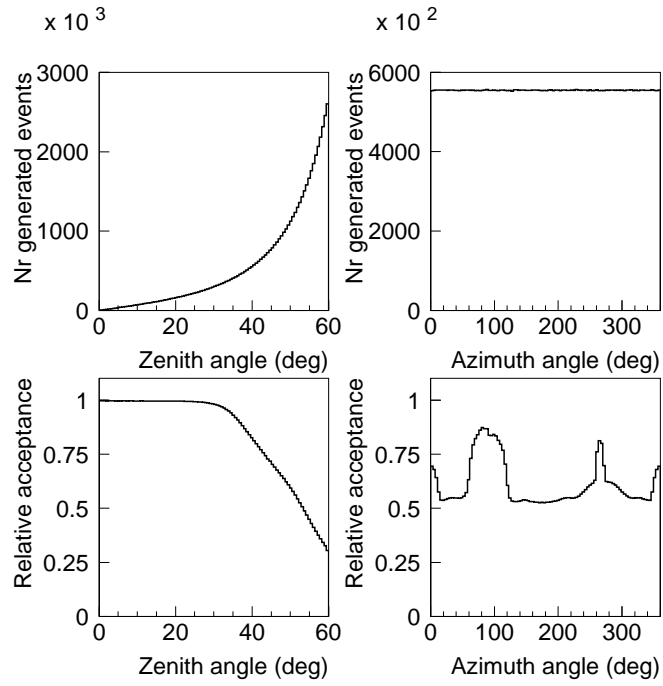
Fig. 6.2: The molasse relative acceptance versus zenith and azimuth angle together with the distribution of events versus both angles. Both distributions are integrated over the companion angle and momentum.
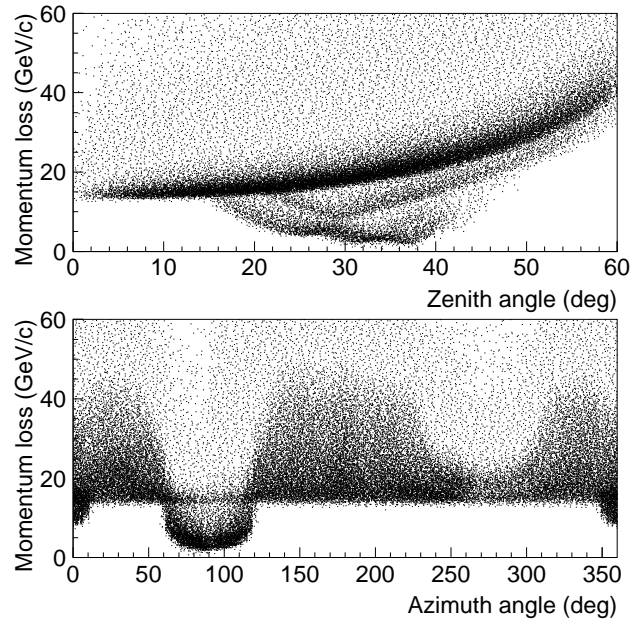

Fig. 6.3: Momentum loss versus zenith and azimuth angle for selected events. Both distributions are integrated over the companion angle and momentum.
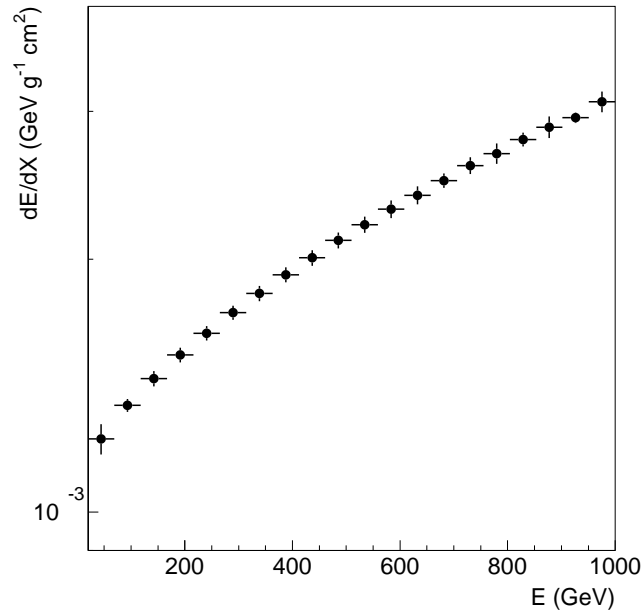
Fig. 6.4: Energy loss rate of a muon in molasse versus energy.

❍ The *real-detector efficiency*. This number is determined by the efficiency with which muon tracks are detected when they pass through the sensitive volume of the detector. It is in general time dependent. For instance, high-voltage problems in the muon chambers will decrease the efficiency. This high-voltage status is logged to a file on a regular basis. During the Monte-Carlo simulation phase, a specific entry of this file is read and the corresponding status of the wires is being simulated. The scintillator-barrel efficiency depends, among others, on the high voltage applied to the photomultiplier tubes. Since the scintillator-barrel detector is relatively stable, no separate logs are kept for its functionality. The efficiency is determined in an offline analysis using (di)muon events [70] originating from LEP collisions.

❍ The *reconstruction efficiency*. This number is determined by the ability of the reconstruction software to reconstruct (part of) a muon track in the detector, when there is enough information present to do so in principle.

The only efficiency which we obtain from the *data* is the *event selection efficiency*. This number describes the efficiency with which events are selected from a sample, by applying cuts to the data in order to simulate the (software) event trigger and to select events on quality. Also regions in data where problems occur that can not easily be corrected for, can be rejected.

The Monte Carlo used in this work is a real-detector Monte Carlo that includes the molasse layer. The result obtained from it is the product of all four acceptances and efficiencies as described in the list, and can be regarded as an *effective* geometrical acceptance.

6.3 Monte Carlo generators and geometrical acceptance

The Monte-Carlo generator should perform the steps as shown in Fig. 6.1. The simulation starts from the surface above the L3 site and tracks muons down through the molasse and the L3 detector. The reconstruction then has to track the muons back towards the surface. One such cycle allows for simulation and reconstruction of an event.

The purpose of the Monte Carlo is to obtain an estimate of the effective geometrical acceptance versus energy, location and angles of the generated muons. The geometrical acceptance is expressed in $[cm^2 sr]$ and denotes the effective phase space as seen by the detector. In order to obtain an estimate of the effective acceptance, we would like the setup of the generator to be as simple as possible. In this way we avoid any problems due to complications in the calculation. The second reason is that for simple generator setups the acceptance can be calculated analytically as well, which gives a firm foundation to the generator's validity, see App. C. The geometrical acceptance can be described by

$$\mathcal{A} = \int \cdots \int_{phasespace} \mathrm{d}^4\mathcal{P} \ \chi(\mathcal{P}) \ w(\mathcal{P}), \tag{6.1}$$

where the integral is performed over phase space $\mathrm{d}^4\mathcal{P}$ and $\chi(\mathcal{P})$ denotes the chance that a particular configuration in phase space is accepted or not. The factor $w(\mathcal{P})$ is the normalized weight assigned to an event, which generally depends on the phase space variables. This is needed to correct the sampling density of phase space, making it constant over all phase space.

6.3.1 Toy model generators

We start with the construction of a three-dimensional toy Monte-Carlo generator. For this toy Monte Carlo, we also obtain the acceptance by an analytical calculation. Our generator setup consists of a disk and a small sphere, separated by a distance h. The radius of the disk is D and the radius of the sphere is R (Fig. 6.5). The sphere is centered below the middle of the disk. Tracks are generated on the disk homogeneously distributed over the surface. An event is accepted if a straight track passes through the sphere. The acceptance can be written as

$$\mathcal{A} = \int_{\mathrm{disk}} \int \mathrm{d}S \ \boldsymbol{F} \cdot \hat{n} \ w(\theta), \tag{6.2}$$

where $\mathrm{d}S$ is an infinitesimal surface element of the sphere, $\boldsymbol{F}$ is the vectorfield *per unit source strength* describing the physical flux of particles, $\hat{n}$ is a unit vector on the surface of the sphere, pointing outwards, and $w(\theta)$ is the normalized event weight which depends on the zenith angle θ only, for this generator. For the type of generator used here, the normalized event weight equals (App. B):

$$w(\theta) = \cos\theta. \tag{6.3}$$

The Monte Carlo generator can be coded easily. One "shoots" tracks from a point on the disk towards the sphere and calculates the distance of closest approach (DCA) with respect to its center. An event is accepted if the DCA is less than or equal to the radius of the sphere. In order to keep the error on the Monte Carlo acceptance low, the efficiency of the generator should be close to 1.0. Thus, a large fraction of the tracks generated should cross the detector volume. This can be accomplished by fixing the opening angle
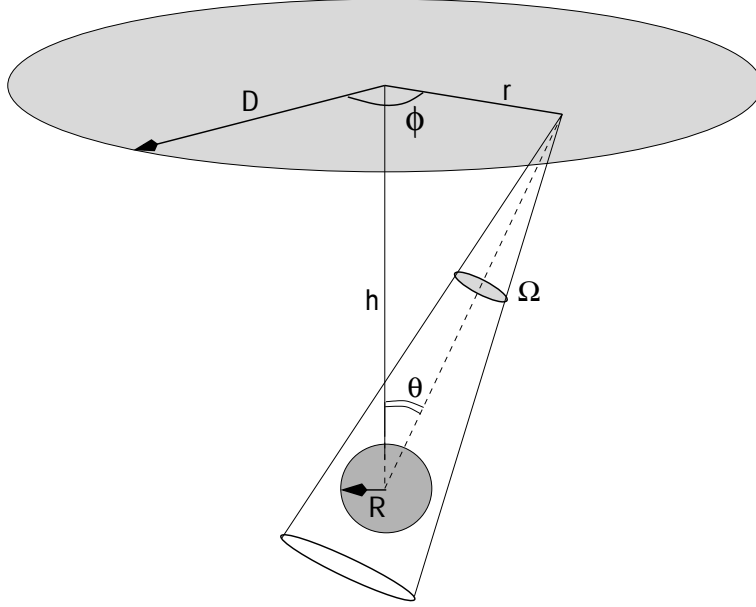
Fig. 6.5: Three dimensional toy Monte-Carlo setup.

of the cone to the value for vertical incidence where it just encloses the detector volume. The axis of the cone always crosses the center of the detector, for any value of r. The acceptance can be calculated analytically in a good approximation, see App. C.

In order to test the full cycle of generation and reconstruction, a second Monte Carlo generator has been constructed which simulates the real data. The aim is to reconstruct the generated angular distribution by means of the acceptance returned by the first Monte Carlo generator. To simulate the data, we use again a disk of radius D situated at a height h above the spherical detector with radius R. Points are generated homogeneously distributed over the surface of the disk. The disk is then tilted over angles θ and ϕ. The distribution in ϕ is uniform whereas the distribution in θ is chosen according to

$$u = 1 - (r1 + r2)/4, \tag{6.4}$$
$$\theta = \arccos u, \tag{6.5}$$

where $r1$ and $r2$ are uniform random numbers varying from 0 to 1. We have chosen 25 equidistant bins in $\cos\theta$ and one bin in azimuth. The generated flux per bin in $\cos\theta$ equals

$$F_{\text{gene}}^i = \frac{N_{\text{bin}} N_{\text{gene}}^i}{\mathcal{P} N_{\text{gene}}}, \tag{6.6}$$

where N_{gene}^i is the number of events generated in bin i, $\mathcal{P}$ is the phase space over which events are generated (which equals $\pi D^2 \, 2\pi(1 - \cos\theta_{\max})$ with $\theta_{\max}$ the maximum zenith angle of an event), N_{gene} is the total number of events generated and N_{bin} is the number of equidistant bins in $\cos\theta$. The reconstructed flux per bin in $\cos\theta$ equals

$$F_{\text{reco}}^i = \frac{N_{\text{acc}}^i}{\mathcal{A}^i N_{\text{gene}}}, \tag{6.7}$$

where N_{acc}^i is the number of accepted events in bin i and $\mathcal{A}^i$ is the acceptance for bin i. The generated and reconstructed distributions are shown to be in agreement (Fig. 6.6).

The total number of events generated was 10^7. The maximum zenith angle was $60°$, the radius of the sphere was chosen as 2 m, located at a depth of 45 m under the surface.
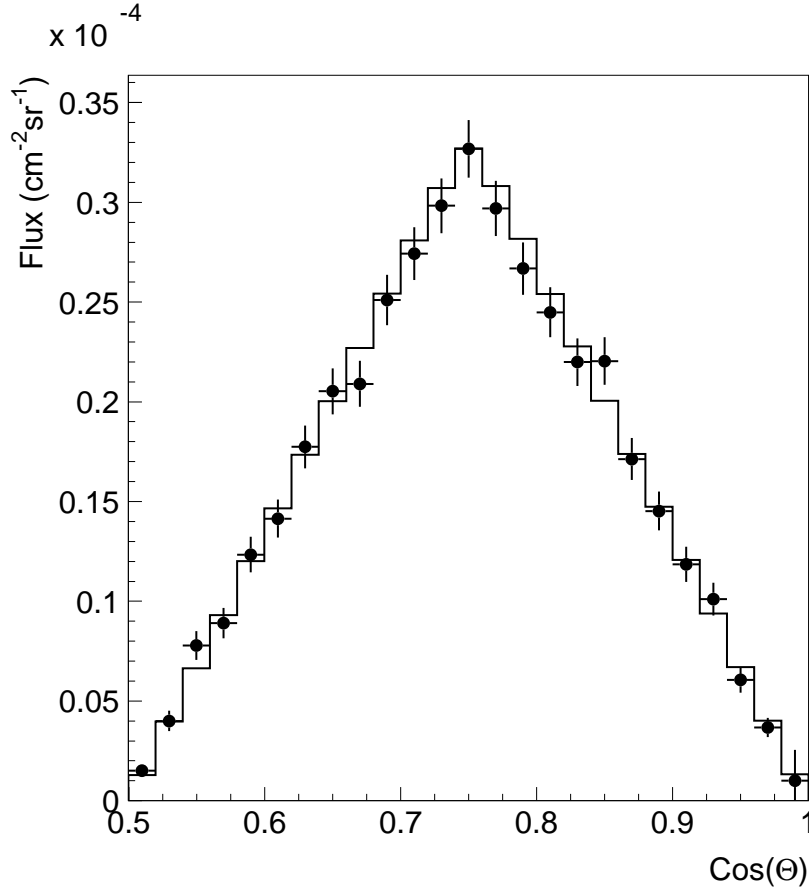

Fig. 6.6: Generated and reconstructed zenith angle distributions for the toy Monte Carlo setup. The generated distribution is indicated by the solid histogram, the reconstructed distribution by the markers and error bars.

6.3.2 Realistic Monte Carlo generator

The real Monte-Carlo generator employs the fixed opening-angle idea of the foregoing section. Events are generated homogeneously distributed over the surface of the disk and homogeneously in solid angle $d\phi_l \, d\cos\theta_l$ with respect to the axis of the cone. The disk has a radius of 77.6 m which limits the zenith angle to a maximum of $60°$. The detector is at a depth of about 45 m below the surface. The opening angle Θ of the cone has to be chosen large enough. Effects on the muon like scattering in the molasse and bending in the L3 magnetic field cause part of the muon tracks not to reach the scintillator barrel volume, while they would have reached it by extrapolating the initial direction on the surface disk. This effect can not be completely avoided. It can be minimized however, by choosing the opening angle of the cone such that it well covers the entire scintillator barrel. The *half opening angle* of the generator cone is fixed to $1.92°$. The phase space

used for the real generator is

$$\text{phase space} = \Sigma\Omega, \quad \begin{cases} \Sigma = \pi D^2 = 1.89 \cdot 10^8 \text{cm}^2, \\ \Omega = 2\pi(1 - \cos\Theta) = 3.53 \cdot 10^{-3} \text{sr}. \end{cases} \tag{6.8}$$

The acceptance is calculated as follows. The density of tracks in the phase space $[cm^2 sr]$ is constant. The equation for the acceptance thus is

$$\mathcal{A} = \frac{(\text{phase space})}{N_{\text{gene}}} \sum_{i=1}^{N_{\text{acc}}} w, \tag{6.9}$$

where phase space $= \pi D^2 \; 2\pi(1 - \cos\beta)$, β is the half-opening angle of the generator cone, N_{gene} is the number of generated tracks on the disk, N_{acc} is the number of accepted tracks and $w = \cos\theta$ is the normalized weight. When the zenith and azimuth angles are binned, the number of accepted tracks should be modified to the number of accepted tracks inside a certain angular bin. The acceptance then is the acceptance for that specific angular bin. The track momentum is *not* a phase space variable. However, when binning in momentum, the number of generated and accepted tracks should be modified to the number of accepted and generated tracks inside a certain momentum bin. The acceptance found is then the acceptance for that particular momentum bin.

The variance on the acceptance is given by

$$V(\mathcal{A}) = \frac{\text{phase space}}{N_{\text{gene}}} V\left(\sum_{i=1}^{N_{\text{acc}}} w\right), \tag{6.10}$$

with

$$V\left(\sum_{i=1}^{N_{\text{acc}}} w\right) = V(N_{\text{acc}}\langle w\rangle) = \langle w\rangle^2 N_{\text{gene}} p(1 - p), \tag{6.11}$$

and $p = \sum_{i=1}^{N_{\text{acc}}} w / N_{\text{gene}}$.

So far, we discussed only the angular and surface distribution of the cosmic-ray muons used in the generator. The distributions yet to be chosen are those of the charge and the energy of the muons. The charge distribution is chosen to be constant, with a charge ratio of 1.25. This coincides with the mean experimental charge ratio over a broad range of energies (Fig. 3.4). The energy distribution is chosen according to the following criteria:

– the mean time spent in generating one event should be reasonable,
– the distribution should be smooth within its bounds at the lower and upper energies, in order to prevent artificial effects due to jumps in the distribution,
– the edges should be outside the area of interest.

The first criterium is needed in order to assure the generation of many events in a reasonable time span. The time needed to generate a high energy event and track it down through the detector volume is far higher than the time needed for a low energy event.

To prevent jumps in the spectrum, we choose a simple energy distribution according to a power law:

$$\frac{\mathrm{d}N_\mu}{\mathrm{d}E_\mu} = cE^{-\gamma}, \quad \gamma = 2.7, \tag{6.12}$$
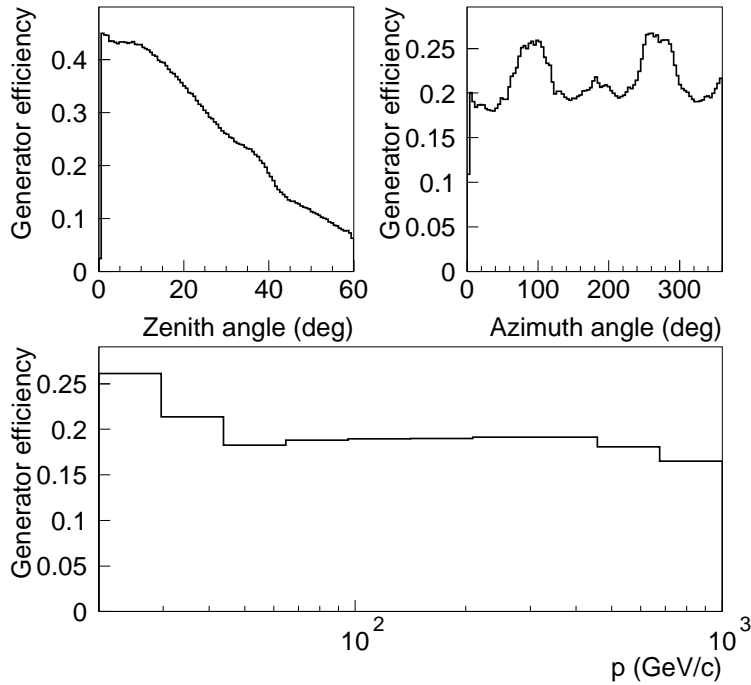
Fig. 6.7: Generator efficiency versus zenith angle, azimuth angle and momentum.

where c is a constant, such that it approximates the real cosmic-ray muon spectrum. The disadvantage of this type of distribution is the relatively low amount of high energy events being generated. The range in surface energy E is 18.8 GeV to 1 TeV.

A generated event was accepted if it crossed the scintillator barrel. In Fig. 6.7 the generator efficiency is shown versus zenith angle, azimuth angle and momentum. The efficiency is defined as the number of events with a track crossing the scintillator barrel over the total number of generated events. In Fig. 6.8, the effective geometrical acceptance is shown versus momentum. Note that it includes the detector efficiency, molasse acceptance and reconstruction efficiency. The geometrical acceptance of the scintillator barrel amounts to 19.9 m^{2}sr, for a zenith angle from 0 up to 60° and a uniform flux.

6.4 Simulation of elementary processes

A muon traversing matter will experience a loss of energy (mainly by ionisation) and its direction will be modified due to angular scattering. In addition, various interactions can take place, such as production of delta-rays, e^+e^- pair production and nuclear interactions.

During the simulation of the path traversed by a muon, either inside the detector or in the molasse, these interactions have to be taken into account in order to recover the particle properties at the surface level. Most of the secondary products of muon interactions are not interesting to us, since they will be stopped by the residual amount of molasse, or since they will not be detected. Some secondary products, especially hadronic particles can, however, lead to detectable signals inside the muon chambers. These signals
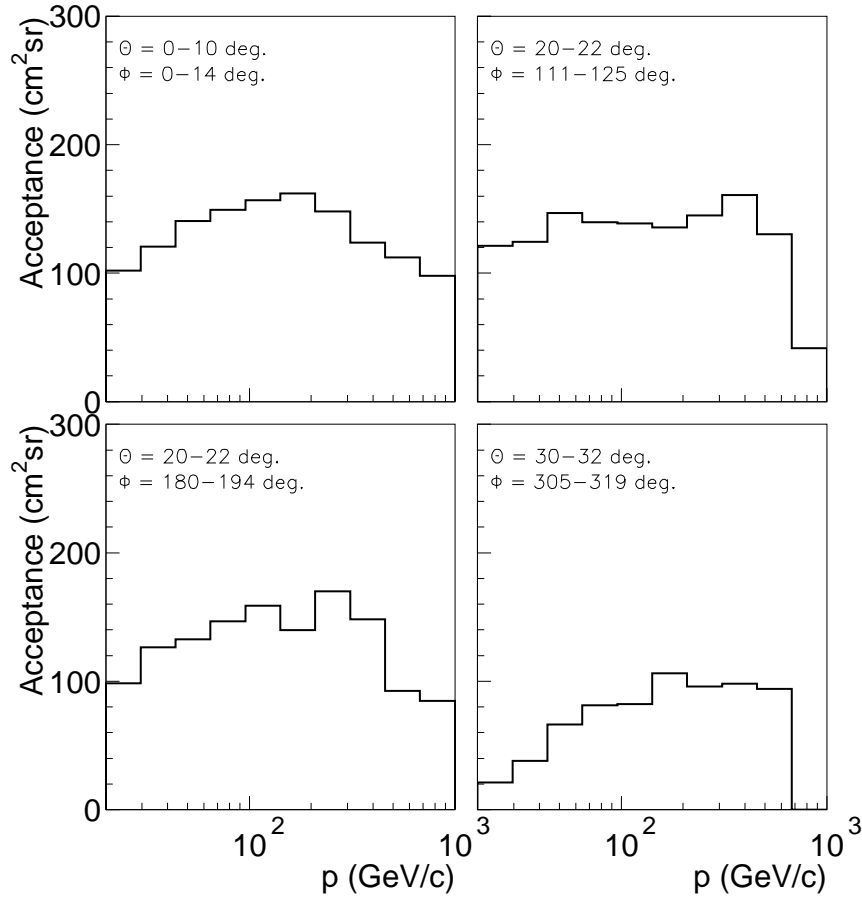
Fig. 6.8: The effective geometrical acceptance versus momentum for four different bins in zenith and azimuth angle.

can inadvertently be misunderstood as being produced by a muon, and so mislead the reconstruction of the supposed muon trajectory.

To simulate the energy loss of a muon, one can choose a few options. For instance, one can either use the mean energy loss or simulate all fluctuations. During event simulation, the GEANT package [73] is used to perform the necessary computations while during event reconstruction the GEANE package [82] is used. The reason is that during simulation we should simulate a real particle trajectory including all stochastic processes involved. During reconstruction, we assume a *mean energy loss and scattering amplitude* during the propagation of the muon. Secondary products are not generated in this case. The GEANE package also allows for an error calculation of the tracking parameters.

Event selection & data analysis

In this chapter we describe the selection and analysis of data and Monte-Carlo events. The selection criteria applied to the events are discussed. The results on the data calibration are shown and general quality checks are performed on data as well as on Monte Carlo. The method to obtain the muon momentum spectrum and the muon charge ratio is discussed. An evaluation of the statistical and systematic errors is presented. Finally, the results on the spectrum and charge ratio are shown.

7.1 Introduction

The data that are analyzed in this work were obtained from two major runs taken in 1991. These dedicated cosmic-ray muon runs were taken for the purpose of calibrating the L3 electromagnetic calorimeter [75]. To achieve this, it was only necessary that cosmic-ray muons could be reconstructed well inside the muon chambers on a track by track basis. At that time it was not the intention that these same runs would also be used to reconstruct the cosmic-ray muon momentum spectrum at the surface of the L3 plant. The use of these data on a run by run basis requires the necessary bookkeeping, which is similar as for the standard L3 physics runs. Especially important in this respect is that the level of functionality of the L3 detector and of the electronics is logged. Also the trigger settings at the time of data taking should be well described. It was not foreseen at that time that these dedicated cosmic-ray muon runs *were* going to be used on a run by run basis, namely by Bruscoli et al. [46] and in this work. As we will show in the next sections, the trigger settings were not fixed, and the trigger itself is not well described. Furthermore, the level of functionality of the L3 detector during the time of cosmic-ray data taking is not known. However, we *do* know the level of functionality just before and after the dedicated cosmic-ray muon runs. Assuming that it didn't change by much in between, the functionality is known well enough to be able to estimate the correction factor.

   The dedicated cosmic-ray muon runs were taken in March to April and in August to October 1991, see Tab. 7.1. The run numbers themselves are not contiguous inside one period of data taking.

Nr runs	Date		Run nr
34	March	13-14	241402-243602
121		16-22	245001-254101
43		24-26	255806-257004
177	April	2-13	257301-267905
111		22-29	274301-280501
37	August	30-31	333701-334403
47	September	1-2	334404-335701
89		27-30	343801-347901
24	October	1	348001-348503
Total 683			

Tab. 7.1. List of dedicated 1991 cosmic-ray muon runs.

7.2 Database status

During the time span in which the cosmic runs were taken, we need to know the behaviour of the detector, since the events written on tape are folded with the detector efficiency and acceptance. In particular, the behaviour of the muon-chamber high voltage system and the muon chamber cell status have to be known. Usually, between physics runs, an entry is created in the muon chamber database which tells the position and status of bad high-voltage cells. During the dedicated cosmic runs however, this database was *not* updated. Therefore, the best option left is to assume that during the dedicated runs the muonchamber high voltage status did not change appreciably. The status is read from the muon database in the range from April to October 1991, during which it was updated for standard LEP physics runs (see Tab. 7.2). Since during the cosmic runs there was no beam, the detector stability was likely to be better than during regular L3 physics runs. Therefore, the detector efficiency found here is a *lower limit*. The run numbers which are

Run nr	Date		Time
281001	April	30	09.25
...	...	...	...
348601	October	3	23.37

Tab. 7.2. List of lumlist (luml91.dat) entries used to sample the muon-chamber high voltage status.

used as entries for the database are sampled proportional to the integrated (beam-beam) luminosity of the run at the Z^0 energy peak. This might seem strange, but it is the only reasonable option for these cosmic-ray muon data.

7.3 Event selection

The raw events which are returned by the reconstruction program are of varying quality. This is due to the event topology inside the detector and to the reconstruction accuracy. due to the geometry of the muon chambers, tracks under large zenith angles are more likely to be P-doublet tracks instead of P-triplet tracks. Since doublets have a worse momentum

measurement than triplets, the quality of triplet data is higher than that of doublet data. In order to obtain a high-quality data sample, a selection is applied to the data as well as to the Monte Carlo. One has to take care that the simulated data are compatible with the reconstructed data, so the same cuts should be applied to both data and Monte Carlo.

In order to simulate the cosmic muon trigger, the following cuts were imposed on the Monte Carlo and the data:

– There must be *at least one* MUTK track present in the event. The DAQ trigger required a signature of a track in two octants, separated by at least one octant. However, such a signature means that there should be a couple of hits which *could* resemble a track. As one learns by scanning real events, it commonly occured that events were triggered which, after reconstruction, only show one MUTK track and some separate hits in another octant. The number of events which only contain hits without the reconstruction being able to reconstruct tracks out of them is negligible.

– The MUTK track must have crossed the scintillator barrel. The number of crossings must equal two, once across a tile in the upper half of the barrel and once across a tile in the lower half of the barrel. In both halves of the barrel there must have been a *real* scintillator hit.

As expected, the influence of these cuts on the data is, within a small variation, just an overall reduction (Fig. 7.1). The Monte Carlo shows a selection efficiency strongly depending on the zenith angle. This is mainly due to the fact that the generated zenith angle distribution for the Monte Carlo is different from the natural zenith angle distribution. It are the selection efficiencies *after* the software trigger simulation, however, that are important, i.e. *these* selection efficiencies should be the same for data and for Monte Carlo. The data that have been selected by the trigger simulation cuts are further exposed to the following quality cuts:

– The number of events in a run must be larger than 500. This keeps the statistical error on the rate from a run below about 5%.

– A track should not pass through the magnet doors. This cut is imposed by requiring that the absolute z ordinate of a track at the LEP3 volume is less than 709.5 cm. The reason why this cut is imposed is that the number of tracks passing the doors, being reconstructed *and* passing the selection criteria is very low, due to the geometry of the muon chambers. The tracks which *are* selected have a relatively large systematic error. By cutting away these tracks, we avoid any systematic effects in the flux measurements at large angle.

– The number of P-hits is cut at 800, the number of Z-hits is cut at 400. The number of raw hits in either the P- or Z-chambers has a maximum of 5000 each, limited by the reconstruction software. Events which contain more than 5000 P- or Z-hits are truncated and do not contain the full physics content of the actual event. For a normal event containing a single muon track that passes close to the vertex, the number of P hits is about 112 and the number of Z hits is about 16. All additional hits are either generated by knock-on electrons or by electronics noise. For tracks passing the vertex at larger distance, the number of hits is larger due to the fact that the track passes through more cells. The distribution of the number of raw hits in the P- and Z-chambers, before and after event selection, is shown in Fig. 7.2 for both data and Monte Carlo events. From these distributions we see that the data contain much more noise than the Monte Carlo.
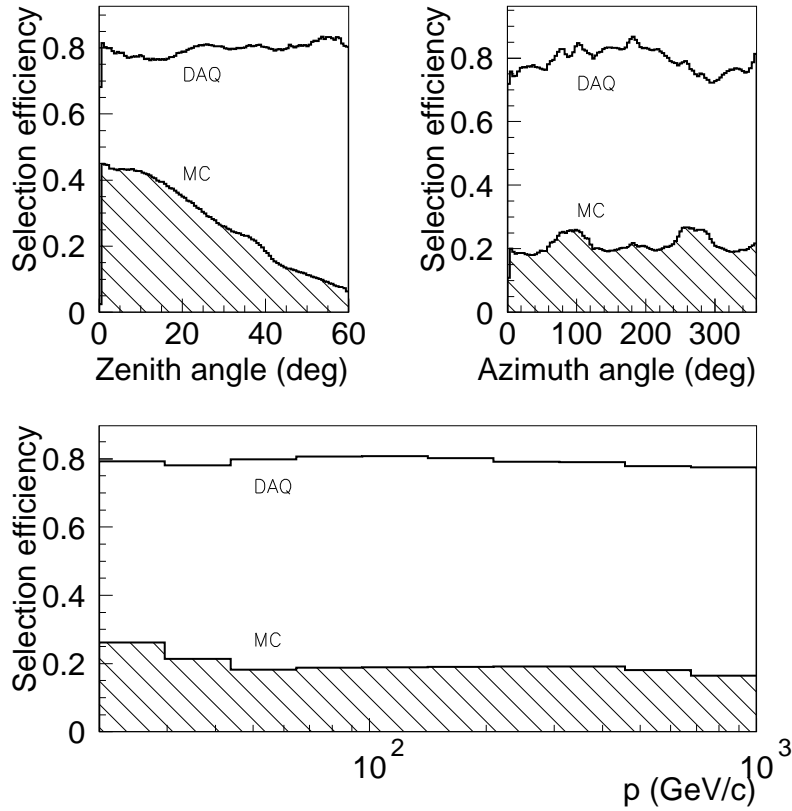
Fig. 7.1: Trigger selection efficiency for data (DAQ) and Monte Carlo (MC).

Since we are selecting single-muon events, care should be taken that the cut on the number of raw hits does not exclude too many single-muon events. The cuts still allow a lot of noise to be present in an event, but the physics contents of the events of interest is not touched significantly. The effect of a variation of these cuts is investigated in Sec. 7.16.2.

– An event should contain one and only one inward track. The cosmic-ray muon Monte-Carlo generator generates only single-muon events. Since the Monte Carlo must be comparable to the data, this means that only single-muon events will be used in the current analysis. For this reason, we select events with one and only one inward track, an inward track being a track in one of the upper octants. We only select the inward part of the tracks since this part does not have to be tracked back *through the inner detector* towards the LEP3 volume, as is the case for outward tracks. By excluding multi-muon events, we bias the overall cosmic-ray muon flux in a downward direction (on the percent level), which has to be taken into account later on.

– The MUTK track must contain 3 P-segments and 2 Z-segments. This is a cut on the quality of the MUTK track inside the muon chambers. The precision of the momentum reconstruction is significantly better for P-triplets than for P-doublets. The requirement
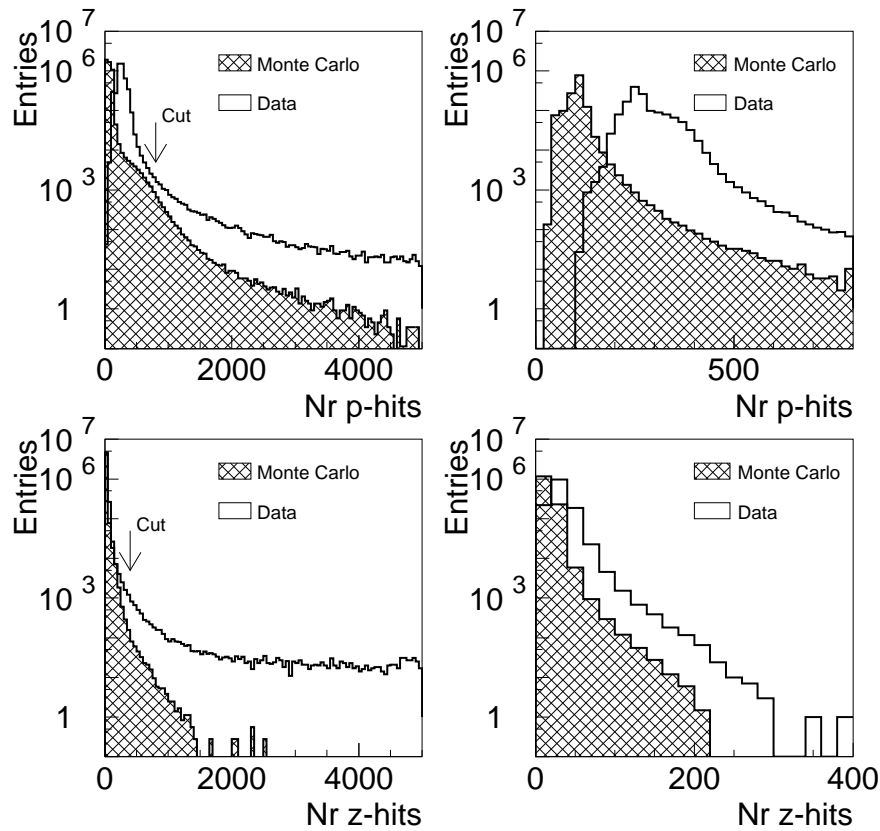
Fig. 7.2: Raw hit distributions for P- and Z-chambers, for data and Monte Carlo. The left plots show the raw distributions, the right plots show the distributions after all cuts have been applied.

of a Z-doublet track selects those tracks which have an accurate λ angle.

– The backtracking of the MUTK track towards the LEP3 volume must have been successful. A small fraction of events do not succeed in this, due to (GEANE) tracking failures.

– The backtracking of the MUTK track towards the surface must have been successful. A small fraction of events do not succeed in this. This is due to the multiple scattering in the molasse and a small positional shift inside the detector due to finite reconstruction accuracy. Events generated close to the edge of the surface disk can easily fall beyond the maximum radius of this disk after reconstruction due to these causes. This is true for Monte Carlo as well as for data.

– The Pearson-r matching parameter must be larger than 0.99. Tracks found in the upper and lower octants are matched at the vertex plane. For the matching, the *Pearsons-r* algorithm is used, see Sec. 5.4.3, which returns a parameter r that indicates how well two track pieces match each other. In Fig. 7.3 the distribution of $1 - r$ is shown, before and after event selection. The agreement between data and Monte Carlo is reasonable.

The effect of a variation of this cut is investigated in Sec 7.16.2.
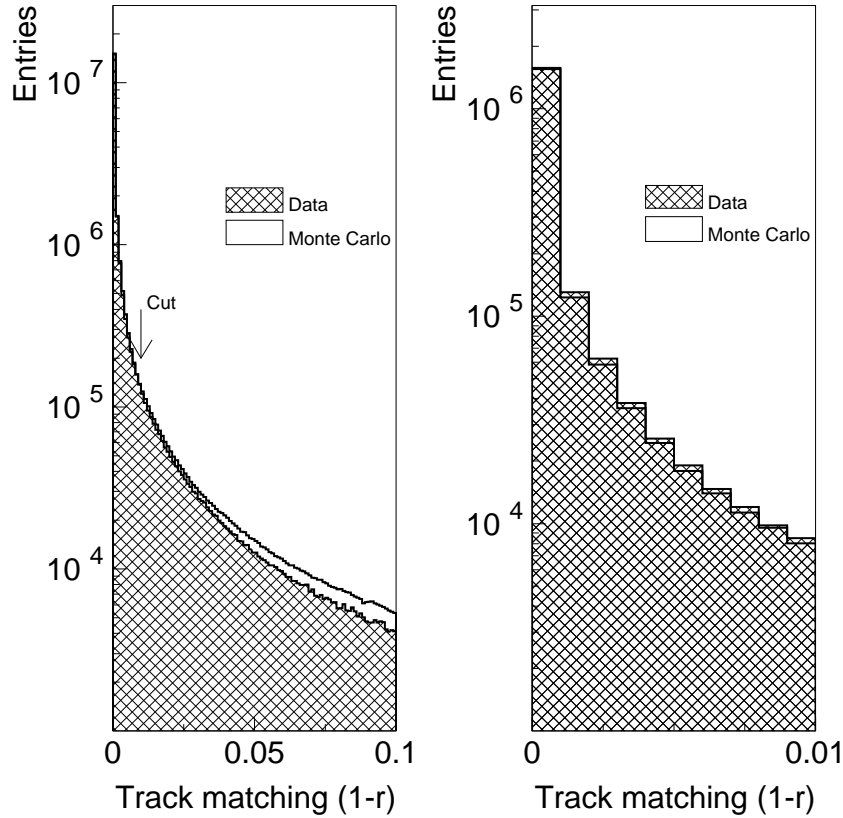
Fig. 7.3: Distribution of the (1-r) parameter of track matching at the vertex plane. The left plot shows the raw distribution, the right plot shows the distribution after all cuts have been applied.

– The χ^2 of the swimfit must be less than 0.001. The number of degrees of freedom of the swimfit is zero. That's why the χ^2 distribution peaks at zero, instead of at a finite positive value. In Fig. 7.4 the swimfit χ^2 distribution is shown, before and after event selection. The agreement between data and Monte Carlo is reasonable. The effect of a variation of this cut is investigated in Sec 7.16.2.

In order to be able to simulate the trigger efficiency during the run, the trigger conditions should be well known. For the data used in this work these conditions are only partially known however. From the data we can conclude that at least a few different trigger conditions existed during the dedicated cosmic-ray muon runs. For a fixed trigger condition, the event rate should only vary due to natural effects (pressure, temperature etc.). In Fig. 7.5 the event rate is shown versus the day of the year 1991, together with the atmospheric pressure at 11.5 km altitude, for all recorded events. The runs having a rate above 3.9 Hz are rejected since these clearly imply different trigger conditions with
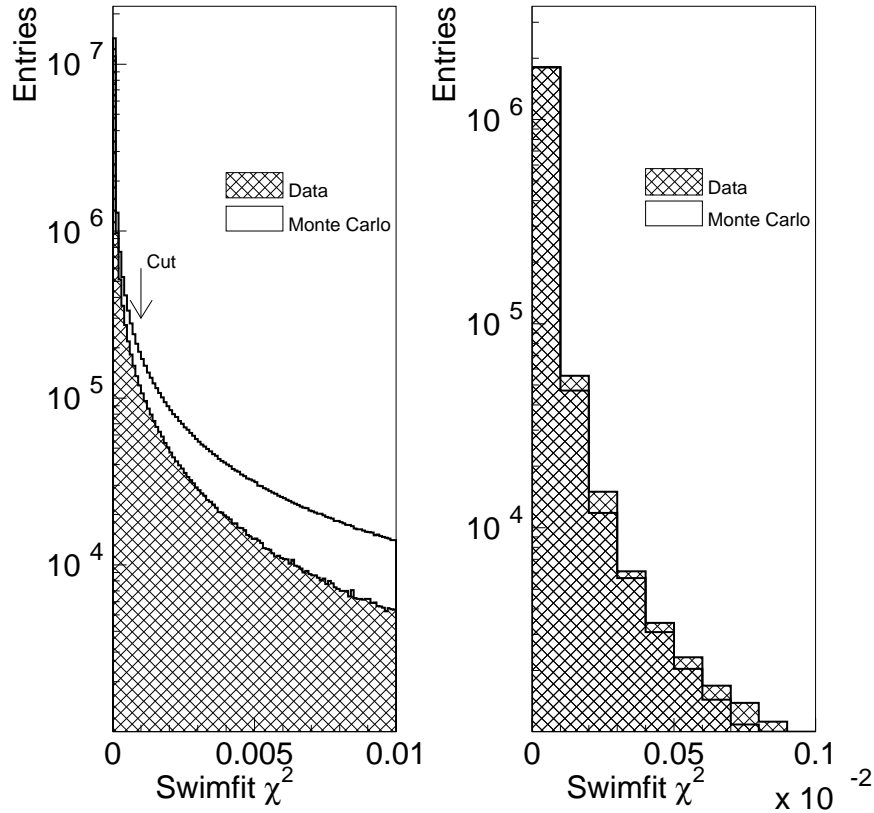
Fig. 7.4: Distribution of χ^2 of track swimfit. The left plot shows the raw distribution, the right plot shows the distribution after all cuts have been applied.

respect to the rest of the data sample. The remaining runs, display an overlap in event rate. Still, the groups of runs are shifted with respect to one another, even taking into account the different values of atmospheric pressure. This effect has to be taken into account in the estimation of the systematic error of the flux. By scanning events we can conclude that the influence of electronics noise on the rate can be neglected.

In Fig. 7.6 the event selection efficiency ε is shown for the data. There are two clear peaks visible near 27 and 32% which are due to a difference in data quality versus time. The data quality can be influenced by differences in the detector setup or by differences in the cosmic-ray muon trigger setup. In this work, we assume that the detector setup is fixed during the entire period of data taking. The variation in selection efficiency should then entirely be due to variations in the trigger setup. In Fig. 7.7, the selection efficiency is plotted versus zenith angle, azimuth angle and momentum for data and for Monte Carlo, after the data samples have been soft-triggered. The efficiencies for data and Monte Carlo mutually agree within about 10%. In Tab. 7.3, the *rejection* efficiencies for the different cuts are given, as well as the total numbers of raw and selected events. The selection cuts are applied in the order as they appear in the table. In Tab. 7.4, the live time and event rates are given. The raw live time is the total time span from the first to the last event. The selected live time is the total live time used to normalize the momentum spectrum.

Raw sample	$55.5 \cdot 10^6$ (MC, un-triggered)	
	$3.8 \cdot 10^6$ (MC, soft-triggered)	
	$4.8 \cdot 10^6$ (DAQ, hard-triggered)	
	$3.1 \cdot 10^6$ (DAQ, soft-triggered)	
Selection cut	Nr rejected events	Rejection efficiency (%)
Event rate ok	$80.1 \cdot 10^3$ (DAQ)	2.6
Nr events per run > 500	$6.4 \cdot 10^3$ (DAQ)	0.2
≥ 1 MUTK track present	$33.6 \cdot 10^6$ (MC)	60.5
	$7.8 \cdot 10^5$ (DAQ)	16.3
Scint barrel crossing ok	$13.1 \cdot 10^6$ (MC)	23.6
	$8.0 \cdot 10^5$ (DAQ)	16.7
Not through doors	$3.7 \cdot 10^5$ (MC)	9.7
	$1.8 \cdot 10^5$ (DAQ)	5.8
LEP3 backtracking ok	773 (MC)	0.02
	656 (DAQ)	0.02
SURF backtracking ok	$6.0 \cdot 10^3$ (MC)	0.2
	$6.4 \cdot 10^4$ (DAQ)	2.1
Single muon event	$1.5 \cdot 10^4$ (MC)	0.4
	$2.6 \cdot 10^4$ (DAQ)	0.8
Not too many P/Z hits	285 (MC)	0.0001
	$1.4 \cdot 10^3$ (DAQ)	0.0005
P-triplet	$1.2 \cdot 10^6$ (MC)	31.6
	$7.7 \cdot 10^5$ (DAQ)	24.8
Z-doublet	$5.4 \cdot 10^5$ (MC)	14.2
	$5.7 \cdot 10^5$ (DAQ)	18.4
Swimfit χ^2 ok	$1.1 \cdot 10^4$ (MC)	0.3
	$8.4 \cdot 10^3$ (DAQ)	0.3
Pearson r ok	$1.5 \cdot 10^5$ (MC)	3.9
	$1.7 \cdot 10^5$ (DAQ)	5.5
Final sample	$1.9 \cdot 10^6$ (MC)	50.0
	$1.4 \cdot 10^6$ (DAQ)	54.8

Tab. 7.3. Event selection for Monte Carlo (MC) and data (DAQ). The number of *rejected* events is shown after all previous cuts have been applied. The terms hard- and soft-triggered mean that events were triggered by the hardware or by the software trigger simulation. The rejection efficiencies are with respect to the soft-triggered samples.

Raw live time	$1.37 \cdot 10^6$ s
Selected live time	$1.13 \cdot 10^5 \pm 16.2$ s
Rejected live time	$3.71 \cdot 10^3$ s
Mean event rate	3.65 Hz
Real event rate	16.22 Hz

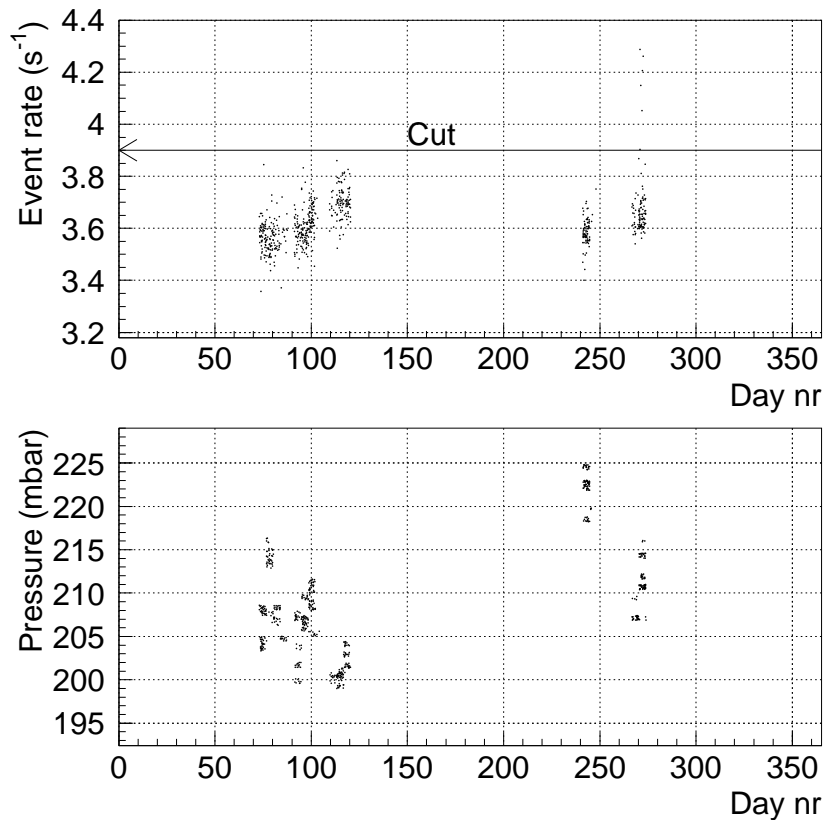**Tab. 7.4.** Live time and rates as obtained from the data.

Fig. 7.5: Event rate and atmospheric pressure (at 11.5 km altitude) versus day of 1991. Each dot represents the mean rate or pressure of a run.

The rejected live time is the time span that was rejected because of the fact that the time between two consecutive events exceeded the 10 second limit (see Sec. 7.10). The mean event rate is the mean trigger rate. The real event rate is the number of triggers per gate-open time span.

7.4 Event trigger

The cosmic-ray muon trigger does not involve any other external signal than the simulated beam-gate signal. This beam-gate signal, usually derived from the signal given by the beam pickup coil, is replaced by the clock source of the BGO read-out electronics [75]. The trigger is a combination of a muon-chamber trigger and a scintillator-barrel trigger. The muon-chamber trigger requires the occurrence of a track signature in two different octants, separated by at least one octant. This condition reduces the muon-chamber trigger rate due to cosmic-ray muon tracks crossing the muon chambers at large distance from the vertex. From Tab. 7.3, the number of events that contained *no* MUTK track is found as 16.3%. The scintillator trigger requires that at least one tile is hit simultaneously in the
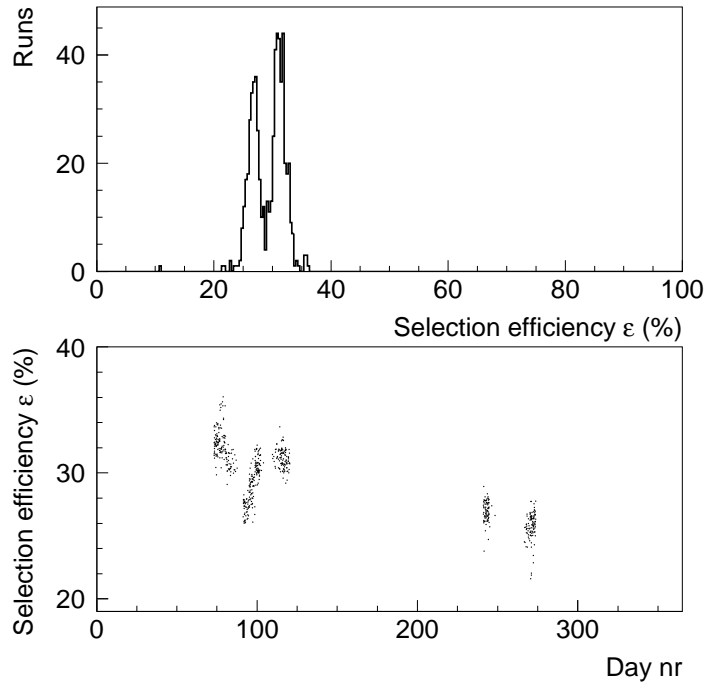
Fig. 7.6: Distribution of event selection efficiency ε for data and its variation versus 1991 day number. The selection efficiency is versus the hard-triggered event sample.

upper *and* in the lower half of the barrel. The condition on simultaneity eliminates most spurious hits from the HCAL uranium noise.

There may have been an additional trigger condition, that limited the distance of closest approach (DCA) of the tracks to the vertex. In that case, tracks would be likely to pass the BGO crystals almost parallel to their longitudinal axis. Investigation of the DCA distribution shows, however, that either this cut did not exist or that it was compatible with the requirement that tracks should cross the scintillator barrel volume. In Fig. 7.8 the DCA distributions in the xy-plane and in the yz-plane are shown for the data, before and after the complete event selection. The zenith angle was limited to $10°$ at maximum and the momentum had to be 50 GeV/c or more, in order to make any deviation from the expected distributions more clear.

The distribution of events in the 5 μs gate (see Sec. 4.3) should be flat. This is due to the fact that the gate width is much smaller than the period of the cosmic-ray muon rate of about 16 Hz. In Fig. 7.9, the distribution inside the gate is shown for selected events. The horizontal axis displays the number of TDC counts. The range of TDC counts coincides with the gate width of 5 μs. The peak structure is probably due to the electronics and has nothing to do with the real-time distribution of the muons inside the gate. Only the mean distribution is important here.

The rate distribution inside a run can be examined by counting the number of events per time interval. In Fig. 7.10, this distribution is shown for a time interval of 360 s. The distribution is a Gaussian with a mean corresponding to 360 times the mean rate of about 3.6 Hz. The width of the distribution depends on the length of the time interval and

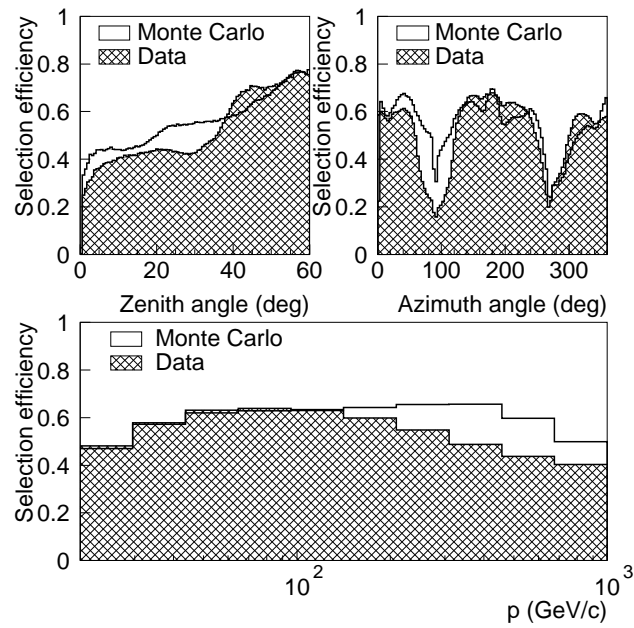Fig. 7.7: Event selection efficiencies for data and Monte-Carlo versus zenith angle, azimuth angle and momentum. The selection efficiency is versus the soft-triggered event sample.
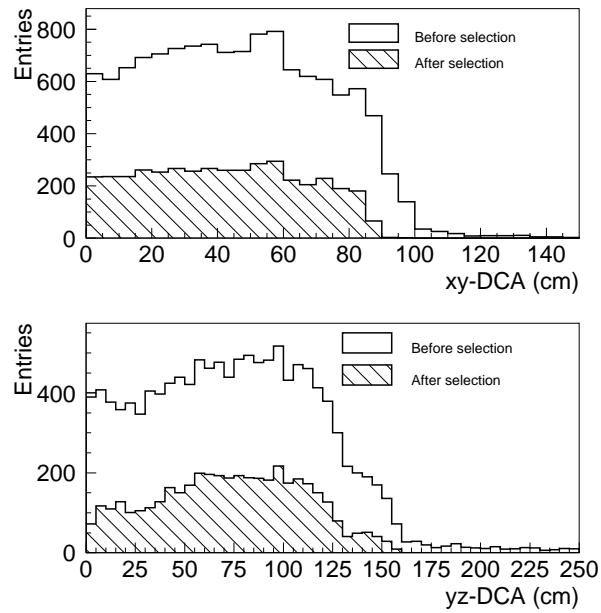

Fig. 7.8: The DCA distributions for data, before and after event selection, in the xy-plane and in the yz-plane.
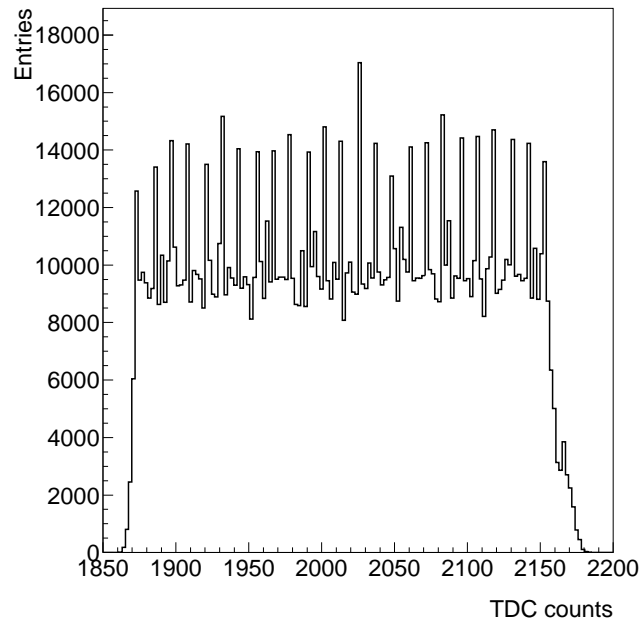
Fig. 7.9: Distribution of events inside the gate of width 5 μs.
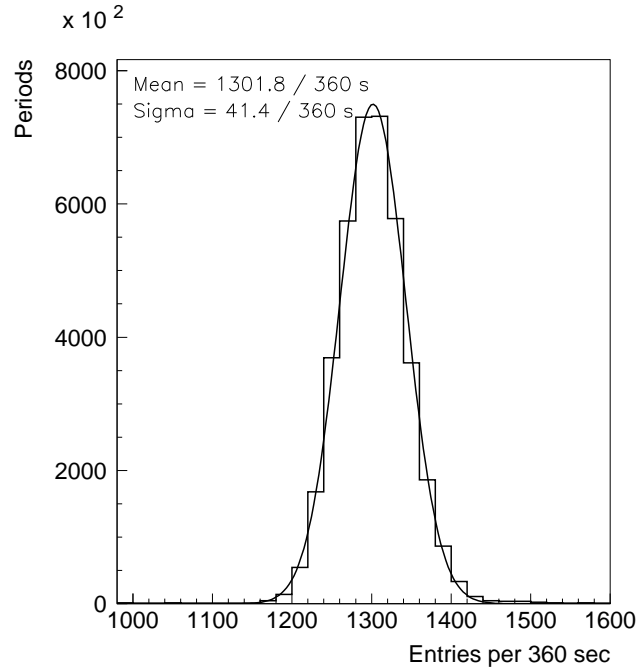

Fig. 7.10: Distribution of number of events per 360 seconds.

decreases with $1/\sqrt{N}$ where N is the mean number of triggers inside an interval. From the mean of the Gaussian we would expect a natural variation of $\sqrt{1302}/(360\text{s}) = 36.1/(360\text{s})$, if the variation would entirely be due to this statistical effect. The variation due to other effects like different trigger settings then is equal to $\sqrt{41.4^2 - 36.1^2}/(360\text{s}) = 19.4/(360\text{s})$. Translated to a variation of the rate, this means 0.054 Hz on a mean rate of 3.6 Hz. This is a systematic error on the trigger rate of 1.5%.

So far, we did not yet speak about the uranium generated noise from the HCAL. This noise is of influence on the cosmic-ray muon trigger, since it generates random coincidences between an upper and a lower scintillator tile. The rate with which this happens is 19 ± 1 kHz [70]. So, about once in three 22 μs cycles there is a scintillator coincidence signal from the uranium noise. A coincidence with the gate happens with a rate of about $f_{\text{noise}} \cdot T_{\text{gate}}/T_{\text{total}}$, or 5.3 kHz. The number of spurious scintillator triggers then equals 1 per 8 gate open occurrences. Such a fake scintillator trigger can lead to a global trigger if in that same gate a muon track is present in the muon chambers which *does not* have to cross the scintillator barrel. Actually, there are many events present with tracks not crossing the scintillator barrel. These must have been triggered by the uranium noise. From Tab. 7.3 we find that 16.7% of the events with at least 1 track do not have a track crossing the scintillator barrel. Since, however, we *demand* tracks crossing the scintillator barrel, the effect of the uranium noise on the measured cosmic-ray muon rate is thought to be negligible. It can at most lead to a slightly deteriorated precision of the momentum measurement of the (falsely) triggered track.

7.5 Calibrations

The accuracy with which the muon momentum is reconstructed is largely determined by the accuracy of the track segments. The swimfit (Sec. 5.4.2) uses the segment coordinates to fit the final momentum of the track. The accuracy with which the segments are constructed depends on the T0 offsets applied to the drift time and on the determined drift velocity. Thus, the T0 offsets and the drift velocity have to be calibrated. The calibration is performed using segments which cross a sense or mesh plane (see appendix A). We describe the results of the calibration below.

7.5.1 T0 offset calibration

The calibration of the various T0 offsets is important for a good reconstruction of muon tracks. The T0 offsets can be divided in P-chamber offsets and Z-chamber offsets. For each of these two groups there exists a global T0 offset and offsets per muon chamber octant. Usually the local octant T0 offsets are calibrated first, after which the global offset is calibrated. The importance of the global offset can be seen from Fig. 7.11, in which the momentum precision is plotted versus the global T0 offset for a 1994 dimuon data sample. The precision is obtained from a fit of a Gaussian to the dimuon momentum peak. The T0 shift is relative to the standard (calibrated) offset. As can be seen, the standard value of the global T0 offset is mis-calibrated by about 0.8 ns for these data.

The behaviour of the momentum precision versus T0 offset can be described by a simple model:

$$\sigma(p)/p^2 = 6.4 \cdot 10^{-6}\sqrt{\sigma_{\text{intr}}^2 + 0.5v_{\text{dr}}^2\Delta^2 T_0}, \tag{7.1}$$

where p is the momentum, σ_intr (in units of length) is of the order of the intrinsic accuracy of the sagitta measurement, v_dr is the drift velocity in the muon chambers and ΔT_0 is the shift in the global T0 offset with respect to the calibrated value. Since this expression does not depend on the exact value of the momentum, it is thought to be valid also for other momenta than just at the dimuon peak.
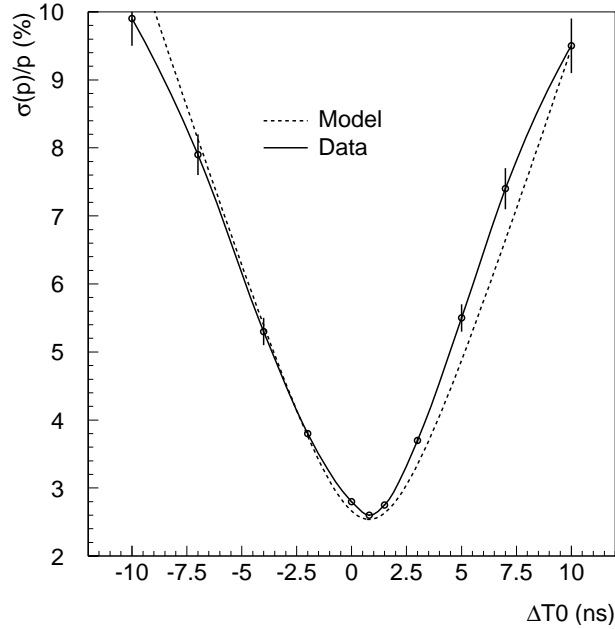

Fig. 7.11: The momentum precision for dimuon events versus shift in global P-chamber T0 offset. The full curve is an interpolation performed on the data-points. The dashed curve is a model-fit to the data points (see text).

The T0 offset calibration is shown in Fig. 7.12. The width of the T0 distribution of 3.7 ns results in a momentum precision of about 4.5% at 1 sigma which is still a reasonable value. The single-wire precision is about 200 μm. With a drift velocity of 50 μm/ns, this results in 4 ns precision per wire. The fits to the hits use about 8 to 12 hits, so that the overall accuracy *in the direction of the drift-path* is better than 4 ns. The algorithm with which the T0 correction is calculated is of limited precision however. The small peaks visible in the plot near -9 and +5 ns are caused by the fit algorithm.

7.5.2 Drift velocity calibration

The drift velocity was calibrated by analyzing segments crossing the mesh planes. It is difficult to calibrate since the drift velocity is influenced by the muon-chamber gas temperature and pressure. Thus, one can expect to see slight deviations from a nominal drift-velocity calibration. In Fig. 7.12, the residual drift velocity is shown. The two peaks close to the main peak are caused by the fit algorithm. The small bump to the left is most likely due to chambers with different gas characteristics. The corresponding chambers are not eliminated.
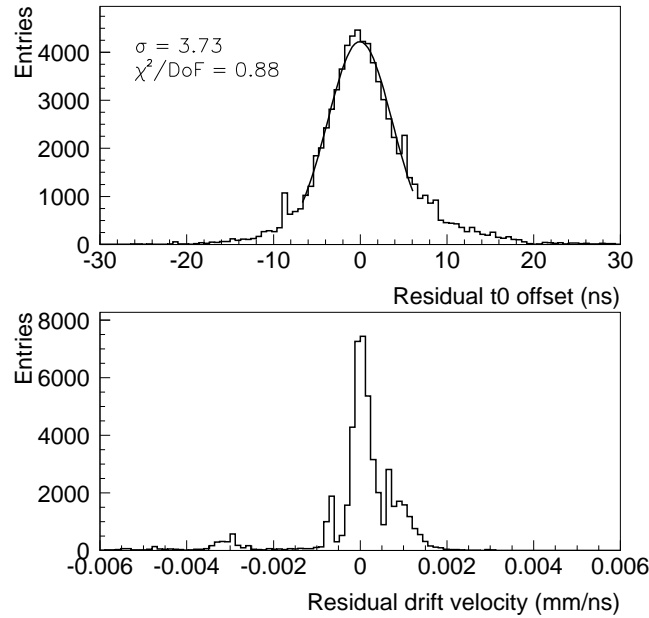
Fig. 7.12: Residual T0 offset and drift velocity for 1991 cosmic muons.

7.6 Momentum precision

The momentum precision is measured for both dimuon events and cosmic-ray muon events. It is important that the momenta are reconstructed accurately. However, it may be possible to compensate for mis-reconstructions by a deconvolution process (to be discussed in Sec. 7.12).

7.6.1 Dimuon events

In order to check the precision with which *P hits* are reconstructed, the so-called *single-wire precision* is a good variable to examine. For any P segment, we can concentrate on three consecutive hits, i.e. hits from three consecutive wires. The sagitta measured from three consecutive hits is defined as

$$S = X_2 - (X_1 + X_3)/2, \tag{7.2}$$

where X_2 denotes the x ordinate of the middle hit. For the error on this sagitta we find

$$\sigma_S = \sqrt{\sigma_{X_2}^2 + \frac{\sigma_{X_1}^2}{4} + \frac{\sigma_{X_3}^2}{4}} \tag{7.3}$$

The errors are assumed to be the same (σ) for all wires, so we get

$$\sigma_S = \sqrt{3/2}\,\sigma. \tag{7.4}$$

Thus, the value of the single-wire precision σ can be found from the three-hit sagitta distribution by multiplying its width with a factor $\sqrt{2/3}$. Since the span of such a '3-hit'

track is small with respect to the track length, we can consider it to be a straight line. Thus, any deviation from the three hits not lying on a straight line is due to the intrinsic accuracy of the drift-distance measurement. In this measurement also the cell-map and hit reproduction routines are involved.

In Fig. 7.13 the single-wire precision is plotted for segments in the inner region of a P-cell, for segments crossing the sense wires and for segments crossing the mesh wires. The obtained precision is better than the precision obtained in [83] and the one estimated in [84]. It should be noted that, although the single-wire precision tells much about the accuracy of the muon-chamber system, its importance depends also on the relative magnitude of systematic errors in the cell-map.

The momentum precision for dimuon *tracks* has been measured by reconstructing the Z^0 mass. Only a few cuts were applied to the data:

– Three P segments and two Z segments per track,
– Two and only two tracks per event,
– Acollinearity less than 1.5 degrees.

The acollinearity is defined as the sharp angle between both muon tracks,

$$\alpha_{\text{aco}} = \pi - \arccos(\cos \lambda_1 \cos \lambda_2 \cos(\phi_1 - \phi_2) + \sin \lambda_1 \sin \lambda_2), \tag{7.5}$$

where ϕ and λ are defined in the L3 coordinate system. The cut removes most of the events with final state radiation (Fig. 7.14). The momentum precision after the cuts have been applied is found to be 3.8% (Fig. 7.15), in agreement with measurements by other authors of the L3 collaboration [83; 51].

7.6.2 Cosmic-ray muon events

For cosmic-ray muon events, the single-wire precision for data is slightly worse than that found for dimuon events (Fig. 7.16). A possible reason is that the distribution of the tracks versus angles and position in a P-cell is different for cosmic-ray muon tracks than for (di)muon tracks from the vertex. The single-wire precision for Monte Carlo is better than that for dimuon events, as expected. The relatively narrow width of the distributions indicates that the Monte Carlo is not well tuned to the data.

In Fig. 7.18, the momentum precision is shown versus the momentum inside the muon chambers for events with two P-triplet and Z-doublet tracks. The momentum precision is obtained as the width of a Gaussian fit to the distribution of $\sigma(1/p)/(1/p)$, where p is the mean momentum of both the (upper and lower) tracks. The precision is worse than that expected from the dimuon events by extrapolation. This can be due to the following reasons:

– The width of the T0 calibration distribution (Fig. 7.12) allows for a small mis-calibration of the T0 offsets. This can influence the momentum precision.
– The angular distribution and range of cosmic-ray muons is different than for dimuons. This influences the accuracy with which tracks are reconstructed.
– The cell-map is only accurate for tracks nearly parallel to the wire plane of a P-cell. For tracks under larger angle with respect to the wire plane, the momentum precision thus deteriorates.
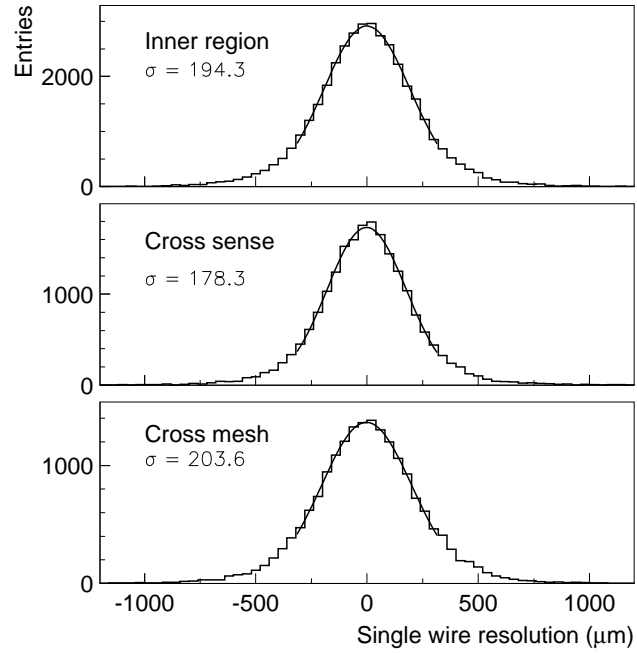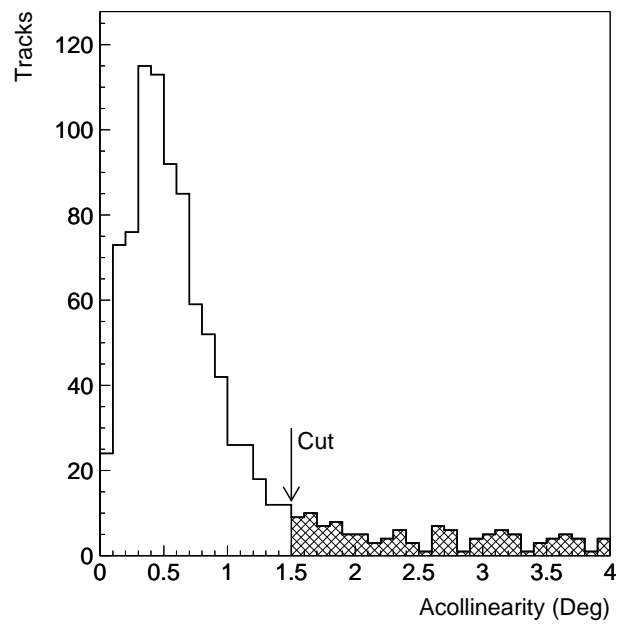
Fig. 7.13: The dimuon single-wire precision.

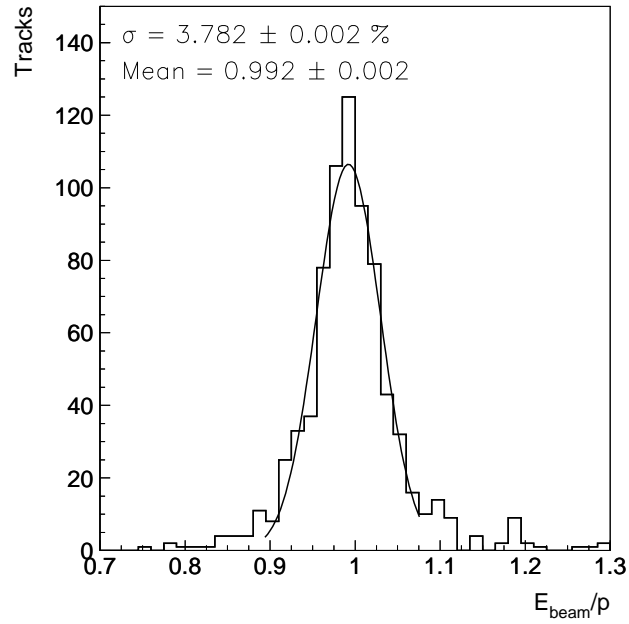Fig. 7.14: The dimuon acollinearity distribution.

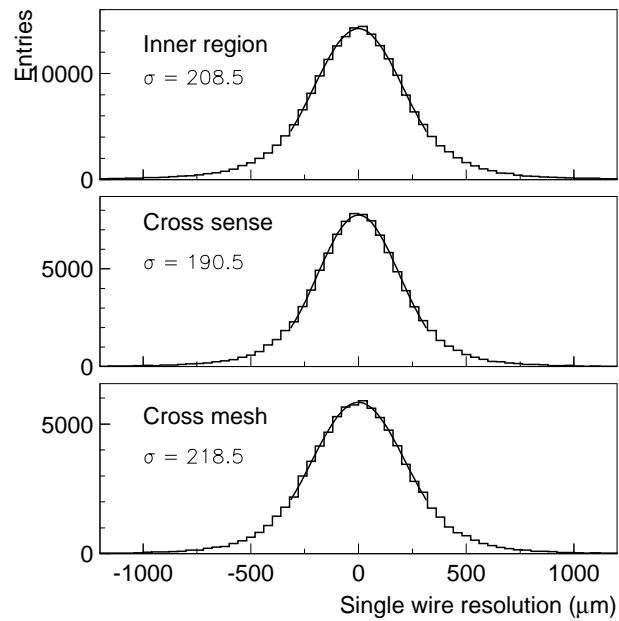Fig. 7.15: Dimuon momentum distribution after cuts being applied.

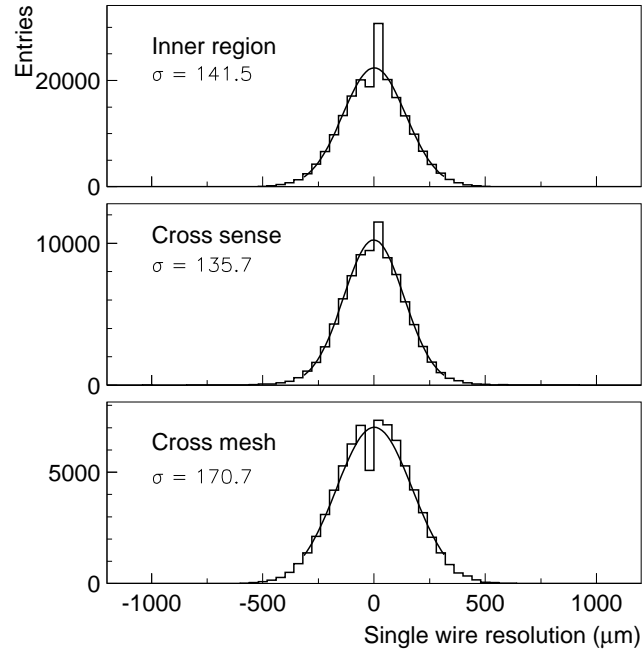Fig. 7.16: The data cosmic-ray muon single wire precision.

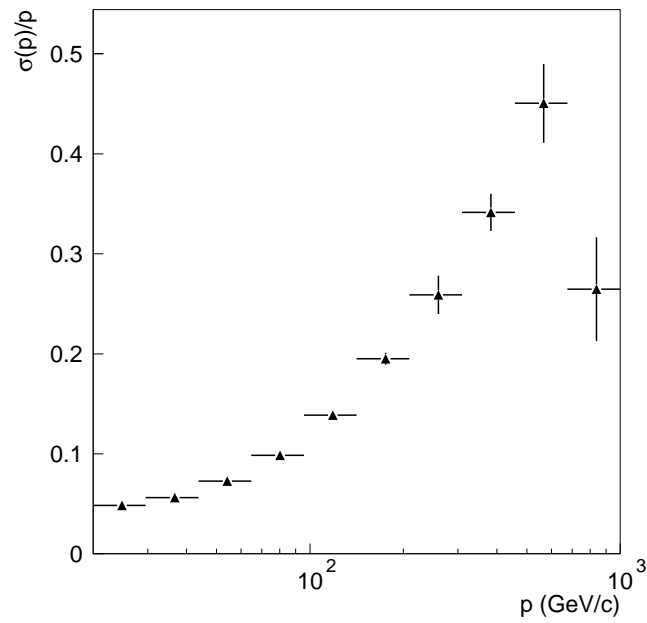Fig. 7.17: The Monte Carlo cosmic-ray muon single wire precision.

Fig. 7.18: Momentum precision for data versus muon chamber momentum for triplet-triplet events.

7.7 Charge confusion

The charge as measured by the L3 muon chambers depends on the direction of the track curvature. Since estimation of the track curvature is in fact a momentum measurement, it follows that the accuracy of the charge assignment to a track depends on the precision of the momentum measurement (see Sec. 3.2.2). The charge confusion coefficient can be obtained from the data, directly. This is preferred over obtaining it from the Monte Carlo, since the Monte Carlo does not describe the data momentum precision precisely. We consider events with two good track pieces (P-triplets and Z-doublets), so an upper and a lower track. Both pieces are measured independently with equal precision, so that the chance of charge confusion is equal for both of them. We neglect here the small difference in momentum between both pieces. Let N_{reco} denote the total number of tracks consisting of pairs of equally charged track pieces and pairs of opposite charged track pieces:

$$N_{\mathrm{reco}} = N^{++} + N^{--} + N^{+-} + N^{-+}, \tag{7.6}$$

where N^{+-} and N^{-+} denote the events with opposite charged track pieces and N^{++} and N^{--} denote the events with equally charged track pieces. The chance that *one* track piece suffers charge confusion is set to p. The relative number of oppositely charged track pieces then equals

$$T \equiv \frac{N^{+-} + N^{-+}}{N_{\mathrm{reco}}} = 2p(1 - p). \tag{7.7}$$

This equation can be solved in p, using that the charge confusion is zero for $T = 0$:

$$p = 0.5 \cdot (1 - \sqrt{1 - 2T}). \tag{7.8}$$

The charge confusion coefficient then equals

$$C = 2 \cdot p = 1 - \sqrt{1 - 2T}, \tag{7.9}$$

where the charge confusion coefficient has been *defined* to be 100% at maximum. The measured number of equally signed track pieces is related to the real number of equally signed track pieces as

$$N^{++}_{\mathrm{meas}} = p^2 N^{--}_{\mathrm{real}} + (1 - p)^2 N^{++}_{\mathrm{real}}, \tag{7.10}$$
$$N^{--}_{\mathrm{meas}} = p^2 N^{++}_{\mathrm{real}} + (1 - p)^2 N^{--}_{\mathrm{real}}. \tag{7.11}$$

Via these equations, the real charge ratio R_{real} can be found from the measured charge ratio R_{meas} as

$$R_{\mathrm{real}} = \frac{p^2 - (1 - p)^2 R_{\mathrm{meas}}}{p^2 R_{\mathrm{meas}} - (1 - p)^2}. \tag{7.12}$$

In Fig. 7.19, the charge confusion coefficient is shown as obtained from the data for near vertical muon tracks.

7.8 Atmospheric pressure correlation

To test the hypothesis that the muon rate depends on the atmospheric pressure (and temperature), the data used in this thesis have been examined for any correlation. Since
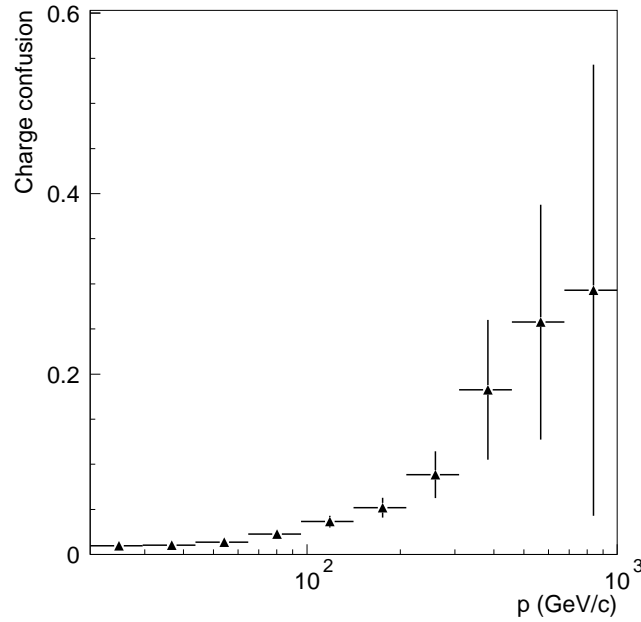
Fig. 7.19: Charge confusion coefficient, as obtained from the data, versus muon-chamber momentum for near vertical muon tracks.

the muons are produced at heights of about 10-20 km, the rate should be correlated with the pressure at this height. We have chosen a height of 11.5 km.[1] The mean atmospheric pressure at this height is about 200 mbar at a temperature of near -55° C. The atmospheric data have been obtained from the meteorological station near Geneva.[2] They were obtained around noon and midnight by means of balloon ascents. Therefore, the exact pressure and temperature during the time of data taking are not known and have to be approximated by the values near the reference times. In Fig. 7.20, the rate is plotted versus pressure at 11.5 km height. A slight anti-correlation, as expected, is seen between rate and pressure, $\Delta R/\Delta P = -2.7 \cdot 10^{-3} \pm 1.4 \cdot 10^{-3} \mathrm{s}^{-1}\mathrm{mbar}^{-1}$. The spread of the rate at given pressure indicates that other effects influencing the rate, besides the pressure, might exist.

7.9 Angular precision

In order to check the accuracy of the track angle reconstruction, we study the angular deflection of tracks generated at, and tracked back to, the surface layer. Note that the (forward) tracking is done by GEANT whereas the backtracking is done by GEANE. The angular deflection α is defined as

$$\alpha = \arccos(\sin\theta_1 \sin\theta_2 \cos(\phi_1 - \phi_2) + \cos\theta_1 \cos\theta_2), \qquad (7.13)$$

where θ_1 and ϕ_1 are the surface zenith and azimuth angles of the generated track and θ_2 and ϕ_2 are the surface zenith and azimuth angles of the reconstructed track. In Fig.

---

[1] Private communication T. Hebbeker
[2] Private communication P. LeCoultre
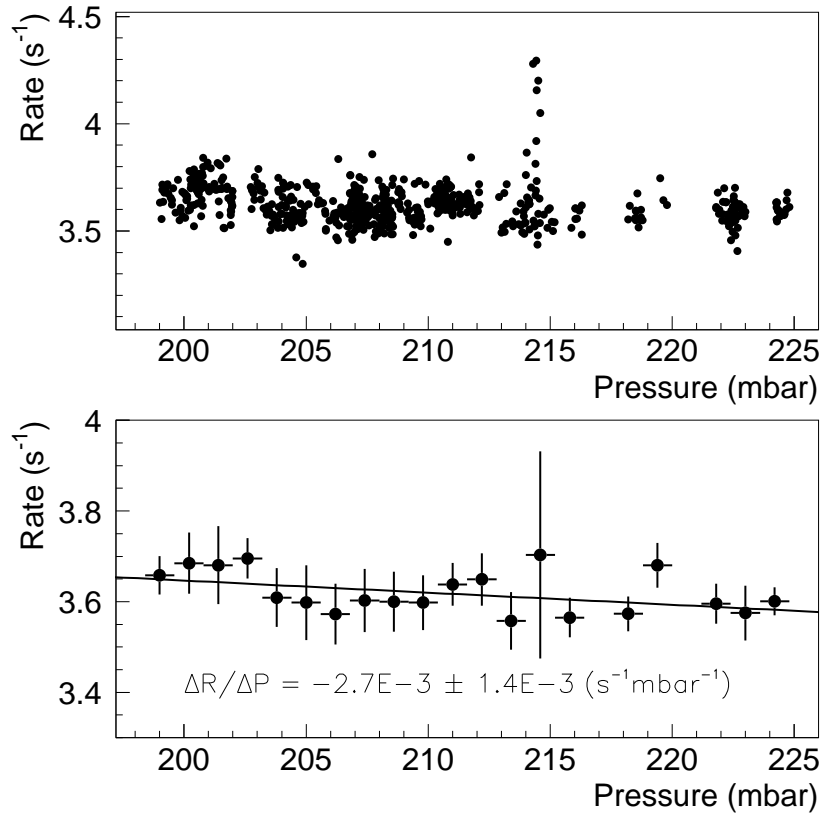
Fig. 7.20: Variation of cosmic-ray muon rate versus atmospheric pressure at 11.5 km height. The lower plot shows a linear fit of the mean rate versus pressure.

7.21 the distribution of the angular deflection in terms of $\cos \alpha$ is shown. The one-sigma value of the total angular deflection is about 2.1 degrees. Note that the scattering inside the molasse is included *twice* in the angular deflection.

7.10 Determination of live time

Besides the acceptance, the total live time is involved in the determination of the absolute muon flux. The live time is defined as the time span in which the experiment was capable of detecting and storing events. As time markers we use the standard L3 event time assigned to each event. The total time period of a run then equals:

$$\Delta T_{\mathrm{run}} = t_{\mathrm{last}} - t_{\mathrm{first}}, \tag{7.14}$$

where t_{last} and t_{first} are the event times of the last and first event of the run, respectively. If a number of N_{trig} events were triggered during the run, then the event rate was

$$R = N_{\mathrm{trig}}/\Delta T_{\mathrm{run}}. \tag{7.15}$$
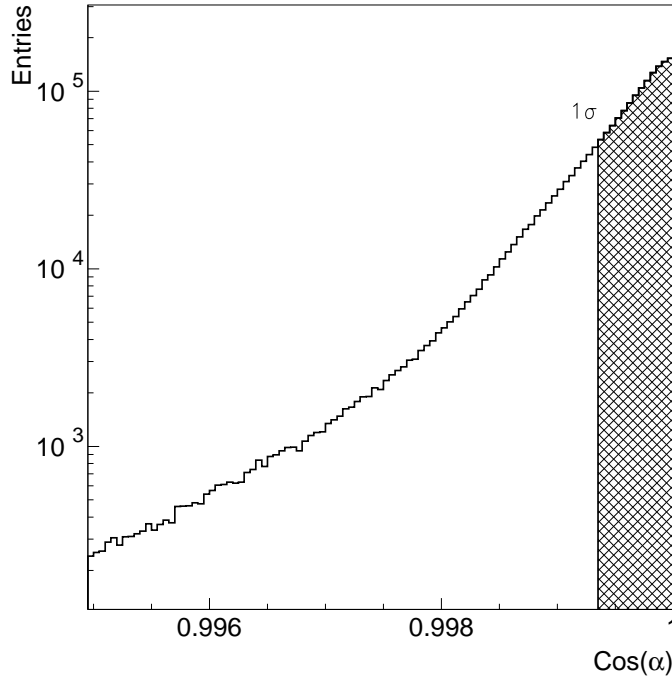
Fig. 7.21: Distribution of angular deflection for all selected cosmic-ray muon Monte Carlo events. Shown is the total deflection from generation at the surface to reconstruction at the surface, and its 1-sigma value.

The triggers are distributed in time according to a Poisson distribution. In the mean, it takes a time $\tau = 1/R$ from the start of the run, before a trigger occurs. Per cycle of the BGO clock source $\Delta T_{\mathrm{cycle}}$ a gate of length ΔT_{gate} was opened during which a cosmic-ray muon could be triggered. The maximum live time therefore equals

$$\tau + \Delta T_{\mathrm{run}} \cdot \Delta T_{\mathrm{gate}}/\Delta T_{\mathrm{cycle}}. \tag{7.16}$$

This live time has to be corrected for the dead time per trigger and for additional dead time $\Delta T_{\mathrm{trdead}}$. If a trigger occurs, the level-1 data taking electronics is dead for a time ΔT_{dead} due to digitization. The additional dead time contribution $\Delta T_{\mathrm{trdead}}$ comes from the fact that during a run the data taking might have been hampered. Since the mean time between two triggers is given by τ, we can argue that any time difference between two consecutive triggers much larger than τ (~ 0.3 sec.) is probably caused by malfunctioning hardware. We have set this criterium to a maximum time span of 10 sec. before it is treated as dead time. Investigation of the actual dead times show that either the dead time is compatible with the time in-between two triggers or the dead time is much larger than 10 seconds. From this we conclude that the 10 second limit is safe to use. The total live time per run now equals

$$\Delta T_{\mathrm{live}} = \tau + \Delta T_{\mathrm{run}} \cdot \Delta T_{\mathrm{gate}}/\Delta T_{\mathrm{cycle}} - N_{\mathrm{trig}} \cdot \Delta T_{\mathrm{dead}} - \Delta T_{\mathrm{trdead}} \tag{7.17}$$

Per run, the error on the total live time consists of the following contributions:

– The error from the first event being triggered during a run. This contributes a time τ.

– The error from hardware failures. This contributes a time 2τ per failure.
– The error from the last event being triggered during a run. This contributes a time τ.

For the total error on the live time per run, we therefore find

$$\Delta T^i_{\mathrm{err}} = 2 \cdot \tau \cdot (1 + N_{\mathrm{trdead}}).\tag{7.18}$$

The live time errors per run are all independent of each other. Therefore, the variance on the total live time T_{live} due to N runs equals

$$V(T_{\mathrm{live}}) = \sum_{i=1}^{N} (\Delta T^i_{\mathrm{err}})^2.\tag{7.19}$$

7.11 Momentum and angular binning

The binning in momentum depends on a compromise. The bin size should be such that the effects of the molasse shielding are still accurately accounted for. We have chosen 10 bins, logarithmically distributed in momentum between 20.0 and 1000.0 GeV/c. The log scale is chosen to reduce the effect of the steep momentum spectrum on the number of events inside a bin. The number of zenith bins is chosen to be 4, each having the same

Bin nr.	Momentum (GeV/c)	Zenith angle (Deg)	$\langle \cos \theta \rangle$
1	20.00-29.58	0.0-9.99	0.992
2	29.58-43.73	20.05-22.44	0.932
3	43.73-64.67	30.27-31.95	0.856
4	64.67-95.63	39.40-40.75	0.765
5	95.63-141.42		
6	141.42-209.13		
7	209.13-309.25		
8	309.25-457.30		
9	457.30-676.24		
10	676.24-1000.0		

Tab. 7.5. Momentum and angular binning used in this work. For the definition of the azimuth angle see Fig. 4.12.

width in $\cos \theta$. The number of azimuth bins is chosen to be 26, distributed evenly in ϕ. The binning in momentum and zenith angle is shown in Tab. 7.5. All references in the text to this binning refer to this table.

7.12 Spectrum deconvolution

Any muon track reaching the detector, is reconstructed and tracked back through the molasse up to the surface again. However, if we start out with a number of tracks at the surface with a given momentum p, the reconstructed momentum will be approximately Gaussian distributed around its initial value p, be it with a large momentum loss straggling tail. This means, the momentum is *smeared* around its original value. To obtain the original momentum distribution at the surface we need to *deconvolute* this momentum distribution.

Suppose we have events following a generated momentum distribution $\mathcal{F}(p)$. After reconstruction of the events we obtain a smeared distribution $\mathcal{G}(p)$. Suppose we bin both distributions into N bins in momentum. The events from a certain bin i of the distribution we start with, $\mathcal{F}(p)_i$, will be smeared over several bins in the distribution $\mathcal{G}(p)$, i.e. there is a bin-to-bin migration of events. The sum of the smeared bin contents in $\mathcal{G}(p)$, however, equals $\mathcal{F}(p)_i$ (conservation of number of events). We assume that the migrated bin contents stay inside the defined range of the original distribution, so we neglect any edge effects. For any momentum bin of $\mathcal{F}(p)$, we now can create a column of the matrix M which expresses the migration of the events. In this way we obtain the *smearing matrix* M defined by

$$\mathcal{G} = \mathsf{M}\mathcal{F}, \tag{7.20}$$

whose entries are normalized between 0 and 1. The deconvolution of the distribution $\mathcal{G}(p)$ is now simply a matter of inverting the matrix M. In this way we can obtain the deconvoluted momentum distribution at the surface as

$$\mathcal{F} = \mathsf{M}^{-1}\mathcal{G}. \tag{7.21}$$

The matrix inversion method however can be problematic. The matrix M can for instance be singular. This method is also known to be unstable and may yield unphysical results [85; 86].

A preferred method of deconvolution, used in this work, is the unfolding method based on Bayes theorem [87]. The Bayes theorem can be stated in terms of n_c independent causes $C_i, (i = 1, \cdots, n_c)$ and an effect E:

$$P(C_i|E) = \frac{P(E|C_i)P(C_i)}{\sum_{j=1}^{n_c} P(E|C_j)P(C_j)}. \tag{7.22}$$

Thus, the probability that an effect E has been due to cause C_i is proportional to the probability of the cause times the probability of the effect given the cause. The latter probabilities can be determined by means of the smearing matrix elements. The advantage of this method is that no matrix inversion is required, any bin-to-bin migration can be taken into account and the covariance matrix of the result is provided.

In practice, one starts with supplying an educated guess for the unfolded distribution. This distribution is folded and compared with the observed (folded) distribution. The ratio of the observed over the folded distribution is used to correct the initial-guess (unfolded) distribution. After a few iterations, a good agreement between the folded and observed distributions will be seen, which indicates that the (corrected) unfolded distribution approaches the real unfolded distribution.

A problem arises if the smearing of momentum extends outside the region in which $\mathcal{G}(p)$ is defined. The deconvolution will miss events such that the original distribution is not exactly reconstructed. This problem cannot easily be overcome. The only solution is to choose the interval from which the generated momenta are chosen large enough such that the region of interest in the reconstructed interval is well inside the range of effect of the generated interval. In our case the momenta are generated in the interval from 20 GeV/c up to 1 TeV/c. This means that the error in the reconstructed spectrum near 20 GeV/c and 1 TeV/c of momentum is relatively large due to this migration of events outside the defined interval.

The deconvolution matrix is obtained partly from the data and partly from the Monte Carlo. The momentum uncertainty consists of two parts: the smearing due to the finite

muon-chamber precision and the smearing due to variations in the momentum loss in the magnet and the molasse layer. The first part is obtained from the data whereas the second part is obtained from the Monte Carlo.

The smearing in the muon chambers is obtained from a momentum comparison of the upper and lower part of a data muon-track. At the point where the two track pieces are matched, the momenta should be the same in the mean. The momentum precision is obtained as follows: The momentum errors σ_1 and σ_2 on the upper and lower part of the track can be regarded equal. The error σ_t on the difference of the two momenta, $p_1 - p_2$, then equals:

$$\sigma_t = \sqrt{\sigma_1^2 + \sigma_2^2} \sim \sqrt{2}\,\sigma_1. \tag{7.23}$$

Since we select only events with an *upper* track present, that is being backtracked to the surface, we need the error on the momentum of the upper track. The momentum error on the upper part of the track equals

$$\sigma_1 = \frac{1}{2}\sqrt{2}\,\sigma_t. \tag{7.24}$$

This is the width of the distribution $\mathcal{S}_{\mathrm{MUCH}}$, representing the muon-chamber momentum precision.

The molasse smearing is obtained from the Monte Carlo by looking at the momentum gain obtained by the track while being backtracked through the molasse. One can argue that this is not the full story, since during backtracking only the *mean* momentum loss, without fluctuations, is taken into account. The real momentum loss distribution is likely to exhibit slightly larger tails than our approximation. In the mean, however, the distribution obtained here approximates that of the Monte Carlo well enough for our purpose, as long as the tails from momentum-loss straggling are not too large. The momentum loss in the molasse per track equals

$$p_{\mathrm{Mol}}^{\mathrm{loss}} = p_{\mathrm{surf}} - p_1, \tag{7.25}$$

where p_1 equals the momentum of the inward MUTK track and p_{surf} equals the momentum of the track at the surface. Repeating this measurement for a large number of tracks we find a molasse smearing distribution $\mathcal{S}_{\mathrm{Mol}}$.

The distributions representing the muon-chamber momentum precision, $\mathcal{S}_{\mathrm{MUCH}}$, and the molasse smearing, $\mathcal{S}_{\mathrm{Mol}}$, are finally convoluted to give the total smearing distribution:

$$\mathcal{S}_{\mathrm{surf}} = \mathcal{S}_{\mathrm{Mol}} * \mathcal{S}_{\mathrm{MUCH}}. \tag{7.26}$$

The distribution $\mathcal{S}_{\mathrm{surf}}$ then has to be shifted such that its mean corresponds to the mean momentum in the surface momentum bin being considered. The final distribution is filled into a column of the smearing matrix M, to be used by the deconvolution algorithm. Each column of the smearing matrix is normalized to 1.0. The shifted distribution is cut at the lower and upper bounds of the momentum range (20 GeV/c and 1 TeV/c, respectively). The cut regions have no physical significance in our case, since the deconvolution is *only* defined within the momentum region stated above.

In Fig. 7.22, the momentum smearing distributions are shown for four different bins in surface momentum as indicated. The upper plot shows the distribution of $\mathcal{S}_{\mathrm{MUCH}}$ while the lower plot shows the distribution of $\mathcal{S}_{\mathrm{Mol}}$. Note that the distributions $\mathcal{S}_{\mathrm{Mol}}$ have been shifted in momentum such that the mean of the distribution coincides with the mean surface momentum in the bin. At low momenta the muon chamber smearing dominates.

For larger momenta, the relative contribution from the molasse smearing to the total smearing increases.
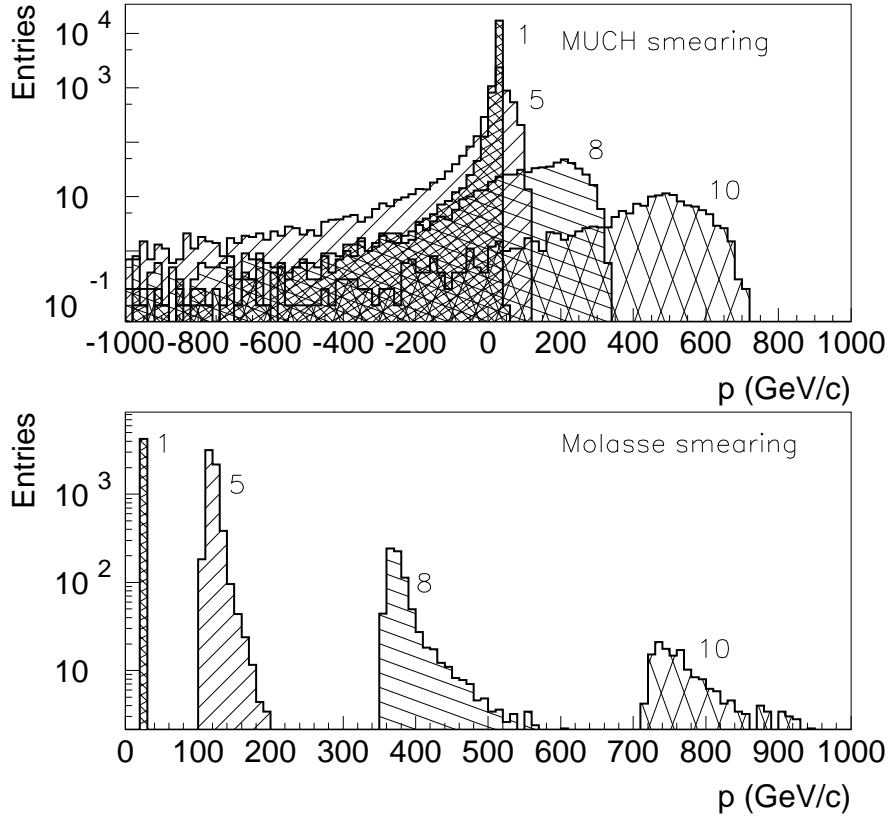
Fig. 7.22: Momentum smearing for 4 different bins in surface momentum. The upper plot shows the momentum smearing in the muon chambers. The lower plot shows the momentum smearing in the molasse. The surface momentum bins are indicated by the numbers (see Sec. 7.11).

7.13 Event selection efficiency correction

The event selection criteria are the same for data as for Monte Carlo. In order to be able to correct the data with the Monte Carlo effective geometrical acceptance, the selection efficiencies for the data and Monte Carlo samples should be the same, with respect to the *soft-triggered* sample. The soft-triggered sample is the raw sample that has been passed through the software trigger-simulation cuts (Sec. 7.3). As can be seen from Fig. 7.7, there is good agreement between both efficiencies. The small differences in efficiencies however, cause systematic shifts in the data spectra. In order to correct for this difference, the effective geometrical acceptance and its error are corrected (per angular bin) according to

$$\mathcal{A}' = \mathcal{A}\, \frac{\varepsilon_{\mathrm{data}}}{\varepsilon_{\mathrm{Mc}}}, \tag{7.27}$$

$$\sigma(\mathcal{A}') = \sigma(\mathcal{A}) \, \frac{\varepsilon_{\text{data}}}{\varepsilon_{\text{Mc}}}, \tag{7.28}$$

where $\varepsilon_{\text{data}}$ and ε_{Mc} are the selection efficiencies for the soft-triggered data and Monte Carlo sample, respectively.

7.14 Calculation of spectrum

The cosmic-ray muon flux is normalized as follows. Per angular bin, we have an estimate of the geometrical acceptance $\mathcal{A}$ in that bin and of the deconvoluted number of entries N_{deco}, each with their respective variance. The number of entries per angular bin, corrected for the acceptance $\mathcal{A}'$, equals

$$S_\mu(i, j) = \frac{N_{\text{deco}}(i, j)}{\mathcal{A}'(i, j)}, \tag{7.29}$$

where i and j denote the zenith and azimuth angular bin, respectively, and $\mathcal{A}'$ is the acceptance corrected for the difference in data and Monte Carlo selection efficiencies (Sec. 7.13). In theory, neglecting any minor variation of the sea-level flux versus azimuth, the flux $S_\mu(i, j)$ should be the same for each azimuth bin j. The flux for zenith angle bin i then equals the weighted flux averaged over the azimuth bins:

$$\bar{S}_\mu(i) = \frac{1}{w(i)} \sum_j w(i, j) S_\mu(i, j), \tag{7.30}$$

where

$$w(i) = \sum_j w(i, j) \tag{7.31}$$

and the weights $w(i, j)$ equal

$$w(i, j) = 1/\sigma_{ij}^2, \tag{7.32}$$

with σ_{ij} the error on $S_\mu(i, j)$. The flux $\bar{S}_\mu$ now has to be corrected for the total live time T_{live}, the width of the momentum bin Δp and the event selection efficiency ε to give the differential muon flux at the surface. The event selection efficiency ε varies from run to run. In order to take this variation into account, the expression for the live time per run, ΔT_{live}, has been modified from Eq. (7.17) to

$$\Delta T'_{\text{live}} = \Delta T_{\text{live}} \, \varepsilon_{\text{run}}, \tag{7.33}$$

where ε_{run} is the event selection efficiency averaged over one run. The equation for the flux thus becomes

$$D_\mu(i) = \frac{\bar{S}_\mu(i)}{\Delta p \, T'_{\text{live}}}, \tag{7.34}$$

where

$$T'_{\text{live}} = \sum_{i=1}^{N} \Delta T'_{\text{live}}. \tag{7.35}$$

In fact, this grants the flux estimate for a certain zenith angular bin with a mean $\cos\theta$ as specified in Tab. 7.11. To measure the real vertical spectrum at $\cos\theta = 1.0$, we need to correct the measurements according to

$$D_\mu(i, \theta = 0) \equiv D_\mu(i, \theta) \cdot \frac{\mathrm{d}N_\mu/\mathrm{d}\cos\theta|_{\theta=0}}{\mathrm{d}N_\mu/\mathrm{d}\cos\theta|_\theta} = D_\mu(i, \theta) \cdot C(p, \theta). \tag{7.36}$$

The dependence $\mathrm{d}N_\mu/\mathrm{d}\cos\theta$ has been parameterized as [88]

$$\mathrm{d}N_\mu/\mathrm{d}\cos\theta = 1 + a(p)(1 - \cos\theta), \tag{7.37}$$

$$a(p) = -1.903 + 0.1434 \ln p + 0.0145 \ln^2 p, \tag{7.38}$$

where p is measured in GeV/c. The correction factor $C(p, \theta)$, for a bin with a mean zenith angle $\langle\cos\theta\rangle$, thus equals

$$C(p, \theta) = \frac{1}{1 + a(p)(1 - \langle\cos\theta\rangle)}. \tag{7.39}$$

It turns out that the correction factor for the near vertical zenith angle bin deviates by about 1 percent from 1.0. It is difficult to determine the systematic error induced by the uncertainty on this correction factor. For these reasons, the correction to the near vertical flux is *not* applied. Instead, we increase the systematic error on the vertical flux by 1%.

7.15 Calculation of charge ratio

From the deconvolution process described in Sec. 7.12, we obtain two separate deconvoluted momentum spectra, one for the positive-charged tracks and one for the negative-charged tracks, $\mathcal{F}^+(p)$ and $\mathcal{F}^-(p)$. The charge ratio is simply obtained by dividing both spectra,

$$R_\mu(i, j) = \frac{\mathcal{F}^+(i, j)}{\mathcal{F}^-(i, j)}, \tag{7.40}$$

where the indices i and j denote the zenith and azimuth angular bin, respectively. Here, it is assumed that the acceptance $\mathcal{A}$ does not depend on the charge of the muon. This charge ratio has to be corrected for the charge confusion, using Eq. (7.12). The final true charge ratio is obtained versus zenith angle by taking a weighted mean over the azimuth bins (since again we neglect any minor azimuth dependence):

$$\bar{R}_\mu(i) = \frac{1}{w(i)} \sum_j w(i, j) R_\mu(i, j), \tag{7.41}$$

where

$$w(i) = \sum_j w(i, j) \tag{7.42}$$

and the weights $w(i, j)$ equal

$$w(i, j) = 1/\sigma_{ij}^2, \tag{7.43}$$

with σ_{ij} the error on $R_\mu(i, j)$.

7.16 Error calculation

The measurement of the muon momentum spectrum and charge ratio have statistical as well as systematic errors. In the next sections I will derive the errors on the various quantities.

7.16.1 Statistical errors

Scaling of statistical errors. The statistical errors for the charge confusion, the charge ratio and the momentum spectrum are calculated at first instance according to the rules of error propagation. All these three variables are measured for several different bins in azimuth for a specific zenith angular bin. In order that the calculated total error on the mean of the variable, taken over all azimuth bins, represents at least the real variation of the variable, we apply a scaling of the errors according to the following scheme [52].

The weighted mean of a variable x over all azimuth bins N (where $x > 0$) is determined:

$$\bar{x} = \frac{\sum_{i=1}^{N} w_i x_i}{\sum_{i=1}^{N} w_i}, \qquad (7.44)$$

$$w_i = 1/\sigma_i^2, \qquad (7.45)$$

where σ_i is the statistical error on x_i. Next, we determine the χ^2 of the measurement:

$$\chi^2 = \sum_{i=1}^{N} w_i (\bar{x} - x_i)^2. \qquad (7.46)$$

For a number of degrees of freedom $DoF = N - 1$, the χ^2/DoF is determined. If the value of $\chi^2/DoF > 1.0$ but *not much* larger than 1.0, then the total statistical error $\sigma_{\bar{x}}^2 = 1/\sum_{i=1}^{N} w_i$ is multiplied by χ^2/DoF.

The flux, the charge ratio and the charge confusion show a *systematic* variation versus the azimuth angle (Fig. 7.23). This variation is likely due to a difference between the simulated detector efficiency and the real efficiency. Therefore, this systematic variation is thought to be independent of other systematic errors. The scaling of the statistical error by the above procedure produces an error that is partly statistical and partly systematic. In scaling the statistical error without taking into account the *total* systematic error on the measurement (but just the statistical error of the individual measurements), we overestimate the total error. Since the scaling factor is not too much different from 1.0, we accept this small error.

Charge confusion. According to Eq. 7.9, the variance on the charge confusion can be written as

$$V(C) = \left(\frac{\partial C}{\partial T}\right)^2 V(T) = \frac{1}{1 - 2T} V(T), \qquad (7.47)$$

where

$$V(T) = \frac{T}{N_{\mathrm{real}}}. \qquad (7.48)$$

The variance on the charge confusion thus equals

$$V(C) = \frac{T}{1 - 2T} \frac{1}{N_{\mathrm{real}}}. \qquad (7.49)$$
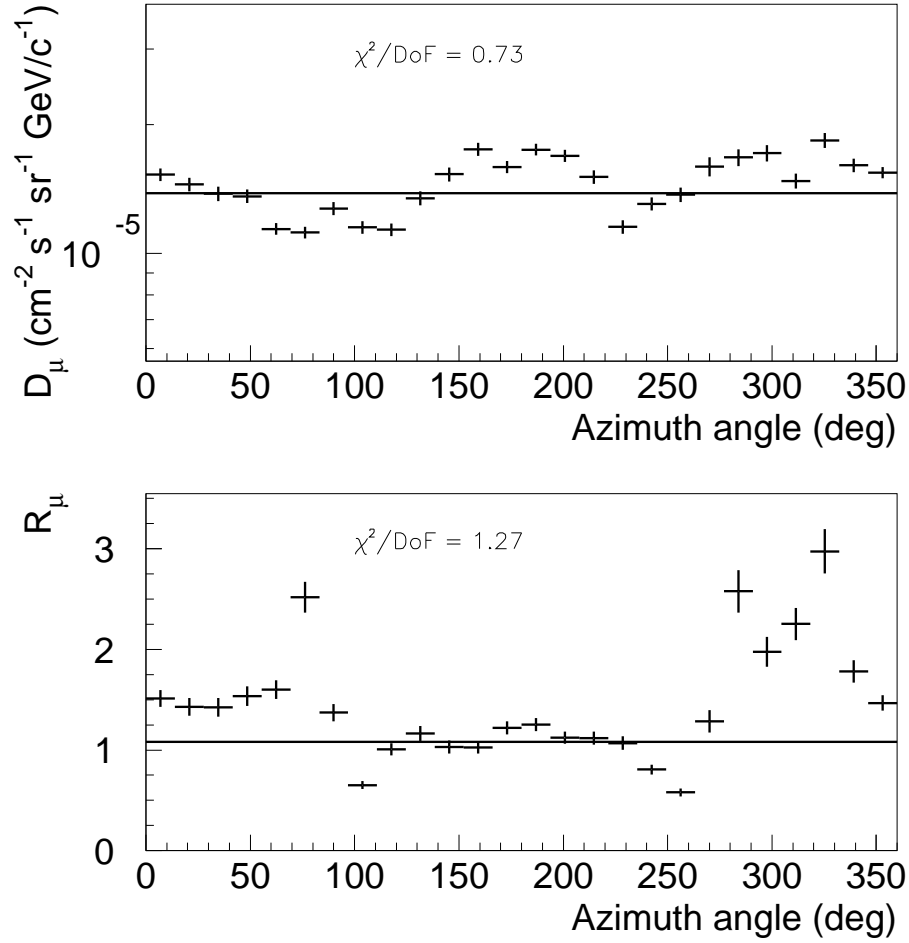
Fig. 7.23: Variation of differential flux and charge ratio versus azimuth angle for momentum bin 1 and zenith bin 2. The mean of either distribution is indicated by the line.

Charge ratio. The measurement of the charge ratio is in fact a measurement of a Bernouilli process. We measure the charge $N = N^+ + N^-$ times, where each measurement either gives a positive or a negative charge outcome. The chance of finding a positive charge is $p^+ = N^+/N$, whereas the chance of finding a negative charge is $1 - p^+ = p^- = N^-/N$. The variance on the measurement of the mean number of positive or negative charges N^+ or N^- is, therefore, $V = Np^+p^-$. The variance on the charge ratio is found from

$$V(R) = \left(\frac{\partial R}{\partial N^+}\right)^2 V(N^+), \qquad (7.50)$$

where $V(R)$ denotes the variance on $R = N^+/(N - N^+)$. Here, $V(N^+) = Np^+p^- = \frac{NR}{(1+R)^2}$. Thus, we find for the variance on the charge ratio

$$V(R) = \frac{R(1+R)^2}{N}. \tag{7.51}$$

In Fig. 7.24 the relative error $\sigma(R_\mu(i))/R_\mu(i)$ is shown for the four zenith angular bins. The results are integrated over azimuth.

Momentum spectrum. The muon momentum spectrum is defined by Eq. (7.34). The statistical variance reads

$$V(D_\mu(i)) = \left(\frac{\partial D_\mu(i)}{\partial \bar{S}_\mu(i)}\right)^2 V(\bar{S}_\mu(i)) + \left(\frac{\partial D_\mu(i)}{\partial T_{\text{live}}}\right)^2 V(T_{\text{live}}), \tag{7.52}$$

or

$$V(D_\mu(i)) = \left(\frac{D_\mu(i)}{\bar{S}_\mu(i)}\right)^2 V(\bar{S}_\mu(i)) + \left(\frac{D_\mu(i)}{T_{\text{live}}}\right)^2 V(T_{\text{live}}). \tag{7.53}$$

In Fig. 7.24 the relative error $\sigma(D_\mu(i))/D_\mu(i)$ is shown for the four zenith angular bins. The results are integrated over azimuth. The error on D_μ is dominated by the error on $S_\mu(i)$. The live-time error does not contribute significantly (relative error contribution $\sigma(T_{\text{live}})/T_{\text{live}} = 0.15 \cdot 10^{-3}$). In Fig. 7.25, the relative error $\sigma(\mathcal{A})/\mathcal{A}$ is shown for four different bins in zenith and azimuth angles. The errors are calculated according to Eq. (6.10).

7.16.2 Systematic errors

The systematic errors involved in the determination of the muon momentum spectrum can be divided into the following classes.

○ Trigger efficiency. As stated earlier, the trigger conditions were not well recorded during the cosmic-ray muon BGO calibration runs. As a result, the normalization of the flux contains an overall systematic error. As an estimate of the systematic error involved, the mean trigger rate can be recorded over long time periods, see Sec. 7.4. From this, we find a systematic error of 1.5% on the trigger rate or, equivalently, on the muon flux. This error is due to variations in the trigger setup and/or detector setup and variations in atmospheric pressure and temperature. The trigger efficiency has no influence on the charge ratio, assuming the trigger efficiency is independent of the track charge.

○ Selection cuts. The flux and the charge ratio are both affected by the value of the selection cuts. To estimate their effect, the flux and the charge ratio are determined with the standard selection cuts described above and with slightly adapted selection cuts, namely
  – Cut on number of raw P hits: 800 → 600,
  – Cut on number of raw Z hits: 400 → 300,
  – Cut on (1-r) of track matching: 0.01 → 0.1,
  – Cut on χ^2 of swimfit: 0.001 → 0.01.
  The main contribution to this systematic error comes from the variation of the cut on the track matching (1-r). It amounts to about 10% for the flux, in the entire momentum range, and from about 1 to 30% for the charge ratio, for energies from 20 to 1000 GeV, respectively.
  The systematic variation of the flux and the charge ratio due to the *simultaneous* change of the selection cuts is shown in Fig. 7.26. The error on the systematic error
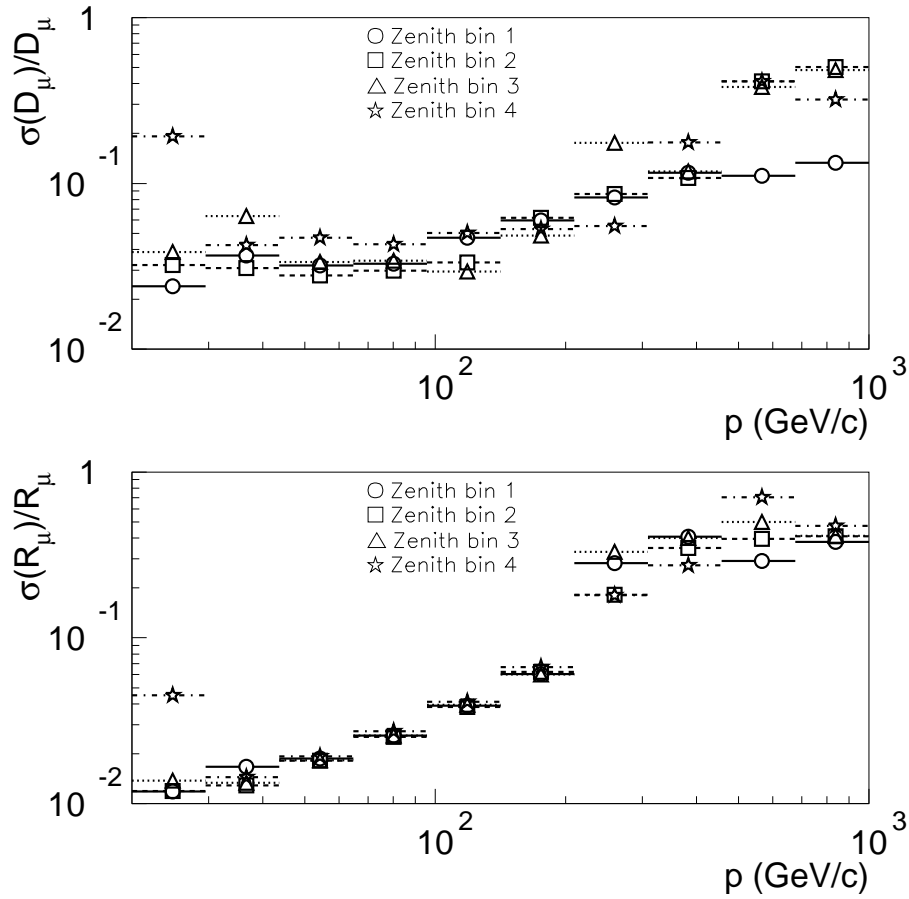
Fig. 7.24: Relative statistical error $\sigma(D_\mu(i))/D_\mu(i)$ (top) and $\sigma(R_\mu(i))/R_\mu(i)$ (bottom) versus momentum for the four zenith angular bins. Horizontal bars indicate bin width.

is not taken into account. Therefore, we are conservative and assign an *upper limit* to the systematic errors. The upper limits are shown in the figures. The error on the differential flux is approximately constant versus momentum whereas the error on the charge ratio increases versus momentum.

○ Deconvolution accuracy. The deconvolution process induces a momentum dependent systematic error on the deconvoluted spectrum. The systematic uncertainty of the flux due to the deconvolution process can be read off from the ratio of the observed spectrum over the smeared spectrum. Ideally, this ratio is equal to 1.0. In reality it deviates from 1.0 since the algorithm is not able to find a perfect match between the observed and the smeared spectrum. The main reason for this discrepancy is that the information about events which are smeared *outside* of the range of the matrix is missing. We determine the systematic error in the following way. For a certain zenith angle bin we check the ratios of observed over smeared spectra for all azimuth bins. From these values, we extract the RMS variation of this ratio versus momentum. This is repeated for all zenith angle bins. Assuming that the deconvolution is independent of the zenith angle, we finally determine the mean variation over all zenith angle bins. In
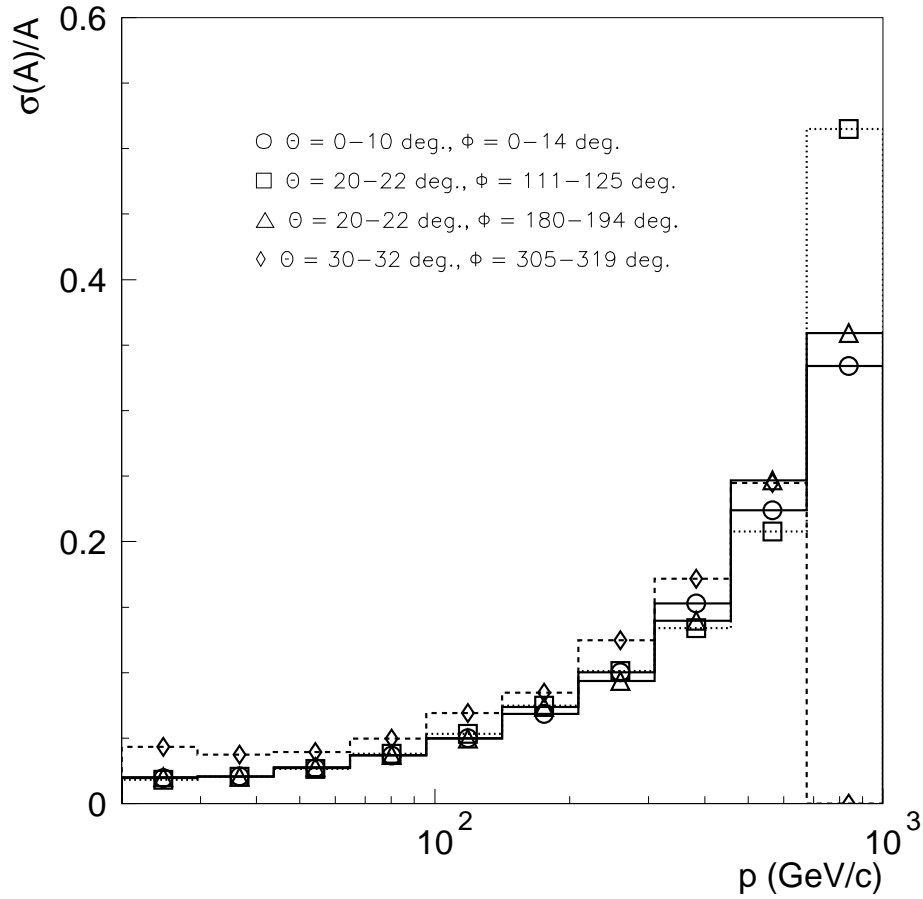
Fig. 7.25: Relative statistical error $\sigma(\mathcal{A})/\mathcal{A}$ versus momentum. Results are shown for four different bins in zenith and azimuth angles. Horizontal bars indicate bin width.

Fig. 7.27 the relative error is shown versus momentum, for the four zenith angle bins in the top plot and the resulting mean error in the bottom plot. The error behaves as expected. Due to the upper and lower cutoff of the Monte Carlo momentum spectrum the deconvolution error increases for low and higher momenta, relative to the error near 50 GeV/c where the smallest error is obtained. The charge ratio is relatively independent of the momentum. Therefore, to first order, we expect that the spectra of positive muons and of negative muons before deconvolution are the same up to a constant factor. Any variation in the deconvolution procedure has only minor effects on the charge ratio, determined by Eq.(7.40), since the effect on the spectra of both charge signs is about the same. For this reason, we do not assign a systematic error from the deconvolution procedure to the charge ratio.

Furthermore, the measured flux has to be corrected for the systematic effects listed below.

❍ Scintillator barrel efficiency. The efficiency of the barrel scintillator system during the cosmic runs is not known. It is taken from [70], where it is estimated to be 99.5% (90% confidence interval) for a dimuon event sample. The trigger criterium for these
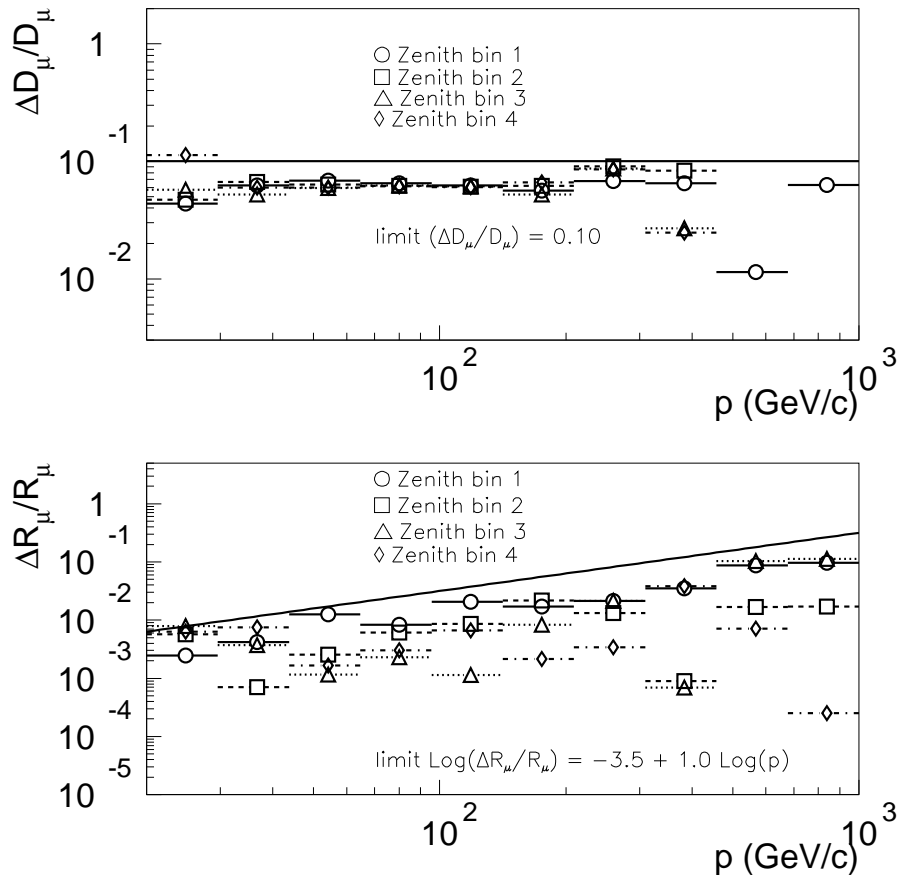
Fig. 7.26: Systematic error on spectrum (top) and charge ratio (bottom) due to change of selection cuts. Horizontal bars indicate bin width. The lines are upper-limits of the contribution to the systematic error due to the selection cuts.

events was that two counters should be hit within ± 3 ns of the beam crossing. This factor corrects the muon flux in an upward direction by 0.5%.

◯ Multi-muon flux contribution. Since we apply a cut on the track multiplicity in an event equal to one, the multi-muon contribution to the flux is neglected. The number of events with more than one track is estimated to be 1%, from comparison of the number of multi-muon events relative to single muon events (see Tab. 7.3). This factor corrects the muon flux in an upward direction by slightly more than 2%. We have used a correction of 2%.

◯ Conversion to sea-level flux. The sea-level flux is lower than the flux at L3 ground level. From [67] we estimate the total effect on the normalization of the flux to be at most 1-2%. This correction is *not* applied to the present data since the exact magnitude of the correction is not known. Thus, all measurements of the flux and charge ratio are for the L3 altitude.
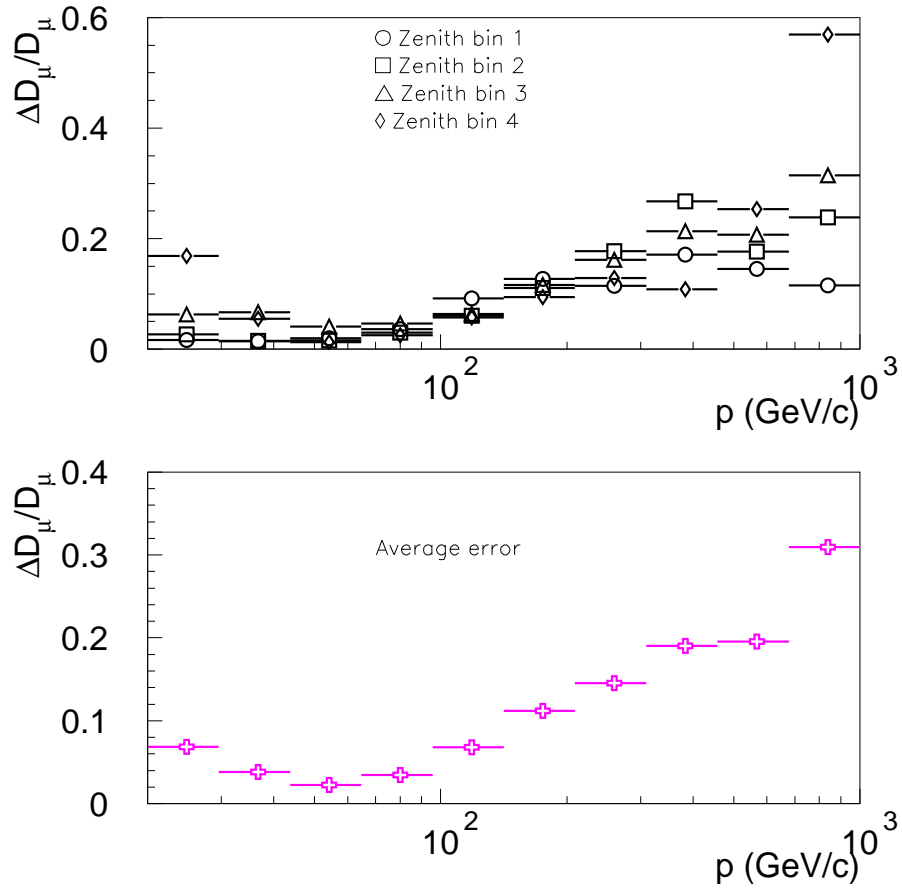
Fig. 7.27: Systematic error per zenith angle bin (top) and averaged (bottom) due to the deconvolution procedure. Horizontal bars indicate bin width.

7.17 Results

The differential spectra D_μ and $p^3 D_\mu$ as measured according to Eq. (7.34) are presented in Fig. 7.28 and 7.29, together with results from other experiments and the spectrum as expected by theory, Eq. (3.1). For numerical values of the flux and its errors we refer to the tables in App. D.

The charge ratio R_μ as measured according to Eq. (7.41) is presented in Fig. 7.30 and 7.31, together with results from other experiments and the charge ratio according to three theoretical models. For numerical values of the charge ratio and its errors we refer to the tables in App. D.
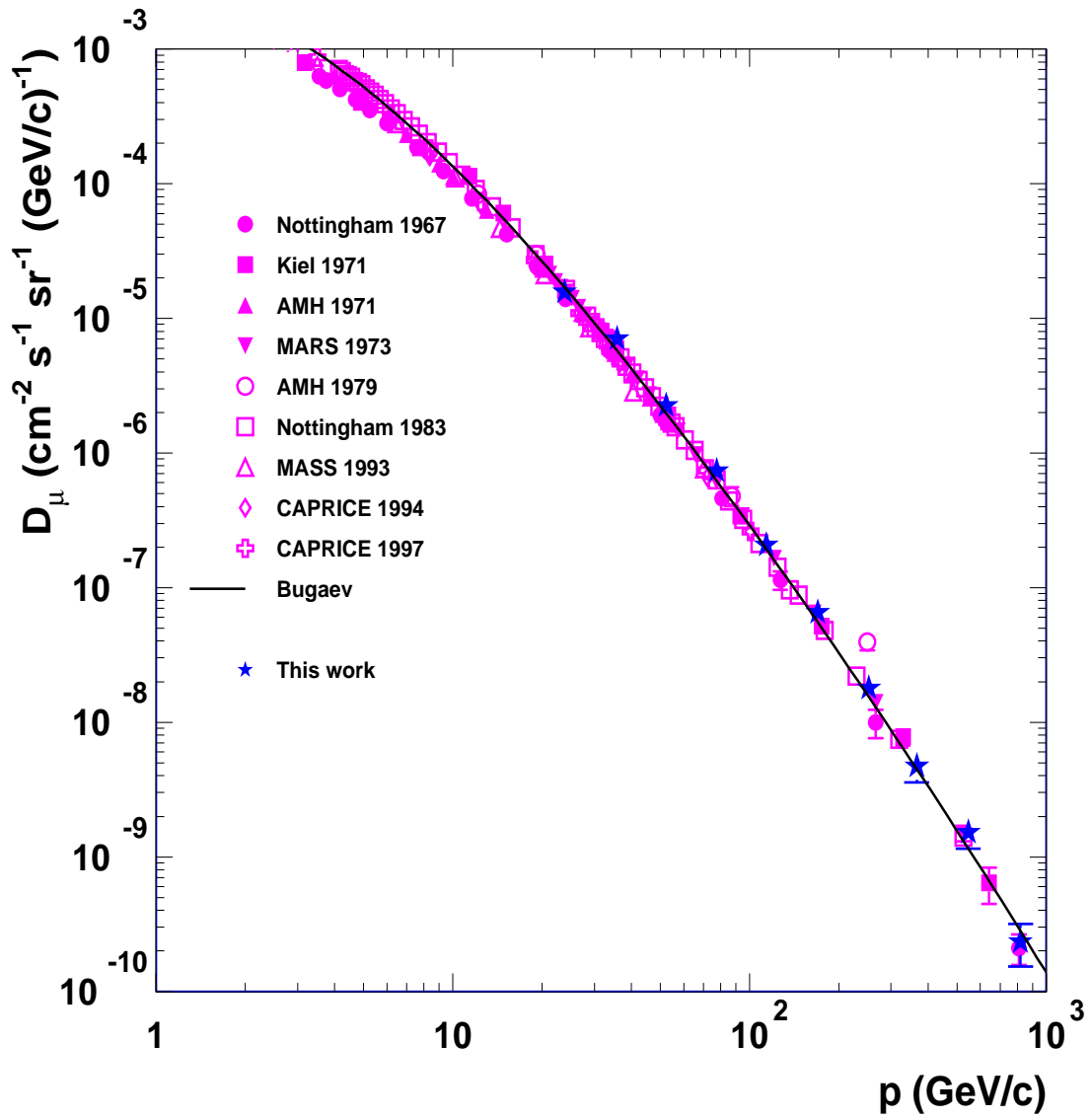
Fig. 7.28: Vertical differential muon spectrum. The results of this work apply to an altitude of 449 m above sea level, whereas the results of other experiments and theory apply to sealevel. Total errors (statistical + systematic) are shown. The data are from [38; 39; 40; 41; 42; 43; 44; 45]
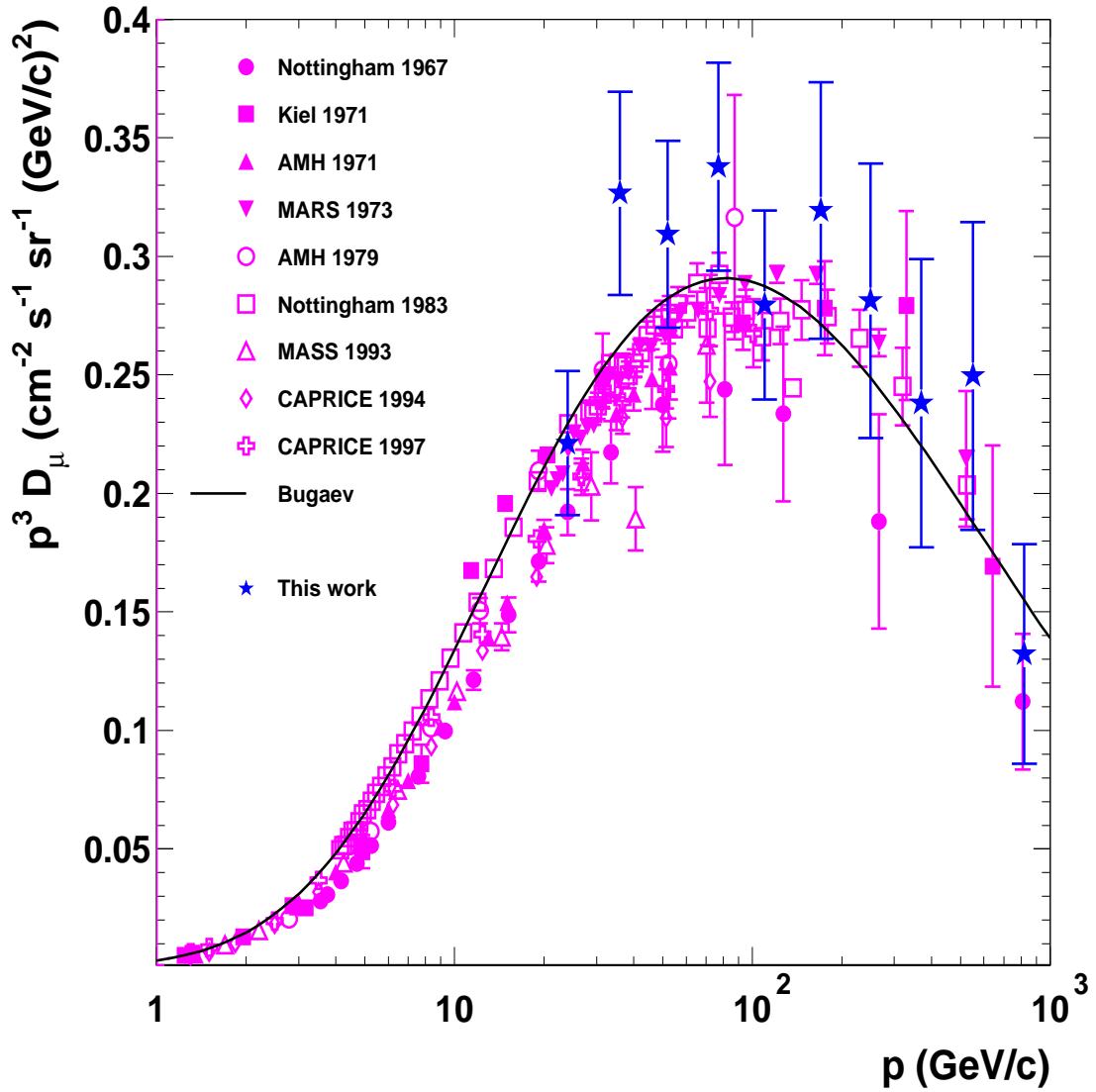
Fig. 7.29: Vertical differential muon spectrum. The results of this work apply to an altitude of 449 m above sea level, whereas the results of other experiments and theory apply to sealevel. The spectra are multiplied by p^3. Total errors (statistical + systematic) are shown. The data are from [38; 39; 40; 41; 42; 43; 44; 45]
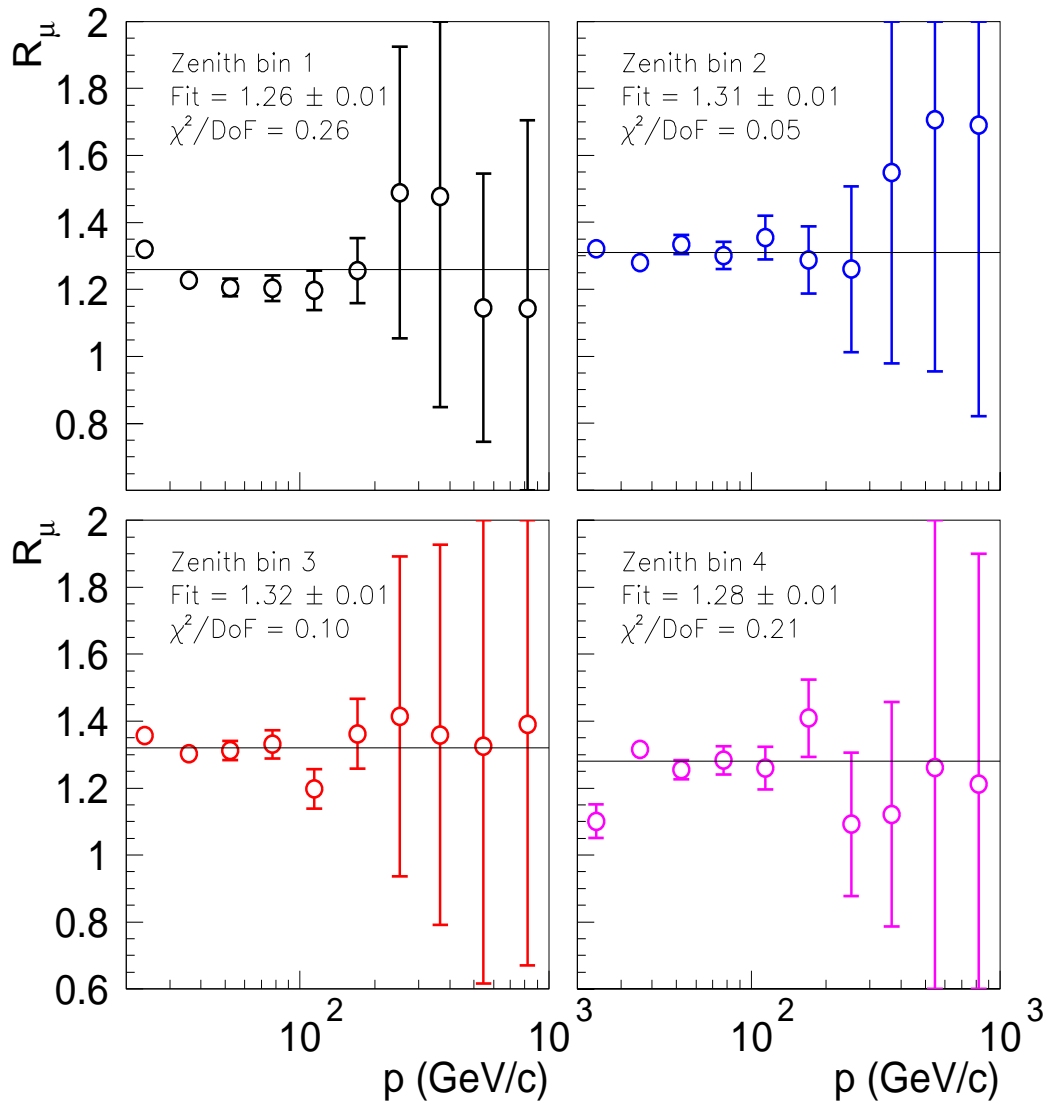
Fig. 7.30: Inclined corrected charge ratio. The results apply to an altitude of 449 m above sea level. Total errors (statistical + systematic) are shown.
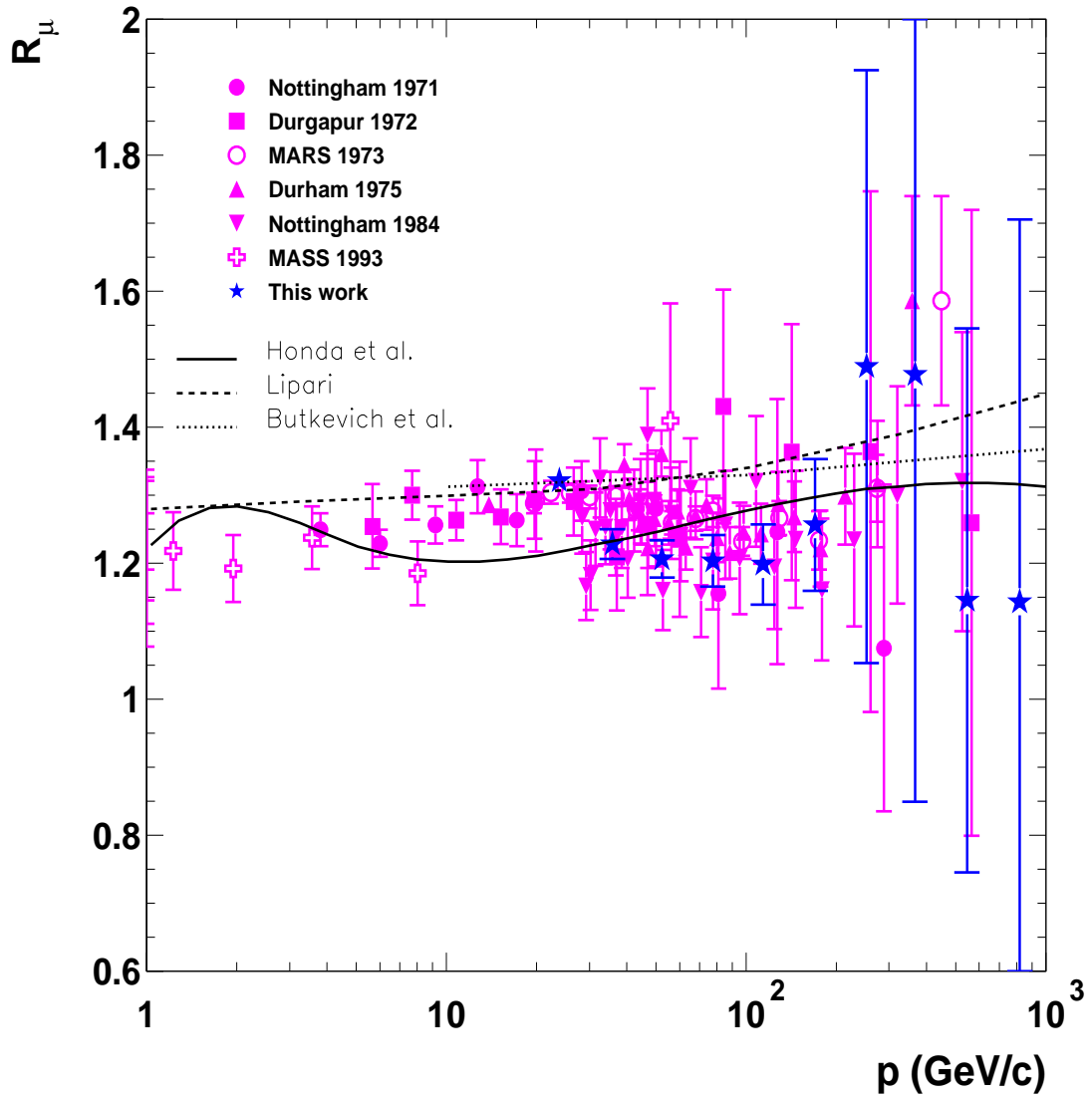
Fig. 7.31: Vertical corrected charge ratio. The results of this work apply to an altitude of 449 m above sea level, whereas the results of other experiments and theory apply to sea level, except the MASS results which are recorded at 600 m above sea level. Total errors (statistical + systematic) are shown. The data are from [47; 48; 49; 50; 44]

Chapter 8

Discussion

In this chapter the results obtained for the differential spectrum and the charge ratio are discussed. Taking into account these results, the feasibility of the L3+Cosmics experiment is discussed.

8.1 Differential spectrum

Our result on the differential spectrum, Fig. 7.28 and 7.29, shows that the total uncertainty on the flux varies from about 14% near 100 GeV/c to about 29% near 1000 GeV/c. The largest contribution to the uncertainty comes from the deconvolution procedure. Our data are in reasonable agreement with the results of other experiments and slightly higher than predicted by Bugaev [37].

In order to estimate the difference on the absolute normalization between our data and theory, we fit the Bugaev parameterization, Eq. (3.1), to our data. The normalization is fitted by a multiplicative factor in front of the flux (which equals 1.0 for the standard normalization). The result of the fit is shown in Fig. 8.1 (Bugaev, fitted normalization), together with the standard normalization (Bugaev, fixed normalization). The one sigma error on the fitted factor is indicated by the hatched region. The fit can be interpreted as an indication that the cosmic-ray muon flux is underestimated, taking the error into account. However, the fitted result is compatible with theory.

8.2 Charge ratio

Our result on the charge ratio R_μ, Fig. 7.30 and 7.31, shows that its value is quite stable versus momentum. Only the vertical charge ratio shows a slight dependence on momentum. The total error on the ratio (above 100 GeV/c) increases rapidly as a function
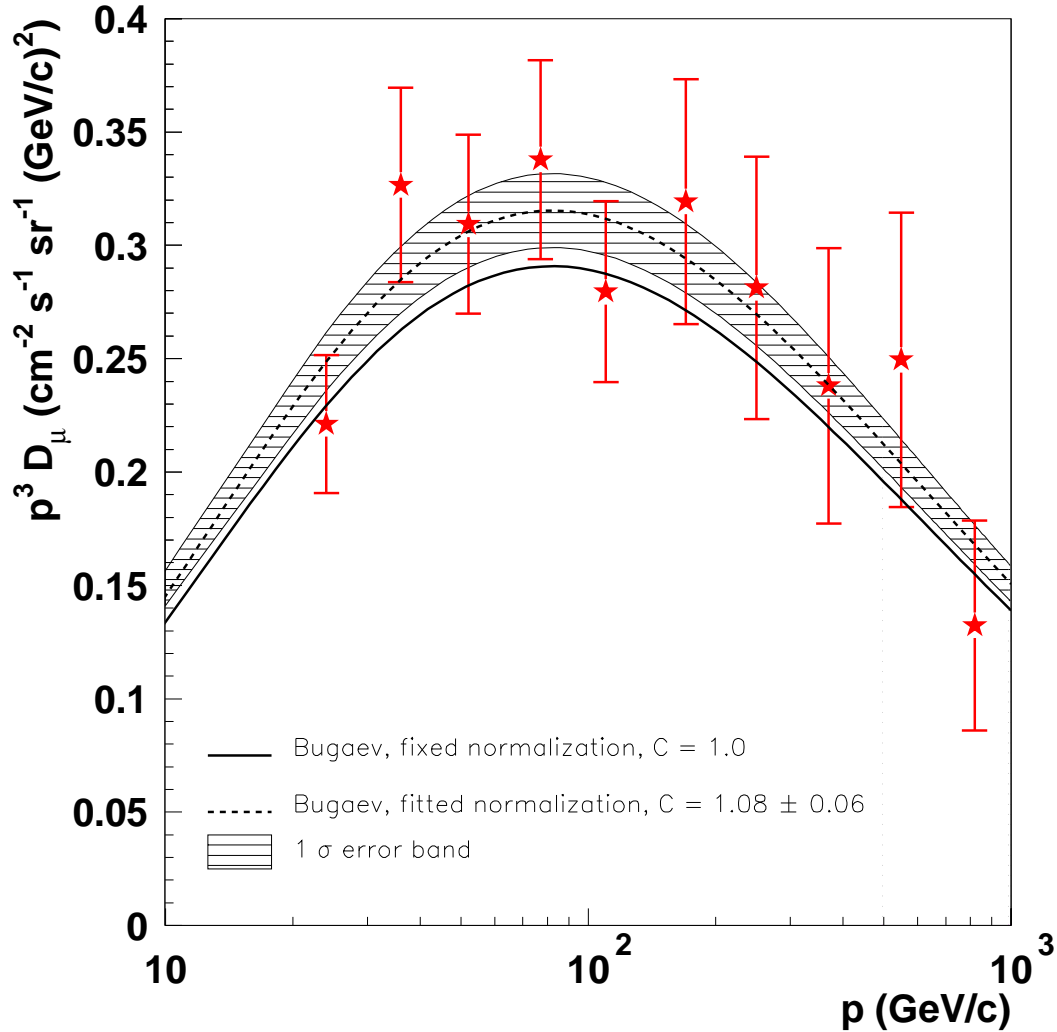
Fig. 8.1: The vertical differential muon spectrum as obtained in this work, including a fit of the Bugaev prediction. The hatched region shows the 1 σ error on the fitted normalization.

of momentum. This is mainly due to the increase of the statistical error. The systematic error on the ratio, determined by changing the selection cuts, increases as a function of momentum and is equal in magnitude to the statistical error for the highest momenta. The charge ratio does not show a strong dependence on the zenith angle. The mean value, as indicated by the fitted horizontal line, varies from 1.26 to 1.32. Our results are in agreement with the results of other experiments and, above 30 GeV/c, are reproduced best by the Honda theory (Fig. 8.2).
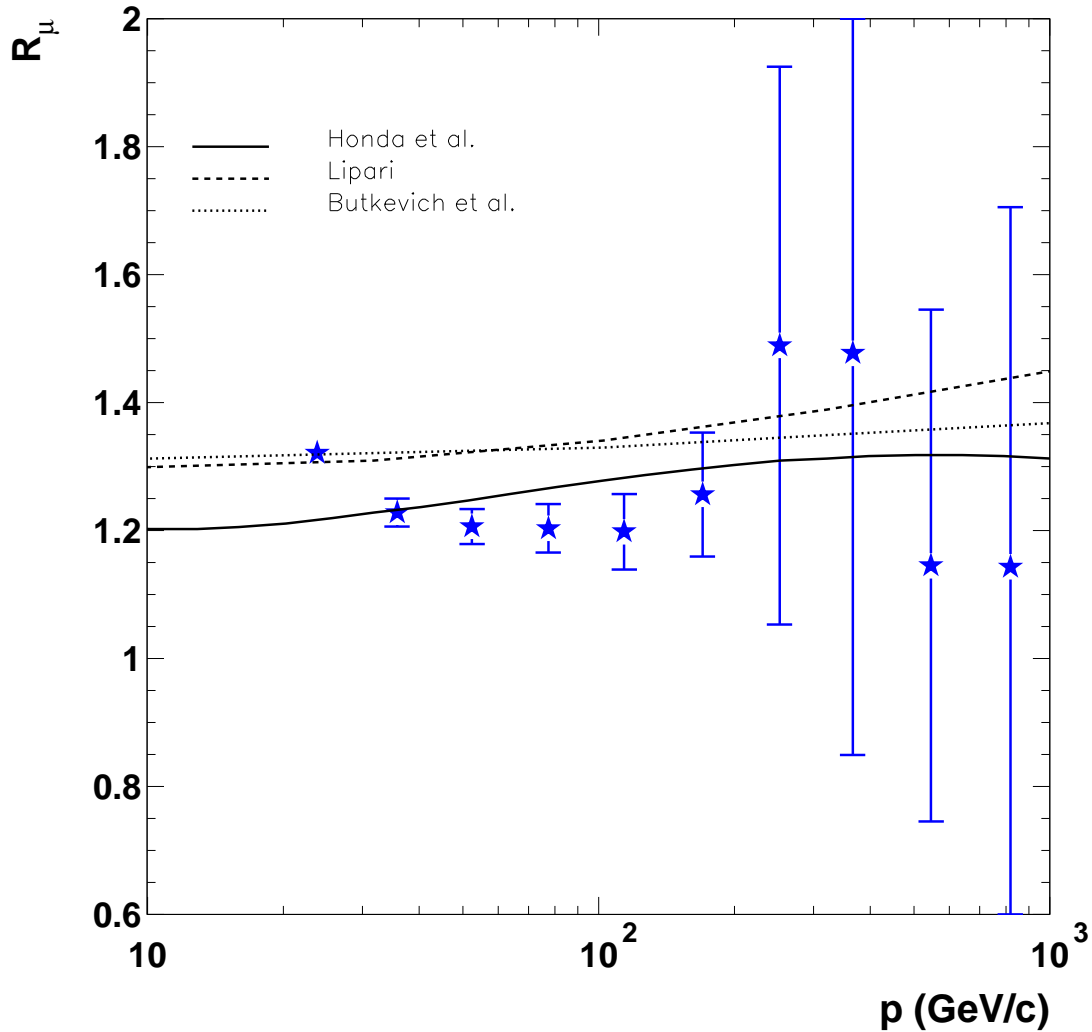
Fig. 8.2: The vertical charge ratio as obtained in this work, including theoretical predictions.

8.3 Feasibility of L3+Cosmics

The geometrical acceptance of the L3+Cosmics setup is far larger than that for the 1991 detector setup, using the barrel scintillator. The precision of time measurement is comparable to the precision with which the time of passage was measured by the scintillator barrel. The basic detector setup, the halls and the principle of measurement of the muon momentum did not change versus the 1991 data. Therefore, the 1991 data analysis is a good representation of the feasibility of the L3+Cosmics project [89; 90]. The most important results of the underlying analysis are:

– The cosmic-ray muon data can be reconstructed with a momentum precision reasonably close to that of dimuon tracks (at 45 GeV/c). Due to the different angular distribution in the muon chambers, the precision is slightly less than obtained for dimuon tracks.
– The geometrical acceptance can be calculated accurately, provided that the number of simulated events is large enough to scale down the Monte Carlo statistical error.
– The systematic effects are understood well, taking into account that these data were originally taken for calibration purposes only. A dedicated experiment is of course able to obtain smaller and more precise error estimates than obtained in this work.
– The cosmic-ray muon spectrum and the charge ratio can be calculated to good precision, provided the statistics is large enough and systematic effects are well understood.

The main objective of the L3+Cosmics experiment, a precise measurement of the cosmic-ray muon spectrum up to a few TeV/c of momentum, is feasible, considering the results of this work.

T0 calibration method

The method used to calibrate the T0 offset and the drift velocity is described.

To calibrate the global T0 offset and the drift velocity in the muon chambers, tracks that cross a sense or mesh plane are used. The drift velocity v_d and the global T0 offset t_0 are closely related to each other through the hit coordinates inside a P-cell:

$$x(t) = x_0 + v_\mathrm{d} t_\mathrm{d} = v_\mathrm{d}(t_0 + t_\mathrm{d}), \qquad\qquad\qquad (\text{A.1})$$

$$y(t) = x(t) \tan \alpha_\mathrm{L}, \qquad\qquad\qquad (\text{A.2})$$

where x and y are the drift distance projections on the x and y-axis, t_d is the drift time and α_L is the Lorentz angle, i.e. the angle with respect to the perpendicular to the wire plane under which electrons drift towards the sense wires. The total drift distance d equals [83]

$$d(t) = \sqrt{x^2(t) + y^2(t)} = \frac{x(t)}{\cos \alpha_\mathrm{L}} = \frac{v_\mathrm{d}(t_0 + t_\mathrm{d})}{\cos \alpha_\mathrm{L}}. \qquad\qquad (\text{A.3})$$

There are three parameters to be fitted: the drift velocity, the global T0 offset and the Lorentz angle. The Lorentz angle is *fixed* to its mean value, so that only the drift velocity and global T0 offset have to be fitted. From A.3 we see that the dependence of the drift distance d on the drift velocity increases with increasing drift time. So it is best to fit the drift velocity at the mesh plane and the global T0 offset at the sense plane, where the drift time is small.

The algorithm to fit both parameters is simple. An offset in the drift velocity or in the global T0 offset leads to a kink in the track segment at the mesh or sense plane, respectively (Fig. A.1). One can refit the segment with an updated T0 offset or drift
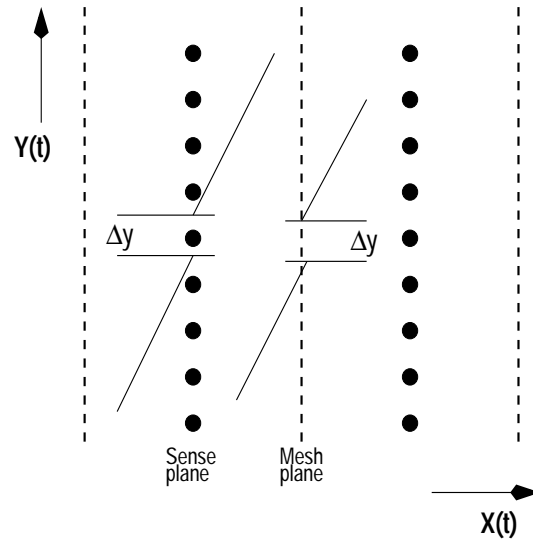
Fig. A.1: Two P-cells showing segments with mis-fitted T0 offset (sense plane) and drift velocity (mesh plane).

velocity, such that the kink is minimized. For this, the pieces of the segment to the left and to the right of the wire plane are fitted separately by a straight line, using the method of absolute deviations. After the hits have been updated for the T0 offset or the drift velocity, the deviation Δy of the intersection points at the wire plane is calculated. According to the magnitude of this deviation, the T0 correction or drift velocity is modified such that after a few iterations both parts of the segment match, within error, at the wire plane. The updated parameter then gives the estimated value for the true T0 offset or drift velocity. More than one iteration is needed, however, since the two parameters are not independent of each other.

Estimating the true value of the parameters is difficult near the minimum of Δy. The deviation Δy is not a smooth function of the fit parameter. In order to obtain the *global* minimum of this function instead of a local minimum, the real function near the mimimum is approximated by a smooth function of second order in the parameter value. This smooth function is used then to obtain its mimimum.

Monte Carlo event weight

The weight to be applied to the events from the Monte Carlo generator used in this work is determined.

A Monte Carlo integral is calculated by sampling the phase space of the generator. If the density of sampling of the phase space depends on any of the phase space variables, themselves, we have to correct the density by applying a weight to the points in phase space so that points in regions with increased density have a smaller contribution to the integral giving the acceptance than those in regions with decreased density. Thus, the weight applied creates an *effective* sampling density that is constant over phase space.

The infinitesimal phase space used in our Monte Carlo generator equals

$$\mathrm{d}^4 \mathcal{P} = \mathrm{d}(\cos\theta)\mathrm{d}\phi\mathrm{d}x\mathrm{d}z, \tag{B.1}$$

where θ is the zenith angle and ϕ the azimuth angle of a track. The variables x and z label a point on the generator surface which, in our case, is a disk. The momenta are sampled from a power law distribution (6.12). The sampling density of points on the generator disk $\mathrm{d}^2 N/\mathrm{d}x\mathrm{d}z$ is constant as is the sampling density in the azimuth angle, $\mathrm{d}N/\mathrm{d}\phi$.

We can think of a phase space where the weight is a constant equal to 1.0. This phase space is given by

$$\mathrm{d}^4 \mathcal{P}_0 = \mathrm{d}(\cos\theta)\mathrm{d}\phi r_\perp \mathrm{d}r_\perp \mathrm{d}\psi, \tag{B.2}$$

where the θ and ϕ are defined as above, $r_\perp$ is the radius from the z-axis perpendicular to the track and $\hat{\psi}$ is perpendicular to the track and to $r_\perp$ (Fig. B.1). From the figure we see that $\mathrm{d}x\mathrm{d}y = r\mathrm{d}r\mathrm{d}\phi$. Noting that $\mathrm{d}r_\perp = \mathrm{d}r\cos\theta$ and $r_\perp\mathrm{d}\psi = r\mathrm{d}\phi$ we find

$$r_\perp \mathrm{d}r_\perp \mathrm{d}\psi = r\mathrm{d}r\mathrm{d}\phi\cos\theta. \tag{B.3}$$
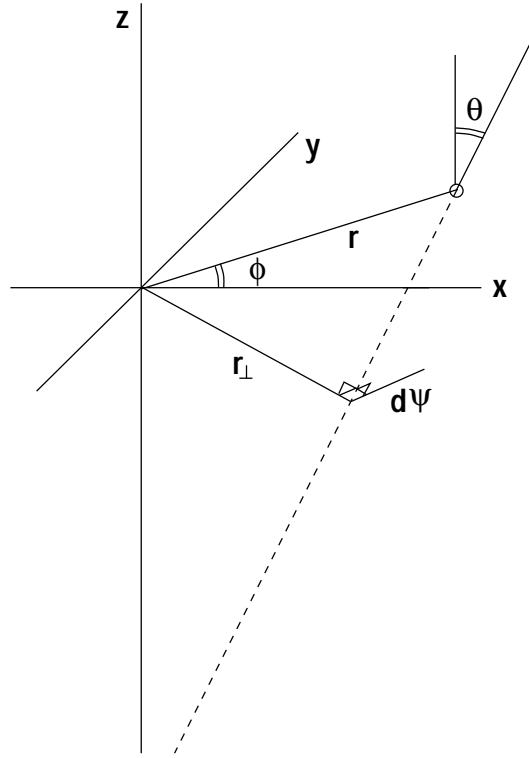
Fig. B.1: Definition of coordinates, see text.

This means that

$$\mathrm{d}^4\mathcal{P}_0 = \mathrm{d}(\cos\theta)\mathrm{d}\phi r_\perp \mathrm{d}r_\perp \mathrm{d}\psi = \mathrm{d}(\cos\theta)\mathrm{d}\phi r \mathrm{d}r \mathrm{d}\phi \cos\theta = \cos\theta \mathrm{d}^4\mathcal{P}. \qquad \text{(B.4)}$$

The acceptance can be formulated as an integral over phase space times a function χ telling us whether a track is inside or outside the sensitive phase space. Rewriting this equation in terms of our new phase space and a weight w we find

$$\mathcal{A} = \int \chi \; \mathrm{d}^4\mathcal{P}_0 = \int \chi \; w \; \mathrm{d}^4\mathcal{P} = \int \chi \; w \; \frac{\mathrm{d}^4\mathcal{P}_0}{\cos\theta}. \qquad \text{(B.5)}$$

Hence the weight $w = \cos\theta$. This weight is properly normalized.

Analytical acceptance

The acceptance for a spherical detector is calculated analytically, using the same generator setup as used for the Monte Carlo acceptance calculation.

The geometrical acceptance of a high energy physics detector is the amount of phase space available to trigger on particles. The particle flow resembles a stationary vectorfield $\boldsymbol{F}(\boldsymbol{r}, \boldsymbol{\theta}, \boldsymbol{\phi})$. It is important for the discussion below to understand that the geometrical acceptance is merely a measure of *the net flow through a predefined region per unit source strength*, the region being defined by the detector geometry and the flow defined by

$$\text{flow} = \int_S \boldsymbol{F} \cdot \hat{n} \ \mathrm{d}S, \tag{C.1}$$

where $\hat{n}$ is the unit vector locally perpendicular to the surface S (pointing outwards) and $\mathrm{d}S$ is an infinitesimal surface element. Note that the definition of "flow" is borrowed from the mathematical theory of vectorfields.

We want to calculate the net flow for the setup as shown in Fig. 6.5. The disk has a fixed radius D and is located at a height h above the spherical detection volume with radius R. Tracks are generated at the disk in a cone of fixed opening angle oriented such that the axis of the cone always passes through the center of the sphere. The opening angle is chosen such that, if the axis of the cone is vertical, the rays at largest angle with respect to the axis just have grazing incidence on the sphere.

The calculated net flow through the spherical surface, defined by the condition that tracks pass this surface from above, depends on the distributions of tracks on the disk and in the solid angle of the cone. The distribution of tracks on the surface of the disk is uniform and the distribution of tracks inside the cone is uniform in spherical coordinates $\mathrm{d}(\cos \theta_l)\mathrm{d}\phi_l$. The density of tracks on the surface is $\rho = \mathrm{d}N_{\text{disk}}/\mathrm{d}S_{\text{disk}} = \text{constant}$. The

flux of tracks from a source with strength $\mathrm{d}N_{\mathrm{disk}}$ will fall off with distance s according to $\boldsymbol{F} = \mathrm{d}N_{\mathrm{disk}}/s^2\,\hat{\boldsymbol{F}}$, where $\hat{\boldsymbol{F}}$ is the unit vector originating in $\mathrm{d}N_{\mathrm{disk}}$ in the direction of the tracks and where s is the distance from $\mathrm{d}N_{\mathrm{disk}}$ (Fig. C.1).

In App. B we derived that a weight w should be applied to the tracks, depending on the zenith angle of a track: $w = \cos\theta$. This weight depends on the zenith angle of the cone's axis, θ_g, as well as on the zenith and azimuth angle θ_l and ϕ_l of the track with respect to the cone's axis (Fig. C.2). From this figure we find:
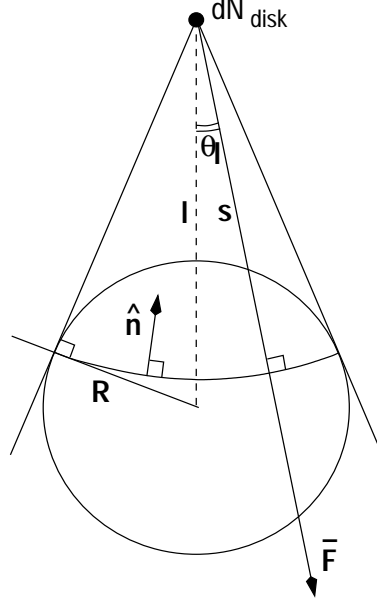
Fig. C.1: Part of Monte Carlo generator setup, see text.

$$\theta = \theta_g + \theta_l \cos\phi_l, \tag{C.2}$$

where $\phi_l = 0$ at maximum θ. From this expression we find

$$w(\theta_g, \theta_l, \phi_l) = \cos\theta = \cos\theta_g \cos(\theta_l \cos\phi_l) - \sin\theta_g \sin(\theta_l \cos\phi_l). \tag{C.3}$$

The distance from $\mathrm{d}N_{\mathrm{disk}}$ to the center of the sphere is l. We will now calculate the flow through the sphere for a fixed value of l, so for an infinitesimal source of strength $\mathrm{d}N_{\mathrm{disk}}$. Since the vectorfield within the sphere has zero divergence, we can modify the surface through which the field passes, without changing the integral. We choose the surface to be the spherical surface $s = $ constant. From Fig. C.1 we see $\hat{F} \cdot \hat{n} = -1$. The expression for the flow now becomes

$$\mathrm{flow} = \int_S \boldsymbol{F} \cdot \hat{n}\, w(\theta)\, \mathrm{d}S = \int \frac{\mathrm{d}N_{\mathrm{disk}}}{s^2}(\hat{F} \cdot \hat{n})s^2 \sin\theta_l \mathrm{d}\theta_l \mathrm{d}\phi_l w(\theta_g, \theta_l, \phi_l). \tag{C.4}$$

Performing the integration over ϕ_l, using that

$$\int_0^{2\pi} \mathrm{d}x \cos(a \cos x) = 2\pi\, \mathcal{J}_0(x), \tag{C.5}$$

$$\int_0^{2\pi} \mathrm{d}x \sin(a \cos x) = 0, \tag{C.6}$$
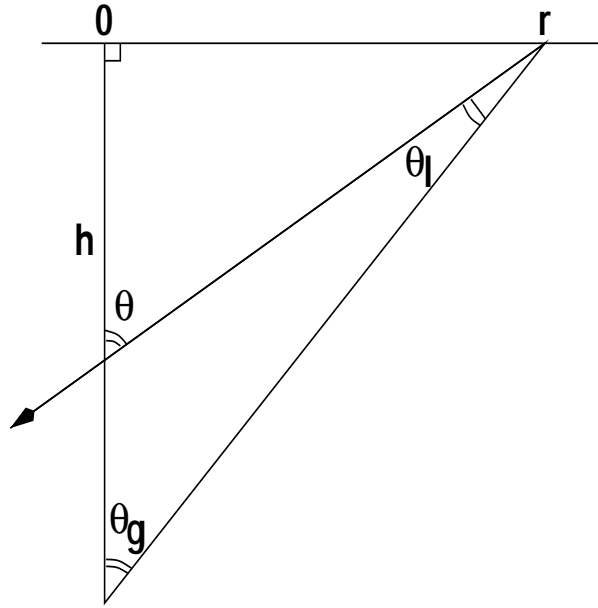
Fig. C.2: Part of Monte Carlo generator setup, see text.

where $\mathcal{J}_0(x)$ is the Bessel function of zeroth order, the expression for the flow becomes

$$\text{flow} = -2\pi \mathrm{d}N_{\mathrm{disk}} \cos\theta_g \int_0^{\arcsin R/l} \sin\theta_l \mathrm{d}\theta_l \mathcal{J}_0(\theta_l). \tag{C.7}$$

The integral can be evaluated resulting in

$$\text{flow} = -\pi \mathrm{d}N_{\mathrm{disk}} \cos\theta_g \arcsin^2(R/l) \, _2F_3\left(\frac{3}{4}, \frac{5}{4}; \frac{3}{2}, \frac{3}{2}, 2; -\arcsin^2(R/l)\right), \tag{C.8}$$

where $_2F_3(\boldsymbol{a}; \boldsymbol{b}; z)$ is the generalized hypergeometric function. The acceptance $\mathcal{A}$ is now found by integrating the flow per unit source strength over all sources $\mathrm{d}N_{\mathrm{disk}} = \rho \mathrm{d}S_{\mathrm{disk}}$,

$$\mathcal{A} = \int \frac{\text{flow}}{\rho}. \tag{C.9}$$

Using that $\cos\theta_g = h/l$, $r\,\mathrm{d}r = l\,\mathrm{d}l$ and neglecting the minus sign for the acceptance, we find

$$\mathcal{A} = \pi \int_h^{\sqrt{h^2+D^2}} l\,\mathrm{d}l \left(\frac{h}{l}\right) \arcsin^2(R/l) \, _2F_3\left(\frac{3}{4}, \frac{5}{4}; \frac{3}{2}, \frac{3}{2}, 2; -\arcsin^2(R/l)\right) \int_0^{2\pi} \mathrm{d}\phi_g. \tag{C.10}$$

This can be rewritten as

$$\mathcal{A} = 2\pi^2 h \int_h^{\sqrt{h^2+D^2}} \mathrm{d}l \arcsin^2(R/l) \, _2F_3\left(\frac{3}{4}, \frac{5}{4}; \frac{3}{2}, \frac{3}{2}, 2; -\arcsin^2(R/l)\right). \tag{C.11}$$

This integral can not be solved analytically. We *can* solve the integral if we approximate the Bessel function in Eq. (C.7) by a cosine function

$$\mathcal{J}_0(\theta_l) \approx \cos\theta_l, \qquad 0 \le \theta_l \le \pi/2. \tag{C.12}$$

The result on the acceptance than becomes

$$\mathcal{A} \approx 2\pi^2 R^2 \left(1 - \frac{1}{\sqrt{1 + (D/h)^2}}\right). \tag{C.13}$$

In the limit $D \to \infty$ we find

$$\lim_{D\to\infty} \mathcal{A} = 2\pi^2 R^2 \tag{C.14}$$

as expected.

The result from the analytical calculation, Eq. (C.13), has been compared with the result from a real Monte Carlo generator with the same setup. For a wide range of relative dimensions of radii R, D and height h, the results agree with each other within the estimated Monte Carlo statistical error.

Tables for spectrum and charge ratio

The results on the differential muon spectra and on the muon charge ratio are tabulated.

Zenith bin 1					
p (GeV/c)	N_{raw}	N_{deco}	$\langle p \rangle$ (GeV/c)	D_μ $(\mathrm{cm}^{-2}\mathrm{s}^{-1}\mathrm{sr}^{-1}(\mathrm{GeV}/c)^{-1})$	$\langle p \rangle^3 \mathrm{D}_\mu$ $(\mathrm{cm}^{-2}\mathrm{s}^{-1}\mathrm{sr}^{-1}(\mathrm{GeV}/c)^2)$
20.0-29.58	28987	28991	23.8±0.5	0.15E-04±0.37E-06±0.19E-05	0.209±0.49E-02±0.29E-01
29.58-43.73	19080	19075	35.8±0.8	0.70E-05±0.25E-06±0.76E-06	0.318±0.12E-01±0.41E-01
43.73-64.67	11409	11532	52.4±1.2	0.22E-05±0.70E-07±0.23E-06	0.318±0.10E-01±0.40E-01
64.67-95.64	5701	6065	77.4±1.7	0.74E-06±0.24E-07±0.79E-07	0.339±0.11E-01±0.43E-01
95.64-141.42	2687	2647	114±2.5	0.21E-06±0.94E-08±0.25E-07	0.299±0.14E-01±0.42E-01
141.42-209.13	1223	1110	170±3.7	0.65E-07±0.38E-08±0.98E-08	0.317±0.19E-01±0.53E-01
209.13-309.25	602	463	252±5.4	0.18E-07±0.14E-09±0.32E-08	0.283±0.23E-01±0.54E-01
309.25-457.30	280	209	366±4.1	0.47E-08±0.53E-09±0.10E-08	0.229±0.26E-01±0.52E-01
457.30-676.24	156	90	586±5.1	0.15E-09±0.16E-09±0.33E-09	0.302±0.27E-01±0.57E-01
676.24-1000.0	88	28	819±12.6	0.24E-09±0.30E-10±0.77E-10	0.128±0.17E-01±0.43E-01

Tab. D.1. Differential cosmic-ray muon spectra for zenith bin 1. N_{raw} and N_{deco} are the number of raw and deconvoluted entries. First errors are statistical, second errors are systematic.

Zenith bin 2					
p (GeV/c)	N_{raw}	N_{deco}	$\langle p \rangle$ (GeV/c)	D_μ (cm^{-2}s^{-1}sr^{-1}(GeV/c)$^{-1}$)	$\langle p \rangle^3 \mathrm{D}_\mu$ (cm^{-2}s^{-1}sr^{-1}(GeV/c)^2)
20.0-29.58	29153	28848	25.0±0.5	0.14E-04±0.43E-06±0.17E-05	0.212±0.58E-02±0.26E-01
29.58-43.73	23924	24466	35.6±0.8	0.69E-05±0.21E-06±0.75E-06	0.308±0.95E-02±0.40E-01
43.73-64.67	12467	12433	52.3±1.2	0.22E-05±0.59E-07±0.23E-06	0.308±0.85E-02±0.39E-01
64.67-95.64	6047	6388	77.1±1.7	0.77E-06±0.22E-07±0.82E-07	0.348±0.10E-01±0.45E-01
95.64-141.42	2853	2791	114±2.5	0.23E-06±0.76E-08±0.28E-07	0.340±0.11E-01±0.48E-01
141.42-209.13	1213	1048	168±3.7	0.60E-07±0.36E-08±0.90E-08	0.284±0.18E-01±0.48E-01
209.13-309.25	542	382	250±5.3	0.14E-07±0.12E-08±0.25E-08	0.218±0.19E-01±0.43E-01
309.25-457.30	234	196	364±6.6	0.54E-08±0.57E-09±0.12E-08	0.258±0.28E-01±0.60E-01
457.30-676.24	152	85	510±5.8	0.57E-10±0.23E-10±0.12E-10	0.007±0.37E-02±0.21E-02
676.24-1000.0	83	25	750±4.7	0.35E-11±0.17E-11±0.11E-11	0.001±0.93E-03±0.63E-03

Tab. D.2. Differential cosmic-ray muon spectra for zenith bin 2. N_{raw} and N_{deco} are the number of raw and deconvoluted entries. First errors are statistical, second errors are systematic.

Zenith bin 3					
p (GeV/c)	N_{raw}	N_{deco}	$\langle p \rangle$ (GeV/c)	D_μ (cm^{-2}s^{-1}sr^{-1}(GeV/c)$^{-1}$)	$\langle p \rangle^3 \mathrm{D}_\mu$ (cm^{-2}s^{-1}sr^{-1}(GeV/c)^2)
20.0-29.58	21102	21652	26.5±0.3	0.14E-04±0.51E-06±0.17E-05	0.249±0.69E-02±0.25E-01
29.58-43.73	23079	22711	35.6±0.8	0.57E-05±0.35E-06±0.61E-06	0.252±0.16E-01±0.33E-01
43.73-64.67	12080	12140	52.4±1.2	0.21E-05±0.70E-07±0.22E-06	0.304±0.10E-01±0.38E-01
64.67-95.64	5952	6189	77.3±1.7	0.73E-06±0.24E-07±0.78E-07	0.332±0.11E-01±0.42E-01
95.64-141.42	2597	2592	114±2.5	0.22E-06±0.64E-08±0.27E-07	0.327±0.95E-02±0.46E-01
141.42-209.13	1291	1133	168±3.6	0.65E-07±0.31E-08±0.98E-08	0.303±0.15E-01±0.52E-01
209.13-309.25	543	401	250±5.0	0.80E-08±0.14E-08±0.14E-08	0.123±0.22E-01±0.24E-01
309.25-457.30	242	154	355±6.6	0.30E-08±0.35E-09±0.65E-09	0.133±0.17E-01±0.33E-01
457.30-676.24	117	77	540±8.0	0.54E-10±0.20E-10±0.12E-10	0.008±0.33E-02±0.20E-02
676.24-1000.0	77	24	836±6.5	0.69E-11±0.32E-11±0.22E-11	0.004±0.18E-02±0.13E-02

Tab. D.3. Differential cosmic-ray muon spectra for zenith bin 3. N_{raw} and N_{deco} are the number of raw and deconvoluted entries. First errors are statistical, second errors are systematic.

Zenith bin 4					
p (GeV/c)	N_{raw}	N_{deco}	$\langle p \rangle$ (GeV/c)	D_μ (cm^{-2}s^{-1}sr^{-1}(GeV/c)$^{-1}$)	$\langle p \rangle^3 \mathrm{D}_\mu$ (cm^{-2}s^{-1}sr^{-1}(GeV/c)^2)
20.0-29.58	5507	4993	28.9±0.1	0.56E-05±0.10E-05±0.68E-06	0.132±0.14E-01±0.10E-01
29.58-43.73	18924	19487	35.7±0.8	0.64E-05±0.27E-06±0.69E-06	0.289±0.12E-01±0.37E-01
43.73-64.67	10681	10867	52.4±1.2	0.21E-05±0.94E-07±0.21E-06	0.292±0.14E-01±0.36E-01
64.67-95.64	5176	5402	77.2±1.7	0.69E-06±0.29E-07±0.74E-07	0.315±0.13E-01±0.40E-01
95.64-141.42	2442	2388	114±2.5	0.21E-06±0.10E-07±0.26E-07	0.308±0.15E-01±0.43E-01
141.42-209.13	1068	931	168±3.2	0.57E-07±0.30E-08±0.86E-08	0.268±0.15E-01±0.46E-01
209.13-309.25	500	418	247±5.0	0.18E-07±0.99E-09±0.33E-08	0.273±0.16E-01±0.56E-01
309.25-457.30	251	147	332±7.3	0.22E-08±0.38E-09±0.48E-09	0.081±0.19E-01±0.25E-01
457.30-676.24	107	56	568±3.6	0.19E-10±0.78E-11±0.42E-11	0.003±0.13E-02±0.72E-03
676.24-1000.0	56	18	712±4.4	0.62E-11±0.19E-11±0.20E-11	0.002±0.11E-02±0.11E-02

Tab. D.4. Differential cosmic-ray muon spectra for zenith bin 4. N_{raw} and N_{deco} are the number of raw and deconvoluted entries. First errors are statistical, second errors are systematic.

Zenith bin 1						
p (GeV/c)	N_{raw}^+	N_{raw}^-	N_{deco}^+	N_{deco}^-	$\langle p \rangle$ (GeV/c)	R_μ
20.0-29.58	16482	12505	16498	12492	23.8±0.5	1.32±0.16E-01±0.59E-02
29.58-43.73	10530	8550	10512	8562	35.8±0.8	1.23±0.20E-01±0.90E-02
43.73-64.67	6239	5170	6304	5228	52.4±1.2	1.21±0.23E-01±0.14E-01
64.67-95.64	3118	2583	3312	2752	77.4±1.7	1.20±0.31E-01±0.22E-01
95.64-141.42	1454	1233	1442	1204	114±2.5	1.20±0.47E-01±0.35E-01
141.42-209.13	685	538	618	492	170±3.7	1.26±0.76E-01±0.60E-01
209.13-309.25	337	265	277	186	252±5.4	1.49±0.42±0.11
309.25-457.30	171	109	124	84	366±4.1	1.48±0.60±0.18
457.30-676.24	91	65	48	42	586±5.1	1.15±0.33±0.22
676.24-1000.0	46	42	14	13	819±12.6	1.14±0.43±0.36

Tab. D.5. Charge ratio for zenith bin 1. N_{raw} and N_{deco} are the number of raw and deconvoluted entries. First errors are statistical, second errors are systematic.

Zenith bin 2						
p (GeV/c)	N_{raw}^+	N_{raw}^-	N_{deco}^+	N_{deco}^-	$\langle p \rangle$ (GeV/c)	R_μ
20.0-29.58	16602	12551	16420	12427	25.0±0.5	1.32±0.16E-01±0.59E-02
29.58-43.73	13425	10499	13736	10730	35.6±0.8	1.28±0.16E-01±0.94E-02
43.73-64.67	7117	5350	7104	5329	52.3±1.2	1.33±0.24E-01±0.15E-01
64.67-95.64	3418	2629	3611	2777	77.1±1.7	1.30±0.33E-01±0.24E-01
95.64-141.42	1637	1216	1605	1186	114±2.5	1.35±0.52E-01±0.40E-01
141.42-209.13	692	521	589	458	168±3.7	1.29±0.80E-01±0.61E-01
209.13-309.25	302	240	213	169	250±5.3	1.26±0.23±0.96E-01
309.25-457.30	133	101	118	77	364±6.6	1.55±0.54±0.18
457.30-676.24	92	60	53	32	510±5.8	1.71±0.68±0.33
676.24-1000.0	52	31	16	9	750±4.7	1.69±0.69±0.53

Tab. D.6. Charge ratio for zenith bin 2. N_{raw} and N_{deco} are the number of raw and deconvoluted entries. First errors are statistical, second errors are systematic.

Zenith bin 3						
p (GeV/c)	N_{raw}^+	N_{raw}^-	N_{deco}^+	N_{deco}^-	$\langle p \rangle$ (GeV/c)	R_μ
20.0-29.58	12159	8943	12467	9185	26.5±0.3	1.36±0.19E-01±0.61E-02
29.58-43.73	13053	10026	12848	9863	35.6±0.8	1.30±0.17E-01±0.95E-02
43.73-64.67	6855	5225	6891	5249	52.4±1.2	1.31±0.24E-01±0.15E-01
64.67-95.64	3398	2554	3534	2655	77.3±1.7	1.33±0.34E-01±0.25E-01
95.64-141.42	1432	1165	1413	1179	114±2.5	1.20±0.47E-01±0.35E-01
141.42-209.13	720	571	653	479	168±3.6	1.36±0.82E-01±0.65E-01
209.13-309.25	324	219	235	166	250±5.0	1.41±0.47±0.11
309.25-457.30	137	105	88	65	355±6.6	1.36±0.54±0.16
457.30-676.24	68	49	44	33	540±8.0	1.32±0.66±0.26
676.24-1000.0	44	33	13	10	836±6.5	1.39±0.57±0.44

Tab. D.7. Charge ratio for zenith bin 3. N_{raw} and N_{deco} are the number of raw and deconvoluted entries. First errors are statistical, second errors are systematic.

Zenith bin 4						
p (GeV/c)	N_{raw}^+	N_{raw}^-	N_{deco}^+	N_{deco}^-	$\langle p \rangle$ (GeV/c)	R_μ
20.0-29.58	2925	2582	2617	2376	28.9±0.1	1.10±0.49E-01±0.49E-02
29.58-43.73	10732	8192	11073	8413	35.7±0.8	1.32±0.19E-01±0.96E-02
43.73-64.67	5952	4729	6048	4819	52.4±1.2	1.26±0.24E-01±0.15E-01
64.67-95.64	2907	2269	3035	2366	77.2±1.7	1.28±0.35E-01±0.24E-01
95.64-141.42	1361	1081	1331	1057	114±2.5	1.26±0.52E-01±0.37E-01
141.42-209.13	609	459	544	387	168±3.2	1.41±0.94E-01±0.67E-01
209.13-309.25	286	214	218	200	247±5.0	1.09±0.20±0.83E-01
309.25-457.30	127	124	77	69	332±7.3	1.12±0.31±0.13
457.30-676.24	58	49	31	25	568±3.6	1.26±0.89±0.24
676.24-1000.0	31	25	9	8	712±4.4	1.21±0.57±0.38

Tab. D.8. Charge ratio for zenith bin 4. N_{raw} and N_{deco} are the number of raw and deconvoluted entries. First errors are statistical, second errors are systematic.

References

[1] Achterberg, A., Cosmic Ray Physics, sources of energetic particles in the universe, Lecture notes, University of Utrecht, 1997.

[2] Longair, M.S., *High energy astrophysics*, volume 1, Cambridge university press, 1992, Particles, photons and their detection.

[3] Simpson, J.A., Ann. Rev. Astr. Astrophys. **33**, 323 (1983).

[4] Proc. of IAU Symp. 195, *Particle Acceleration at Astrophysical Shocks*, Highly energetic physical processes and mechanisms for emission from astrophsyical plasmas, Publ. Astron. Soc. Pacific, p. 291, 2000.

[5] Axford, W.I., in *Proc. 17th Int. Cosmic Ray Conf.*, volume 12, page 155, 1981.

[6] Blandford, R. and Eichler, D., Phys. Rep. **154**, 1 (1987).

[7] Letessier-Selvon, A., astro-ph/0006111 (2000), Lecture given at the XXVIII International Meeting on Fundamental Physics, Sanlucar de Barameda, Cadiz Spain, February 2000.

[8] Chen, H. et al., Phys. Rep. **282**, 1 (1997).

[9] Crookes, W., Phil. Trans. Roy. Soc. **175**, 135 (1879).

[10] Wilson, C.T.R., Proc. Cam. Phil. Soc. **11**, 32 (1900).

[11] Wilson, C.T.R., Proc. Roy. Soc. **68A**, 151 (1901).

[12] Wilson, C.T.R., Proc. Roy. Soc. **69A**, 277 (1901).

[13] Geitel, H., Phys. Z. **2**, 116 (1900).

[14] Elster, J., Phys. Z. **2**, 560 (1900).

[15] Hess, V.F., Phys. Z. **13**, 1084 (1912).

[16] Kolhörster, W., Phys. Z. **14**, 1153 (1913).

[17] Kolhörster, W., Deutsch. Phys. Gesell. Verhandl. **16**, 719 (1914).

[18] Clay, J., Proc. Ned. Akad. v. Wet. **30**, 1115 (1927).

[19] Compton, A.H., Phys. Rev. **43**, 387 (1933).

[20] Johnson, T.H., Phys. Rev. **45**, 569 (1934).

[21] Johnson, T.H., Rev. Mod. Phys. **10**, 193 (1938).

[22] Anderson, C.D., Phys. Rev. **43**, 491 (1933).

[23] Schmeiser, K. and Bothe, W., Ann. Phys. **32**, 161 (1938).

[24] Auger, P. et al., C.R. Acad. Sci. **206**, 1721 (1938).

[25] Kolhörster, W. et al., Naturwiss. **26**, 576 (1938).

[26] Bird, D.J. et al., Phys. Rev. Lett. **71**, 3401 (1993).

[27] L3 Collaboration, Technical Proposal, 1983.

[28] Proc. 'Nuclear Astrophysics', *Selected results from ground-based Cosmic Ray and Gamma-Ray experiments*, Hirschegg, Austria, 1998, astro-ph/9805165.

[29] Greisen, K., Phys. Rev. Lett. **16**, 748 (1966).

[30] Zatsepin, G.T. and Kuzmin, V.A., JETP Lett. **4**, 78 (1966).

[31] Schwarzschild, B., Physics Today , 19 (1997).

[32] Honda, M. et al., Phys. Rev. D. **52**, 4985 (1995), also ICRR-Report-336-95-2.

[33] Gaisser, T.K., *Cosmic Rays and Particle Physics*, Cambridge University Press, 1990.

[34] Feynman, R.P., Phys. Rev. Lett. **23**, 1415 (1969).

[35] Yen, E., Phys. Rev. D **10**, 836 (1974).

[36] A.S. Müller, Erste Untersuchungen ausgedehnter Luftschauer im LEP-Tunnel (CosmoAleph), Master's thesis, Johannes Gutenberg Universität Mainz, 1996.

[37] Bugaev, E.V. et al., Phys. Rev. D. **58**, 5401 (1998).

[38] Baber, S.R., Nucl. Phys. B **4**, 539 (1968).

[39] Rastin, B.C., J. Phys. G **10**, 1609 (1984).

[40] Allkofer, O.C. et al., Phys. Lett. B **36B**, 425 (1971).

[41] Bateman, B.J., Phys. Lett. **36B**, 144 (1971).

[42] Green, P.J., Phys. Rev. D **20**, 1598 (1979).

[43] Ayre, C.A. et al., J. Phys. G **5**, 584 (1975).

[44] De Pascale, M.P. et al., J. Geoph. Res. **98**, 3501 (1993).

[45] Kremer, J. et al., Phys. Rev. Lett. **83**, 4241 (1999).

[46] Bruscoli, M. and Pieri, M., Measurement of cosmic muons with the L3 detector, L3 Note 1335, 1993.

[47] Appleton, I.C. et al., Nucl. Phys. B **26**, 365 (1971).

[48] Nandi, B.C. et al., Nucl. Phys. B **40**, 289 (1972).

[49] Baxendale, J.M. et al., J. Phys. G **1**, 781 (1975).

[50] Rastin, B.C., J. Phys. G **10**, 1629 (1984).

[51] Timmermans, C., *Measurement of muon pair production around the Z-resonance using the L3 detector at LEP.*, PhD thesis, University of Nijmegen, 1992.

[52] Caso, C. et al., Europ. Phys. Jour. C **3**, 1 (1999).

[53] Athanassopoulos, C. et al. (LSND Collaboration), Phys. Rev. Lett. **81**, 1774 (1998).

[54] Allison, W.W.M. et al., Phys. Lett. B **391**, 491 (1997).

[55] Becker-Szendy, R. et al., Phys. Rev. D **46**, 3720 (1992).

[56] Casper, D. et al., Phys. Rev. Lett. **66**, 2561 (1991).

[57] Bernardini, P. et al. (MACRO collaboration), hep-ex/9809003 (1998), Vulcano workshop, May 1998, Vulcano, Italy.

[58] Fukuda, Y. et al., Phys. Lett. B. **433**, 9 (1998).

[59] Fukuda, Y. et al., Phys. Lett. B. **436**, 33 (1998).

[60] Apollonio, M. et al. (CHOOZ collaboration), Phys. Lett. B **420**, 397 (1998).

[61] Gaisser, T.K. et al., Phys. Rev. D **38**, 85 (1988).

[62] Barr, G. et al., Phys. Rev. D **39**, 3532 (1989).

[63] Bugaev, E.V. et al., Phys. Lett. B **232**, 391 (1989).

[64] Volkova, L.V., Soviet J. Nucl. Phys. **37**, 784 (1980).

[65] Mitsui, K. et al., Nuovo Cim. C **9**, 995 (1986).

[66] Butkevich, A.V. et al., Soviet J. Nucl. Phys. **50**, 90 (1989).

[67] Lipari, P., Astropart. Phys. **1**, 195 (1993).

[68] L3 Collaboration, Letter of Intent, 1982.

[69] Adeva, B. et al., Nucl. Instr. and Meth. A **289**, 35 (1990).

[70] Uwer, U., Aufbau und Eichung der Szintillationszähler des L3-Experimentes., Master's thesis, RWTH Aachen, 1990.

[71] L3 Collaboration, L3 Forward-Backward Muon Detector, Technical report, 1991.

[72] Richard-Serre, C., Evaluation de la perte d'energie unitaire et du parcours pour des muons de 2 a 600 GeV dans un absorbant quelconque, Technical report, CERN 71-18, Division de la Machine Synchrocyclotron, 1971.

[73] Brun, R. et al., *GEANT, Detector description and simulation tool*, CERN, Geneva, 1994.

[74] Merk, M., *Study of Bhabha scattering at the Zº-resonance using the L3 detector.*, PhD thesis, University of Nijmegen, 1992.

[75] L3 BGO Collaboration, Results on the calibration of the L3 BGO calorimeter with cosmic rays., Technical report, CERN/L3, 1993.

[76] Spiess, B., *Calibration of the L3 hadron calorimeter barrel with cosmic ray muons*, PhD thesis, ETH Zurich, 1991, Diss. ETH Nr. 9414.

[77] Onvlee, J., *The behaviour of the L3 muon chambers in a magnetic field.*, PhD thesis, University of Amsterdam, 1989.

[78] Uwer, U., The L3 scintillation counter system: description and status, L3 note 2003, 1996.

[79] Beer, P. et al., editor, *Vision modeling and information coding*, volume 40-4 of *Vistas in Astronomy*, Pergamon, 1996, Observatoire de Nice, France.

[80] Karimäki, V., Effective circle fitting for particle trajectories, Technical Report HU-SEFT-1990-04, SEFT, University of Helsinki, 1990.

[81] Karimäki, V., Fast code to fit circular arcs, Technical Report HU-SEFT-1991-10, Research institute for High Energy Physics, University of Helsinki, 1991.

[82] Innocente, V. et al., *GEANE, Average tracking and error propagation package*, L3 report No. 572 edition, 1988.

[83] Fabre, M., *The dimuon mass resolution of the L3 experiment at LEP.*, PhD thesis, ETH Zurich, 1992, Diss. ETH Nr. 9696.

[84] Zhang, D., *Muon Pair production in e^+e^- collisions at the Z resonance.*, PhD thesis, University of Amsterdam, 1994.

[85] Zech, G., Comparing statistical data to Monte Carlo simulation - parameter fitting and unfolding, DESY internal note, DESY 95-113, 1995.

[86] D'Agostini, G., Bayesian reasoning in High Energy Physics, -Principles and Applications-, Lecture at CERN, Geneva, 1998.

[87] D'Agostini, G., Nucl. Instr. and Meth. A **362**, 487 (1995).

[88] Hebbeker, T. et al., Simulation programs for the L3+Cosmics Experiment, Technical report, Humboldt-Universität zu Berlin, 1998.

[89] LeCoultre, P., L3, a new tool for cosmic ray muon research, 25th International Cosmic Ray Conference, Durban, 1997.

[90] Timmermans, C., The L3+Cosmics experiment, 26th International Cosmic Ray Conference, Salt Lake City, 1999.

Summary

In 1991, the L3 detector at CERN, Geneva, measured muons generated by primary cosmic rays colliding with atmospheric nuclei. While the purpose of the measurement was merely to calibrate an L3 subdetector, the data are used in this thesis to investigate whether one can obtain the muon momentum spectrum and the muon charge ratio, as a function of momentum and zenith angle, with good precision.

An accurate measurement of the muon flux as a function of momentum and zenith angle may give vital information on the cosmic-ray neutrino flux. The neutrino flux is related to the muon flux through the common parent particles. Once the muon flux is measured, a cosmic-ray Monte Carlo model can be tuned such that it describes the measured muon flux accurately. The neutrino flux is then automatically determined to a more precise value.

The main topic of this underlying thesis is the design of the reconstruction and simulation software. The existing L3 simulation and reconstruction software was rewritten and extended in order to reconstruct cosmic muons and to simulate the geometry of the L3 hall and shafts. A preliminary version of this software is used to analyze the 1991 cosmic-ray muon data.

The number of events analyzed in this thesis amounts to about 1.4 million, out of a total of about 4.8 million events recorded. The momentum spectrum and the charge ratio are calculated for four different zenith angle bins. The result on the vertical spectrum is compatible with the spectrum as predicted by theory. The statistics are not high enough to conclude anything on the behaviour of the spectrum versus zenith angle.

The charge ratio is compatible with theory and with the results of other experiments. It does not show a strong dependence on the zenith angle. The charge ratio averaged over the momentum range from 20-1000 GeV/c, is consistent with a value of 1.25-1.30.

In order to obtain more accurate measurements on the muon spectrum and the muon charge ratio, a dedicated experiment is needed that can obtain higher statistics and more accurate error estimates. The feasibility of the L3+Cosmics experiment has been shown. It can reach its goal; an accurate measurement of the cosmic-ray muon momentum spectrum upto TeV momenta.

Samenvatting

Muonen van Kosmische Straling
in de L3 Detector

(Een eerste onderzoek ter bepaling van de secundaire muon flux)

In 1991 werd de L3 detector te CERN, Geneve, gebruikt om de secundaire muonen van kosmische straling in onze atmosfeer te meten. Deze muonen zijn afkomstig uit botsingen van primaire kosmische straling (deeltjes uit de kosmos met hoge energieën) met atmosferische atoomkernen. Hoewel het doel van deze meting was om een L3 subdetector te kalibreren, worden de data in dit proefschrift gebruikt om te onderzoeken of het muon impulsspectrum en de muon ladingsverhouding als functie van impuls en zenithoek bepaald kan worden.

Een nauwkeurige meting van de muonflux als functie van impuls en zenithoek kan cruciale informatie geven omtrent de neutrinoflux afkomstig van kosmische straling. De neutrinoflux is gerelateerd aan de muonflux door hun gemeenschappelijke moederdeeltjes. Als de muonflux gemeten is kan een Monte Carlo model voor kosmische straling zodanig worden afgesteld dat het de gemeten muonflux nauwkeurig beschrijft. De neutrinoflux is dan automatisch bepaald tot een meer precieze waarde.

Het belangrijkste onderwerp van het voorliggende proefschrift bestaat uit het ontwerpen van de reconstructie- en simulatiesoftware. De bestaande L3 simulatie- en reconstructie-software zijn herschreven en uitgebreid zodat de banen van de kosmische muonen in de detector gereconstrueerd kunnen worden en de geometrie van de L3 hal en de schachten beschreven zijn. Een voorlopige versie van deze software wordt gebruikt om de kosmische muon data van 1991 te analyseren.

Het aantal gebeurtenissen ('events') geanalyzeerd in deze thesis bedraagt circa 1.4 miljoen. In totaal zijn circa 4.8 miljoen events op tape geschreven. Het impulsspectrum en de ladingsverhouding zijn berekend voor vier verschillende zenithoek bins. Het resultaat aangaande het vertikale spectrum is in overeenstemming met het door de theorie voorspelde spectrum. De statistiek is niet groot genoeg om iets te kunnen concluderen omtrent het gedrag van het spectrum als functie van de zenithoek.

De ladingsverhouding komt overeen met de theorie en met de resultaten van andere experimenten. Het laat geen sterke afhankelijkheid zien als functie van de zenithoek. De ladingsverhouding, uitgemiddeld over een momentum bereik van 20-1000 GeV/c, is consistent met een waarde van 1.25-1.30.

Teneinde nauwkeuriger metingen te verkrijgen van het muonspectrum en de muon ladingsverhouding, is een nieuw experiment nodig dat een hogere statistiek kan verkrijgen en nauwkeuriger foutbepalingen toelaat. Het huidige L3+Cosmics experiment kan dit doel bereiken; een nauwkeurige meting van het kosmische-straling muon impulsspectrum tot TeV/c momenta.

Curriculum Vitae

De auteur van dit proefschrift werd geboren op 1 september 1966 te Rips, gemeente Bakel en Milheeze. Van 1979 tot 1983 volgde hij het middelbaar onderwijs in Stevensbeek alwaar hij het MAVO diploma behaalde. Daarna volgde hij van 1983 tot 1985 het middelbaar technisch onderwijs in de elektrotechniek dat werd afgesloten na het tweede jaar. Van 1985 tot 1987 volgde hij wederom het middelbaar onderwijs in Stevensbeek dat resulteerde in het diploma HAVO. Het daarop volgende jaar behaalde hij de propaedeuse van het hoger technisch onderwijs te Eindhoven in de richting technische natuurkunde. In de periode van 1987 tot 1993 studeerde hij aan de Katholieke Universiteit Nijmegen in de richting natuurkunde, dat werd afgesloten met een stage in de Hoge Energie Astrofysica bij de afdeling Experimentele Hoge Energie Fysica onder leiding van prof. J.M.E. Kuijpers en prof. E.W. Kittel.

In 1994 verrichte de auteur onderzoek aan deze zelfde afdeling in het kader van het voorgestelde "L3+Cosmics" project. Deze werkzaamheden werden verricht als "erkend gewetensbezwaarde militaire dienstplicht", onder leiding van prof. J.M.E. Kuijpers en prof. E.W. Kittel. Van 1995 tot en met 1997 was de auteur aan de afdeling verbonden als Assistent in Opleiding, met als onderzoeksdoel een haalbaarheids studie verrichten aangaande het "L3+Cosmics" project.

Gedurende 1995 en 1996 was de auteur gedetacheerd te CERN, Genève. Van 1997 tot en met medio 2000 werd het onderzoek verder uitgevoerd en voltooid. Gedurende de periode voor en na de detachering heeft de auteur een bijdrage geleverd aan het onderwijs in de vorm van het geven van werkcolleges. Tevens zijn diverse scholen en cursussen bezocht ten behoeve van bijscholing in de Hoge Energie Fysica en Astro Fysica en in presentatie technieken.

Het bovengenoemde onderzoek heeft geleid tot het thans voorliggende proefschrift.